

**TIME-DEPENDENT TENSILE STRENGTH AND
DEFORMABILITY OF ROCK SALT USING FOUR-
POINT BENDING TEST**



**A Thesis Submitted in Partial Fulfillment of the Requirements for the
Degree of Master of Engineering in Geotechnology
Suranaree University of Technology**

Academic Year 2017

กำลังตั้งและการเปลี่ยนรูปร่างเชิงเวลาของเกล็ดหินจากการทดสอบแรงดัดโค้ง
แบบสี่จุด

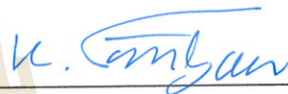


วิทยานิพนธ์นี้เป็นส่วนหนึ่งของการศึกษาตามหลักสูตรปริญญาวิศวกรรมศาสตรมหาบัณฑิต
สาขาวิชาเทคโนโลยีธรณี
มหาวิทยาลัยเทคโนโลยีสุรนารี
ปีการศึกษา 2560

**TIME-DEPENDENT TENSILE STRENGTH AND
DEFORMABILITY OF ROCK SALT USING
FOUR-POINT BENDING TEST**

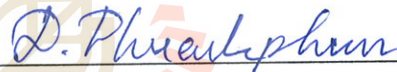
Suranaree University of Technology has approved this thesis submitted in partial fulfillment of the requirements for a Master's Degree.

Thesis Examining Committee



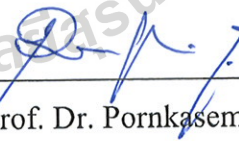
(Prof. Dr. Kittitep Fuenkajorn)

Chairperson



(Asst. Prof. Dr. Decho Phueakphum)

Member (Thesis Advisor)



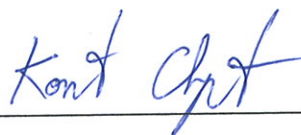
(Assoc. Prof. Dr. Pornkasem Jongpradist)

Member



(Prof. Dr. Santi Maensiri)

Vice Rector for Academic Affairs
and Internationalization



(Assoc. Prof. Flt. Lt. Dr. Kontorn Chamniprasart)

Dean of Institute of Engineering

เจนจิรา ปลั่งกลาง : กำลังดึงและการเปลี่ยนรูปร่างเชิงเวลาของเกลือหินจากการทดสอบ
แรงค้ำโค้งแบบสี่จุด (TIME-DEPENDENT TENSILE STRENGTH AND
DEFORMABILITY OF ROCK SALT USING FOUR-POINT BENDING TEST)
อาจารย์ที่ปรึกษา : ผู้ช่วยศาสตราจารย์ ดร. เดโซ เพ็ชร์กภูมิ, 85 หน้า

การทดสอบแรงดึงแบบกดสี่จุดได้ดำเนินการบนตัวอย่างเกลือหินรูปทรงสี่เหลี่ยมผืนผ้า (50×50×200 ลูกบาศก์มิลลิเมตร) โดยแปรเปลี่ยนวิธีการให้แรงสำหรับชุดทดสอบต่างๆ คือ การทดสอบแรงดึงแบบกดสี่จุดภายใต้การให้แรงกคคกที่เชิงเวลา (การคืบ) การทดสอบแรงดึงแบบกดสี่จุดภายใต้การให้อัตราการกคคกที่เชิงเวลา และทดสอบแรงดึงแบบกดสี่จุดภายใต้การให้แรงแบบวัฏจักร ขึ้นตอนการทดสอบได้ปฏิบัติตามมาตรฐานของ ASTM (D6272-10) โดยค่าความเค้นดึงที่จุดแตกได้จากการคำนวณโดยใช้สูตร และค่าความเครียดดึงได้จากการวัดด้วยสเตรนเกจ การทดสอบภายใต้แรงกคคกที่ได้ใช้แรงที่สัมพันธ์กับค่าความเค้นดึงที่เกิดขึ้นผันแปรจาก 0.5 ถึง 1.25 เมกะปาสกาล โดยค่าความเครียดดึงถูกวัดเป็นเวลา 21 วัน แสดงให้เห็นถึงการเคลื่อนตัวแบบทันทีทันใดและการเคลื่อนตัวแบบเปลี่ยนแปลงเชิงเวลา ซึ่งสามารถอธิบายได้ด้วยสมการการคืบแบบยกกำลัง การทดสอบภายใต้การให้แรงแบบวัฏจักรได้ผันแปรความถี่ของการให้แรงที่ 1 และ 10 มิลลิเฮิร์ตซ์ ซึ่งให้จำนวนรอบการทดสอบสูงถึง 4,800 รอบ ความเค้นดึงสูงสุดมีค่าตั้งแต่ 1.2 ถึง 3.2 เมกะปาสกาล ความเครียดล้ามีค่าลดลงเมื่อจำนวนรอบเพิ่มขึ้นและมีความอ่อนไหวน้อยต่อค่าความถี่ของการให้แรง กราฟแสดงความถี่สามารถอธิบายได้ด้วยสมการลอการิทึม ความยืดหยุ่นของเกลือหินมีค่าลดลงเมื่อจำนวนรอบเพิ่มขึ้น อาจเนื่องมาจากการสะสมตัวของรอยแตกเล็กๆ ที่เกิดขึ้นใหม่ในแต่ละรอบของการให้แรงแบบวัฏจักร ซึ่งมีค่าตั้งแต่ 0.47 ถึง 1.93 จิกะปาสกาล การทดสอบภายใต้อัตราการกคคกที่เชิงเวลาได้ผันแปรอัตราการกคคกจาก 10^{-7} ถึง 10^{-3} เมกะปาสกาลต่อวินาที จนกระทั่งหินเกิดการวิบัติ อัตราการกคคกสูงส่งผลให้ความเค้นดึงมีค่าสูง จากผลการทดสอบทั้งสามชุด ระบุว่าภายใต้แรงดึงของเกลือหินจะมีพฤติกรรมเคลื่อนตัวในเชิงเวลา การเปลี่ยนแปลงรูปร่างแบบคืบถูกควบคุมโดยกลไกการปีน (การเคลื่อนตัวระหว่างผลึก) ซึ่งไม่สามารถคืนสู่สภาพเดิมได้ดังแสดงให้เห็นจากการสะสมตัวของความเครียดระหว่างการให้แรงแบบวัฏจักร การจำลองทางคอมพิวเตอร์ได้นำมาใช้หาความเค้นดึงบริเวณหลังคาช่องเหมืองภายใต้การผันแปรความดันต่ำสุดที่ใช้ในการกักเก็บ ความลึก และความกว้างของช่องเหมือง ผลจากการศึกษาสามารถนำมาใช้เพื่อแสดงให้เห็นถึงความสามารถในการกักเก็บอย่างมีประสิทธิภาพในระยะยาว

สาขาวิชา เทคโนโลยีธรณี
ปีการศึกษา 2560

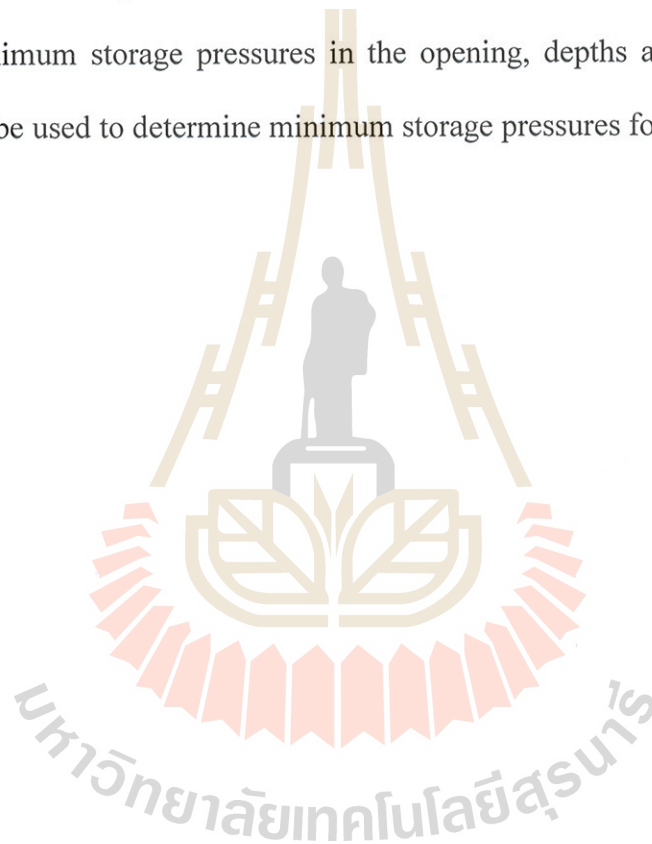
ลายมือชื่อนักศึกษา เจนจิรา ปลั่งกลาง
ลายมือชื่ออาจารย์ที่ปรึกษา D.Thueoolyphm

JENJIRA PLANGKLANG : TIME-DEPENDENT TENSILE STRENGTH
AND DEFORMABILITY OF ROCK SALT USING FOUR-POINT
BENDING TEST. THESIS ADVISOR : ASST. PROF. DECHO
PHUEKPHUM, Ph.D., 85 PP.

CREEP/ BENDING TEST/ CYCLIC LOADING/ LOADING RATE/ FATIGUE

Four-point bending tests have been performed on prismatic ($50 \times 50 \times 200 \text{ mm}^3$) specimens of rock salt. Three loading configurations are used on separate sets of the specimens: static (creep) loading, constant loading rate and cyclic loading. The test procedure is in accordance with the ASTM (D6272-10) standard practice, where applicable. The tensile stresses at the crack initiation point are calculated, and the tensile strains are measured with strain gage. The static loading test uses four loading magnitudes equivalent to the induced tensile stresses from 0.5 to 1.25 MPa. The tensile strains measured up to 21 days show the instantaneous and transient deformations which can be described by the potential creep law. Two loading frequencies are used for the cyclic loading test series: 1 and 10 mHz for up to 4800 cycles. The maximum stresses are varied from 1.2 to 3.2 MPa. The fatigue strength decreases with increasing loading cycles, and is insensitive to the loading frequencies. The fatigue (S-N) curves can be represented by a logarithm relations. The salt elasticity decreases as the number of loading cycles increases, probably due to the accumulated strain of the micro-cracks induced by each loading cycle. The calculated elastic moduli range from 0.47 GPa to 1.93 GPa. The constant loading rate specimens are subjected to the tensile stresses rates from 10^{-7} to 10^{-3} MPa/s. They are loaded until failure. Higher loading rates induce

higher from 10^{-7} to 10^{-3} MPa/s. They are loaded until failure. Higher loading rates induce higher tensile strength. Results from the three test series suggest that under tension rock salt exhibits time-dependent deformations. The creep deformation is governed by the dislocation climb mechanism (sliding between crystals). It is non-recoverable, as evidenced by the accumulated strains measured during the cyclic loading tests. The computer simulations calculate the tensile stresses in mine roof under different minimum storage pressures in the opening, depths and room widths. The findings can be used to determine minimum storage pressures for long term stability.



School of Geotechnology

Academic Year 2017

Student's Signature มนตรี ธีระภรณ์

Advisor's Signature D. Phueakphum

ACKNOWLEDGMENTS

I wish to acknowledge the funding support from Suranaree University of Technology (SUT).

I would like to express my sincere thanks to Prof. Dr. Kittitep Fuenkajorn for his valuable guidance and efficient supervision. I appreciate his strong support, encouragement, suggestions and comments during the research period. I also would like to express my gratitude to Asst. Prof. Dr. Decho Phueakphum and Dr. Prachya Tepnarong for their constructive advice, valuable suggestions and comments on my research works as thesis committee members. Grateful thanks are given to all staffs of Geomechanics Research Unit, Institute of Engineering who supported my work.

Finally, I would like to thank beloved parents for their love, support and encouragement.

มหาวิทยาลัยเทคโนโลยีสุรนารี

Jenjira Plangklang

TABLE OF CONTENTS

| | Page |
|---|-------------|
| ABSTRACT (THAI) | I |
| ABSTRACT (ENGLISH)..... | II |
| ACKNOWLEDGEMENTS..... | IV |
| TABLE OF CONTENTS..... | V |
| LIST OF TABLES..... | IX |
| LIST OF FIGURES | X |
| SYMBOLS AND ABBREVIATIONS..... | XX |
| CHAPTER | |
| I INTRODUCTION..... | 1 |
| 1.1 Background and rationale | 1 |
| 1.2 Research objectives..... | 1 |
| 1.3 Scope and limitations..... | 2 |
| 1.4 Research methodology..... | 3 |
| 1.4.1 Literature review | 4 |
| 1.4.2 Sample preparation..... | 4 |
| 1.4.3 Laboratory testing..... | 4 |
| 1.4.4 Salt properties calibration and strength criterion..... | 5 |
| 1.4.5 Numerical modeling..... | 5 |

TABLE OF CONTENTS (Continued)

| | Page |
|--|-------------|
| 1.4.6 Discussions and Conclusions..... | 5 |
| 1.4.7 Thesis writing | 5 |
| 1.5 Thesis contents..... | 6 |
| II LITERATURE REVIEW | 7 |
| 2.1 Introduction..... | 7 |
| 2.2 Time-dependency of salt..... | 7 |
| 2.3 Fatigue of salt in tension..... | 10 |
| 2.4 Bending test | 10 |
| 2.4.1 Three-point bending test..... | 10 |
| 2.4.2 Four-point bending test | 12 |
| 2.5 Tensile strength of salt..... | 16 |
| 2.6 Loading rate effects..... | 18 |
| 2.7 Cyclic loading of salt in tension..... | 20 |
| 2.8 Roof stability and design | 22 |
| III SAMPLE PREPARATION | 28 |
| 3.1 Introduction..... | 28 |
| 3.2 Sample preparation | 28 |
| 3.3 Strain gage installation..... | 29 |
| IV LABORATORY TESTING METHODS AND RESULTS | 32 |
| 4.1 Introduction..... | 32 |

TABLE OF CONTENTS (Continued)

| | Page |
|--|-------------|
| 4.2 Test method..... | 32 |
| 4.3 Four point bending with constant loading test..... | 35 |
| 4.4 Four point bending with cyclic loading test results | 39 |
| 4.5 Four point bending with constant loading rates test results..... | 52 |
| V SALT CREEP CALIBRATION AND STRENGTH | |
| CRITERION | 59 |
| 5.1 Introduction..... | 59 |
| 5.2 Potential Law | 59 |
| 5.3 Strength criterion | 62 |
| 5.3.1 Tensile strength as a function of stress rate..... | 62 |
| 5.3.2 Strain energy density criterion | 63 |
| VI NUMERICAL MODELLING | 69 |
| 6.1 Introduction..... | 69 |
| 6.2 Numerical modelling (FLAC program)..... | 69 |
| 6.3 Property parameters used in numerical modelling..... | 70 |
| 6.4 Numerical results | 71 |
| 6.5 Discussions | 71 |
| VII DISCUSSIONS, CONCLUSIONS AND | |
| RECOMMENDATIONS FOR FUTURE STUDIES | 82 |
| 7.1 Discussions | 82 |

TABLE OF CONTENTS (Continued)

| | Page |
|---|-------------|
| 7.2 Conclusions..... | 84 |
| 7.3 Recommendations for future studies | 85 |
| REFERENCES | 86 |
| APPENDIX A RESULTS OF COMPUTER SIMULATION | 93 |
| APPENDIX B TECHNICAL PUBLICATION | 133 |
| BIOGRAPHY | 135 |

LIST OF TABLES

| Table | Page |
|-------|---|
| 3.1 | Nominal dimensions of specimens for difference tests. 30 |
| 3.2 | Salt specimens prepared for static loading tests. 30 |
| 3.3 | Salt specimens prepared for cyclic loading tests 30 |
| 3.4 | Salt specimens prepared for constant loading rate tests..... 31 |
| 4.1 | Stresses and strains at failure for cyclic loading tests..... 40 |
| 4.2 | Stress, strain, deflection and elastic modulus for loading rates test..... 54 |
| 5.1 | Calibration of the potential parameters..... 61 |
| 5.2 | Strain energy of each specimen 67 |
| 6.1 | Material parameters used for numerical modeling 70 |
| 6.2 | Minimum pressures, induce tensile stresses and maximum number of loading cycles..... 80 |
| A.1 | Applied load for creep test..... 130 |
| A.2 | Applied load for cyclic loading test..... 131 |
| A.3 | Applied load for loading rate test..... 132 |

LIST OF FIGURES

| Figure | Page |
|--------|---|
| 1.1 | Research methodology..... 3 |
| 2.1 | Typical deformation as a function of time of creep materials 8 |
| 2.2 | Typical stress-strain curve for rock materials..... 9 |
| 2.3 | Schematic of a suitable apparatus for flexure test by center-point loading method (ASTM (C293-02)) 12 |
| 2.4 | Loading diagram (ASTM (D6272-10)) 13 |
| 2.5 | Elastic beam with (a) fixed ends and (b) simple (pin) supports. 15 |
| 2.6 | Beam tensile test results showing that the UTS is an exponential function of the beam length / height ratio..... 17 |
| 2.7 | Tensile stress-strain curves for various loading rates 20 |
| 2.8 | Load-deformation curves of Brazilian split fatigue tests of constant average load..... 21 |
| 2.9 | Load-deformation curves of Brazilian split fatigue tests of variation average load..... 22 |
| 2.10 | Stability chart for tensile fracturing of roof beds..... 23 |
| 2.11 | Cross section through Bostock No. 5 panel showing model configuration..... 25 |
| 2.12 | Maximum principal stress distribution around central two rooms in the Bostock No. 5 panel (MPa)..... 25 |

LIST OF FIGURES (Continued)

| Figure | Page |
|---------------|--|
| 2.13 | Rock displacement around a cavern with reduced overburden stiffness 26 |
| 3.1 | Example of prismatic salt specimens with nominal dimensions of 50×50×200 mm ³ 29 |
| 3.2 | Some salt specimens prepared for four point bending test with L/D = 4.0. 29 |
| 3.3 | Examples of prismatic salt specimen with strain gage position salt specimens prepared for four point bending test..... 29 |
| 4.1 | Test arrangement for four-point bending test (ASTM (D6272-10))..... 33 |
| 4.2 | Four point bending test equipment. 34 |
| 4.3 | Tensile strain (ϵ_t) as a function of time (t) for constant loading under tensile stresses of 0.5, 0.75, 1.0 and 1.25 MPa..... 36 |
| 4.4 | Compressive strain (ϵ_c) as a function of time (t) for constant loading under compressive stresses of 0.5, 0.75, 1.0 and 1.25 MPa..... 37 |
| 4.5 | Deflection as a function of time (t) for static loading under tensile stresses of 0.5, 0.75, 1.0 and 1.25 MPa 38 |
| 4.6 | Tensile stresses (σ_T) plotted as a function of tensile strain (ϵ_T) for 10 mHz ... 41 |
| 4.7 | Tensile stresses (σ_T) plotted as a function of tensile strain (ϵ_T) for 10 mHz ... 42 |
| 4.8 | Tensile stresses (σ_T) plotted as a function of tensile strain (ϵ_T) for 1 mHz 43 |
| 4.9 | Tensile stresses (σ_T) plotted as a function of tensile strain (ϵ_T) for 1 mHz 44 |
| 4.10 | Accumulated tensile strain (ϵ_t) as a function of time for 10 mHz. 45 |

LIST OF FIGURES (Continued)

| Figure | Page |
|--------|--|
| 4.11 | Accumulated tensile strain (ϵ_t) as a function of time for 1 mHz. 46 |
| 4.12 | Fatigue tensile strengths (S) as a function of number of loading cycles at failure (N)..... 47 |
| 4.13 | Elastic moduli (E) plotted as a function of number of loading cycles (N) up to failure for $f = 10$ mHz. 48 |
| 4.14 | Elastic moduli (E) plotted as a function of number of loading cycles (N) up to failure for $f = 1$ mHz 49 |
| 4.15 | Normalized elastic moduli (E/E_0) plotted as a function of number of loading cycles (N) up to failure for $f = 10$ mHz..... 50 |
| 4.16 | Normalized elastic moduli (E/E_0) plotted as a function of number of loading cycles (N) up to failure for $f = 1$ mHz..... 51 |
| 4.17 | Some post-test specimens of Maha Sarakham salt obtained from four point bending testing under various loading rates..... 53 |
| 4.18 | Some cleavage fracturing and inter granular fracturing of salt specimens..... 53 |
| 4.19 | Tensile stress-strain curves for various loading rates. 55 |
| 4.20 | Compressive stress-strain curves for various loading rates 56 |
| 4.21 | Deflection (δ) as a function of time (t) for loading rates under tensile stresses rates of 4×10^{-7} to 4×10^{-3} MPa..... 57 |

LIST OF FIGURES (Continued)

| Figure | Page |
|--------|--|
| 4.22 | Tensile strain (ϵ_t) as a function of deflection (δ) for loading rates under tensile stresses rates of 4×10^{-7} to 4×10^{-3} MPa 58 |
| 5.1 | Potential parameters as a function of tensile stress..... 62 |
| 5.2 | Tensile strengths (σ_T) as function of stress..... 63 |
| 5.3 | Strain energy of distortion (W_d) as a function of mean strain energy (W_m).... 66 |
| 6.1 | Finite difference mesh developed for FLAC simulation, mining depths are 175, 250 and 300 m and room width is 10 m..... 73 |
| 6.2 | Finite difference mesh developed for FLAC simulation, mining depths are 175, 250 and 300 m and room width is 15 m..... 74 |
| 6.3 | Finite difference mesh developed for FLAC simulation, mining depths are 175, 250 and 300 m and room width is 20 m..... 75 |
| 6.4 | Fatigue tensile stresses as a function of cycle at 175 m with 10 m (a), 15 m (b) and 20 m (c) room widths..... 76 |
| 6.5 | Fatigue tensile stresses as a function of cycle at 250 m with 10 m (a), 15 m (b) and 20 m (c) room widths 77 |
| 6.6 | Fatigue tensile stresses as a function of cycle at 250 m with 10 m (a), 15 m (b) and 20 m (c) room widths. 78 |
| 6.7 | Minimum pressures as a function of cycles various mining depths (300 m (a), 250 m (b) and 175 m (c)) 79 |

LIST OF FIGURES (Continued)

| Figure | Page |
|---|------|
| A.1 Stress distribution (top) and displacement vectors (bottom) in mine roof for depths of 175 m and width of 10 m with minimum pressure at 20 % of in-situ stress..... | 94 |
| A.2 Stress distribution (top) and displacement vectors (bottom) in mine roof for depths of 175 m and width of 10 m with minimum pressure at 30 % of in-situ stress..... | 95 |
| A.3 Stress distribution (top) and displacement vectors (bottom) in mine roof for depths of 175 m and width of 10 m with minimum pressure at 40 % of in-situ stress..... | 96 |
| A.4 Stress distribution (top) and displacement vectors (bottom) in mine roof for depths of 175 m and width of 10 m with minimum pressure at 50 % of in-situ stress..... | 97 |
| A.5 Stress distribution (top) and displacement vectors (bottom) in mine roof for depths of 175 m and width of 15 m with minimum pressure at 20 % of in-situ stress..... | 98 |
| A.6 Stress distribution (top) and displacement vectors (bottom) in mine roof for depths of 175 m and width of 15 m with minimum pressure at 30 % of in-situ stress..... | 99 |

LIST OF FIGURES (Continued)

| Figure | Page |
|--|------|
| A.7 Stress distribution (top) and displacement vectors (bottom) in mine roof for depths of 175 m and width of 15 m with minimum pressure at 40 % of in-situ stress..... | 100 |
| A.8 Stress distribution (top) and displacement vectors (bottom) in mine roof for depths of 175 m and width of 15 m with minimum pressure at 50 % of in-situ stress..... | 101 |
| A.9 Stress distribution (top) and displacement vectors (bottom) in mine roof for depths of 175 m and width of 20 m with minimum pressure at 20 % of in-situ stress..... | 102 |
| A.10 Stress distribution (top) and displacement vectors (bottom) in mine roof for depths of 175 m and width of 20 m with minimum pressure at 30 % of in-situ stress..... | 103 |
| A.11 Stress distribution (top) and displacement vectors (bottom) in mine roof for depths of 175 m and width of 20 m with minimum pressure at 40 % of in-situ stress..... | 104 |
| A.12 Stress distribution (top) and displacement vectors (bottom) in mine roof for depths of 175 m and width of 20 m with minimum pressure at 50 % of in-situ stress..... | 105 |

LIST OF FIGURES (Continued)

| Figure | Page |
|--|-------------|
| A.13 Stress distribution (top) and displacement vectors (bottom) in mine roof for depths of 200 m and width of 10 m with minimum pressure at 20 % of in-situ stress..... | 106 |
| A.14 Stress distribution (top) and displacement vectors (bottom) in mine roof for depths of 200 m and width of 10 m with minimum pressure at 30 % of in-situ stress..... | 107 |
| A.15 Stress distribution (top) and displacement vectors (bottom) in mine roof for depths of 200 m and width of 10 m with minimum pressure at 40 % of in-situ stress..... | 108 |
| A.16 Stress distribution (top) and displacement vectors (bottom) in mine roof for depths of 200 m and width of 10 m with minimum pressure at 50 % of in-situ stress..... | 109 |
| A.17 Stress distribution (top) and displacement vectors (bottom) in mine roof for depths of 200 m and width of 15 m with minimum pressure at 20 % of in-situ stress..... | 110 |
| A.18 Stress distribution (top) and displacement vectors (bottom) in mine roof for depths of 200 m and width of 15 m with minimum pressure at 30 % of in-situ stress..... | 111 |

LIST OF FIGURES (Continued)

| Figure | Page |
|--|-------------|
| A.19 Stress distribution (top) and displacement vectors (bottom) in mine roof for depths of 200 m and width of 15 m with minimum pressure at 40 % of in-situ stress..... | 112 |
| A.20 Stress distribution (top) and displacement vectors (bottom) in mine roof for depths of 200 m and width of 15 m with minimum pressure at 50 % of in-situ stress..... | 113 |
| A.21 Stress distribution (top) and displacement vectors (bottom) in mine roof for depths of 200 m and width of 20 m with minimum pressure at 20 % of in-situ stress..... | 114 |
| A.22 Stress distribution (top) and displacement vectors (bottom) in mine roof for depths of 200 m and width of 20 m with minimum pressure at 30 % of in-situ stress..... | 115 |
| A.23 Stress distribution (top) and displacement vectors (bottom) in mine roof for depths of 200 m and width of 20 m with minimum pressure at 40 % of in-situ stress..... | 116 |
| A.24 Stress distribution (top) and displacement vectors (bottom) in mine roof for depths of 200 m and width of 20 m with minimum pressure at 50 % of in-situ stress..... | 117 |

LIST OF FIGURES (Continued)

| Figure | Page |
|--|------|
| A.25 Stress distribution (top) and displacement vectors (bottom) in mine roof for depths of 200 m and width of 10 m with minimum pressure at 20 % of in-situ stress..... | 118 |
| A.26 Stress distribution (top) and displacement vectors (bottom) in mine roof for depths of 200 m and width of 10 m with minimum pressure at 30 % of in-situ stress..... | 119 |
| A.27 Stress distribution (top) and displacement vectors (bottom) in mine roof for depths of 200 m and width of 10 m with minimum pressure at 40 % of in-situ stress..... | 120 |
| A.28 Stress distribution (top) and displacement vectors (bottom) in mine roof for depths of 200 m and width of 10 m with minimum pressure at 50 % of in-situ stress..... | 121 |
| A.29 Stress distribution (top) and displacement vectors (bottom) in mine roof for depths of 200 m and width of 15 m with minimum pressure at 20 % of in-situ stress..... | 122 |
| A.30 Stress distribution (top) and displacement vectors (bottom) in mine roof for depths of 200 m and width of 15 m with minimum pressure at 30 % of in-situ stress..... | 123 |

LIST OF FIGURES (Continued)

| Figure | Page |
|--|------|
| A.31 Stress distribution (top) and displacement vectors (bottom) in mine roof for depths of 200 m and width of 15 m with minimum pressure at 40 % of in-situ stress..... | 124 |
| A.32 Stress distribution (top) and displacement vectors (bottom) in mine roof for depths of 200 m and width of 15 m with minimum pressure at 50 % of in-situ stress..... | 125 |
| A.33 Stress distribution (top) and displacement vectors (bottom) in mine roof for depths of 200 m and width of 20 m with minimum pressure at 20 % of in-situ stress..... | 126 |
| A.34 Stress distribution (top) and displacement vectors (bottom) in mine roof for depths of 200 m and width of 20 m with minimum pressure at 30 % of in-situ stress..... | 127 |
| A.35 Stress distribution (top) and displacement vectors (bottom) in mine roof for depths of 200 m and width of 20 m with minimum pressure at 40 % of in-situ stress..... | 128 |
| A.36 Stress distribution (top) and displacement vectors (bottom) in mine roof for depths of 200 m and width of 20 m with minimum pressure at 50 % of in-situ stress..... | 129 |

SYMBOLS AND ABBREVIATIONS

| | | |
|---|---|-------------------------|
| δ | = | Deflection |
| η | = | Empirical constant |
| κ | = | Empirical constant |
| β | = | Empirical constant |
| γ | = | Empirical constant |
| f | = | Frequency |
| ε | = | Strain |
| $\varepsilon_1, \varepsilon_2, \varepsilon_3$ | = | Principal strain |
| $\sigma_1, \sigma_2, \sigma_3$ | = | Principal stress |
| ε_c | = | Compressive strain |
| γ_{oct} | = | Octahedral shear strain |
| τ_{oct} | = | Octahedral shear stress |
| σ_R | = | Constant stress rate |
| σ_T | = | Tensile strength |
| σ_t | = | Tensile stress |
| ε_t | = | Tensile strain |
| ρ | = | Density |
| $\partial\sigma/\partial t$ | = | Constant stress rate |
| b | = | Specimen width |

SYMBOLS AND ABBREVIATIONS (Continued)

| | | |
|------------|---|------------------------------------|
| d | = | Specimen thickness |
| E | = | Elastic modulus |
| E_0 | = | Normalized elastic |
| G | = | The shear modulus |
| K | = | The bulk modulus |
| L | = | Support span |
| N | = | Number of cycle |
| P | = | Load |
| P_{\min} | = | Minimum pressure |
| S | = | Fatigue strength |
| t | = | Time |
| W | = | Strain energy density |
| W_d | = | Distortional strain energy density |
| W_m | = | Mean strain energy |

CHAPTER I

INTRODUCTION

1.1 Background and rationale

Tensile strength of rock dictates the maximum span and standup time of the mine opening. The tensile strength can be obtained in the laboratory by various methods, including direct tension tests, Brazilian tension tests, ring tension tests, flexural tests, three- and four-point bending tests (Phueakphum et al., 2013; Wisetsaen et al., 2015). For the analysis and design of the mine roof span the bending test is more preferable than the others because the bending test specimen will subject to the stress configurations similar to those in the mine roof. The design of the mine roof span for brittle rock will normally consider the fracture characteristics (shear strength, spacing, water pressure, etc.). For soft and time-dependent rocks, such as rock salt and potash, the design considerations should also be placed on the time-dependent strength and deformation of the materials.

1.2 Research objectives

The objective of this study is to determine the time-dependent tensile strength and deformability of rock salt. The four-point bending tests are performed on prismatic beams ($50 \times 50 \times 200 \text{ mm}^3$) of rock salt specimens. Three loading configurations are used on separate sets of the specimens: static loading, cyclic loading, and constant loading rate. The static loading test uses four loading magnitudes equivalent to the induced

tensile stresses from 0.5 to 1.25 MPa. Two loading frequencies are used for the cyclic loading test series: 1 and 10 mHz. The applied loading rates are varied which are equivalent to the tensile stress rates of 10^{-7} to 10^{-3} MPa/s. This will be obtained from numerical simulations. The findings can be used to determine salt minimum cavern pressures for long term stability. This will be obtained from numerical simulations.

1.3 Scope and limitations

The scope and limitations of the research include as follows.

1. All specimens are conducted on rock specimens obtained from the Maha Sarakham formation.
2. The nominal dimensions of prismatic blocks are $50 \times 50 \times 200$ mm³.
3. The creep tests are performed with the applied tensile stresses varying from 0.50, 0.75, 1.0 to 1.25 MPa for 21 days.
4. Numerical modeling will be performed to assist in the design of the salt roof thickness.
5. The cyclic loading tests have two frequencies: 1 and 10 mHz.
6. The loading rate tests use stress rates from 10^{-7} to 10^{-3} MPa/s at the crack initiation point.
7. The testing procedure will follow the relevant standard practices (ASTM (D6272-10)).
8. The research findings are published in conference paper and journal.

1.4 Research methodology

The research methodology shown in Figure 1.1 comprises 7 steps; including literature review, sample preparation, laboratory testing, salt properties calibration and strength criterion, numerical modeling, discussions and conclusions and thesis writing.

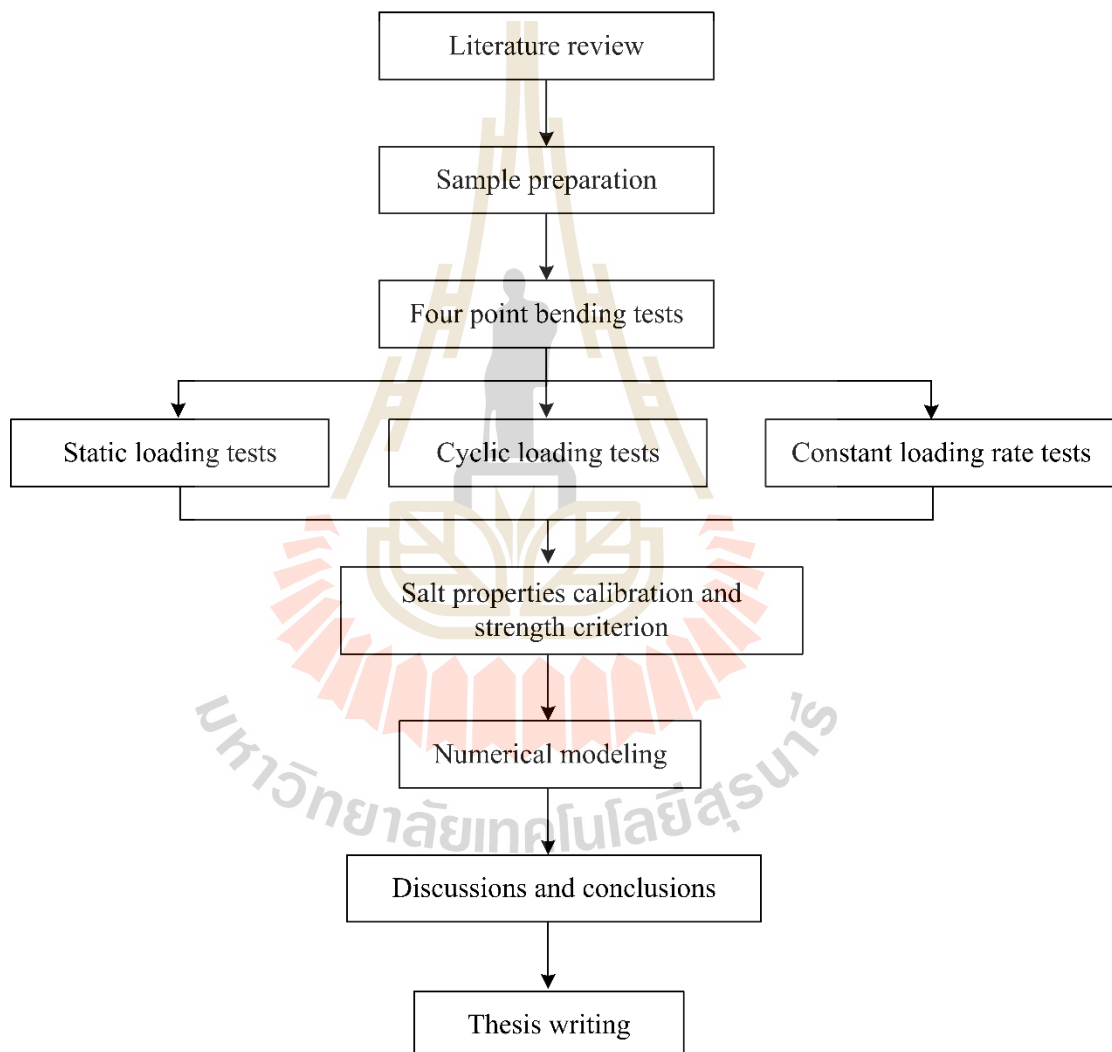


Figure 1.1 Research methodology

1.4.1 Literature review

Literature review are carried out to study the previous researches on time-dependency of salt, fatigue of salt in tension, bending test, tensile strength of salt, loading rate effects, cyclic loading of salt in tension and roof stability and design. The sources of information are from text books, journals, technical reports and conference papers. A summary of the literature review are given in the thesis.

1.4.2 Sample preparation

Rock samples used here have been obtained from underground openings of ASEAN Potash Chaiyaphum Public Company Limited (APOT). They belong to the Lower Salt member of the Maha Sarakham formation. Sample preparation are carried out in the laboratory at Suranaree University of Technology. The specimens are prepared to obtain prismatic blocks with nominal dimensions of $50 \times 50 \times 200 \text{ mm}^3$.

1.4.3 Laboratory testing

Four-point bending tests follow the ASTM standard practice (D6272-10). A data logger (TC-32K) connected with the switching box (Type B-2760) is used to monitor the induced tensile strains while loading. Three loading configurations are used on separate sets of the specimens: static loading, constant loading rate and cyclic loading.

1) In the static loading tests four loading magnitudes of 0.5, 0.75, 1.0 and 12.5 MPa are used. Each specimen is tested up to 21 days.

2) The constant loading rates are applied under four constant rates from 0.0045 N/s to 45 N/s, which are equivalent to the induced tensile stressed rates at the center of the specimen from 10^{-7} to 10^{-3} MPa/s.

3) The cyclic loading tests are used two loading frequencies: 1 and 10 mHz. The stresses and strains are monitored until failure occurs.

1.4.4 Salt properties calibration and strength criterion

The potential creep law is applied here to describe the time-dependent deformation of the creep specimens. Regression analyses on the strain-time curves based using the SPSS statistical software are performed to determine these parameters for each rock salt specimen. The strain energy density principle is applied here to describe the salt strengths and deformability under different loading rates of constant loading rates tests and different amplitudes of cyclic loading tests.

1.4.5 Numerical modeling

A finite difference analysis with the elastic model is performed to simulate mine roof in rock salt to determine the maximum tensile stresses for different storage pressures, roof widths and depths. The analysis is made in plane strain condition. The results can be used to suggest the salt minimum cavern pressures for long term stability.

1.4.6 Discussions and Conclusions

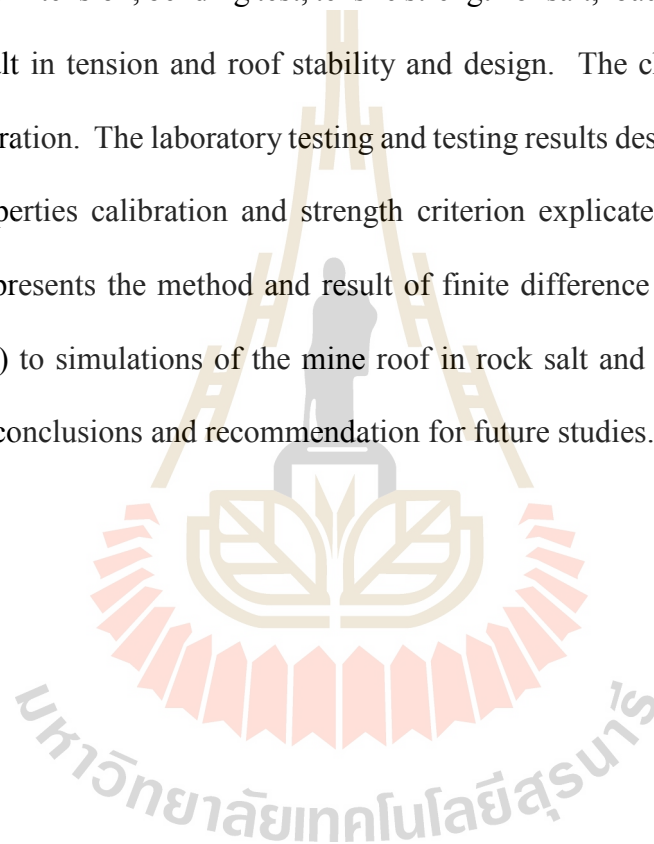
Discussions are made on the reliability and adequacies of the approaches used here. Future research needs are identified. All research activities, methods, and results are documented and complied in the thesis. The research or findings are published in the conference proceedings or journals.

1.4.7 Thesis writing

All research activities, methods, and results are documented and complied in the thesis.

1.5 Thesis contents

This research thesis is divided into eight chapters. The first chapter introduces the thesis by briefly describing the background of problems and significance of the study. The research objectives, methodology, scope and limitations are identified. The second chapter presents results of the literature review about time-dependency of salt, fatigue of salt in tension, bending test, tensile strength of salt, loading rate effects, cyclic loading of salt in tension and roof stability and design. The chapter three describes sample preparation. The laboratory testing and testing results described in chapter four. The salt properties calibration and strength criterion explicated are in chapter five. Chapter six presents the method and result of finite difference analysis using FLAC (Itasca, 1992) to simulations of the mine roof in rock salt and chapter seven present discussions, conclusions and recommendation for future studies.



CHAPTER II

LITERATURE REVIEW

2.1 Introduction

The topic reviewed here include time-dependency of salt, fatigue of salt in tension, bending test, tensile strength of salt, loading rate effect, cyclic loading of salt in tension and roof stability and design.

2.2 Time-dependency of salt

The time-dependent deformation (or creep) is the process at which the rock can continue deformation without changing stress (Fuenkajorn and Daemen, 1988; Dusseault and Fordham, 1993; Jeremic, 1994; Knowles et al., 1998). The creep strain seldom can be recovery fully when loads are removed, thus it is largely plastic deformation. Creep deformation occurs in three different phases, as shown in Figure 2.1, which relatively represents a model of salt properties undergoing creep deformation due to the sustained constant load. Upon application of a constant force on the rock salt, an instantaneous elastic strain (ϵ_e) is induced. The elastic strain is followed by a primary or transient strain, shown as Region I. Region II, characterized by an almost constant slope in the diagram, corresponds to secondary or steady state creep. Tertiary or accelerating creep leading to rather sudden failure is shown in Region III. Laboratory investigations show that removal of applied load in Region I at point L will cause the strain to fall rapidly to the M level and then asymptotically back to zero at N.

The distance LM is equal to the instantaneous strain ϵ_e . No permanent strain is induced here if the removal of stress takes place in the steady-state phase the permanent strain (ϵ_p) will occur. From the stability point of view, salt structure deformations after constant load removal have only academic significance, since the stresses imposed underground due to mining operations are irreversible. The behavior of the salts with time-dependent deformation under constant load is characterized as a visco-elastic and visco-plastic phenomenon. Under these conditions the strain criteria are superior to the strength criteria for design purposes, because failure of most salt pillars occurs during accelerated or tertiary phase of creep, due to the almost constant applied load.

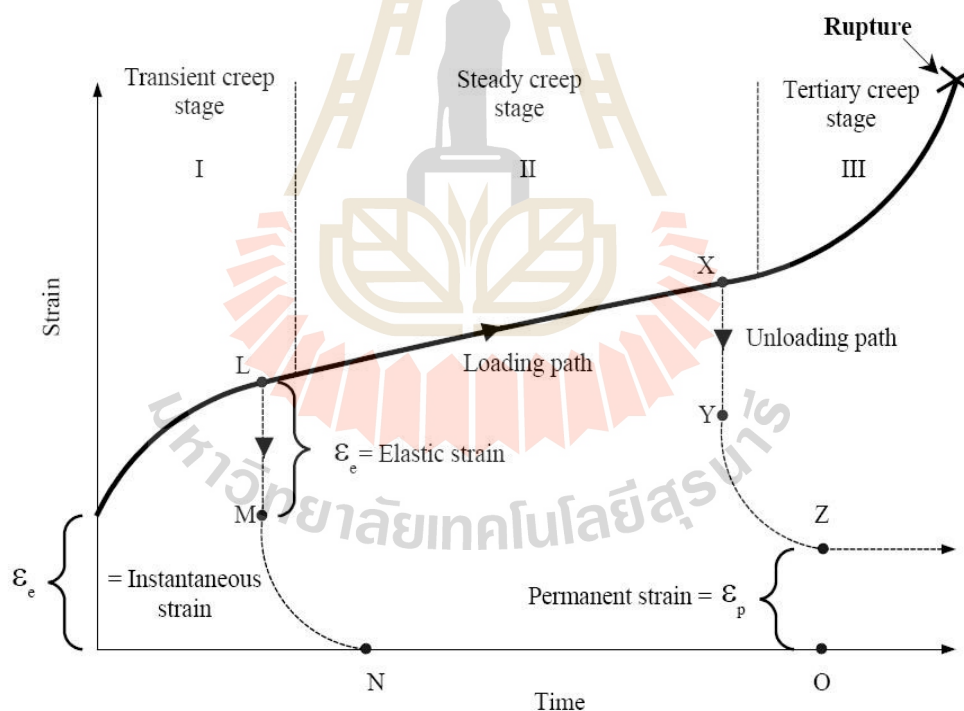


Figure 2.1 Typical deformation as a function of time of creep materials (Jeremic, 1994).

A typical stress versus strain curve for a rock specimen under loading can be divided into four regions as revealed in Figure 2.2. In region I there is a small foot in the curve, and the observed modulus is lower because of the nonelastic strain arising from the closing up of the microcracks and pore. Region II represents the true modulus of the bulk material and the stress versus strain curve here is linear. The stress-strain curve then starts to deviate from linearity in region III indicating the stage of nucleation of microcracks. Here there is a general loosening of the grain boundaries which is not yet obvious in microscopic observations. Only in region IV do microcracks become visible in an optical microscope. The only difference was that regions III and IV of the static stress-strain curve were extended to larger strains. Consequently the fracture strength was increased primarily because of a larger strain-to-fracture (Kumar, 1968; Liang et al., 2010).

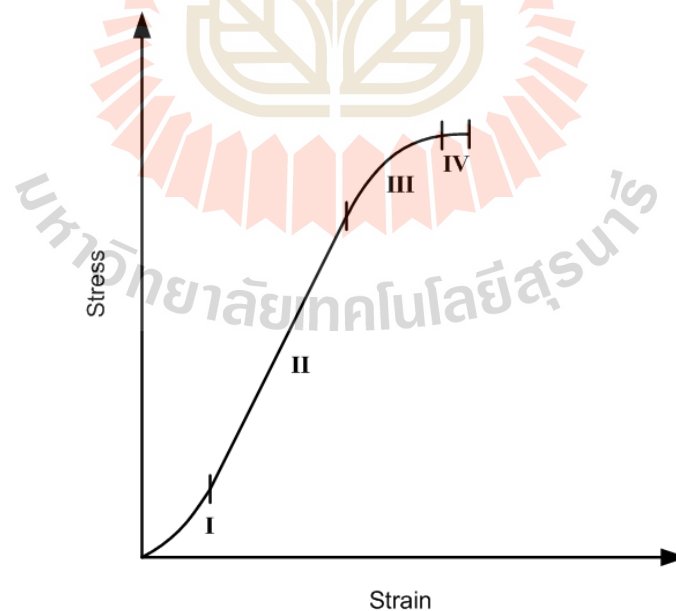


Figure 2.2 Typical stress-strain curve for rock materials (Kumar, 1968; Liang et al., 2010).

2.3 Fatigue of salt in tension

The fatigue properties of rock depend on the maximum compressive and tensile stresses generated during cyclic loading, the load amplitude, and the loading frequency (Thirumalai and Demou, 1974; Xiao et al., 2010).

Voznesenskii et al. (2017) experiments with cyclic fatigue loading samples of rock salt (halite) showed a non-monotonic change in strength, depending on the number of load cycles. The minimum strength is observed at 20 cycles for cyclic loadings up to 40%, and 60% from damage tension at 15 cycles until 80% loading. The two most likely mechanisms are dilation, causing strength decrease; and consolidation, due to the cohesion of halite grains under cyclic deformation, causing a strength increase. Their combination reduces the strength of the initial area of the deformation and its subsequent increase after reaching a minimum. These changes are consistent with changes in the strength storage modulus and volume deformation, depending on the number of loadings. The dependencies between the strength and quality factor will allow the strength of the objects under study to be assessed by non-destructive testing methods while leaving them intact.

2.4 Bending test

2.4.1 Three-point bending test

The American Society for Testing and Materials (ASTM (C293-02)) specifies the methods and sample preparation for the three-point bending test. All forces are applied perpendicular to the face of the specimen continuously without eccentricity. A diagram of an apparatus that accomplishes this purpose is shown in Figure 2.3. The load is applied at a constant rate to the breaking point. The maximum

stress on the tension face increases under loading rate between 0.9 and 1.2 MPa/min (125 and 175 psi/min). The loading rate is calculated using the following equation:

$$r = 2Sbd^2 / 3L \quad (2.1)$$

where r is loading rate, N/min (lb/min), S is rate of increase in the maximum stress on the tension face, MPa/min (psi/min), b is average width of the specimen as oriented for testing, mm (in.), d is average depth of the specimen as oriented for testing, mm (in.) and L is span length, mm (in.).

The modulus of rupture is calculated as follows:

$$R = 3PL / 2bd^2 \quad (2.2)$$

where R is modulus of rupture, MPa (psi), P is maximum applied load indicated by the testing machine, N (lbf), L is span length, mm (in.), b is average width of specimen at the fracture, mm (in.) and d is average depth of specimen at the fracture, mm (in.). A bar of rectangular cross section rests on two supports and is loaded at two points or two loading noses. The distance between the loading noses (the load span) is either one third or one half of the support span.

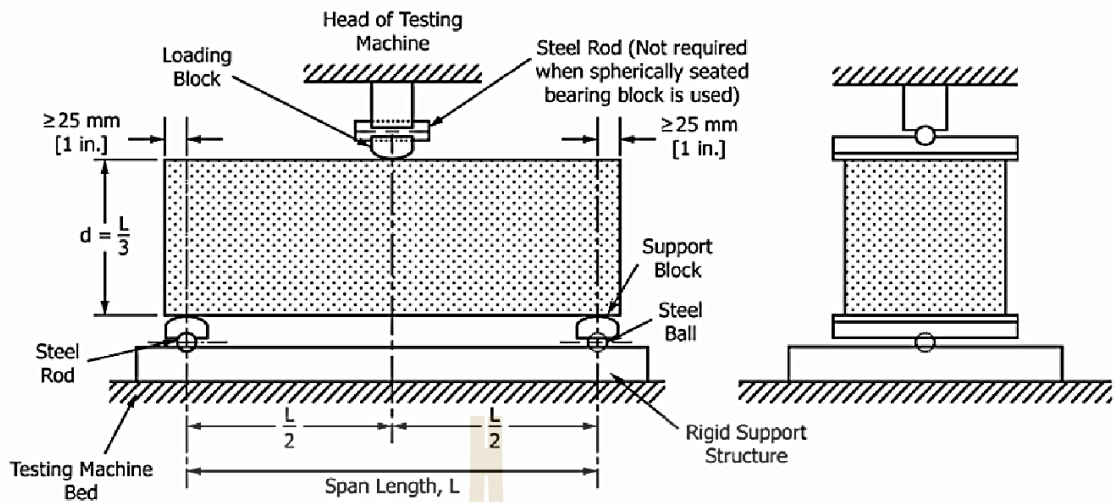


Figure 2.3 Schematic of a suitable apparatus for flexure test by center-point loading method (ASTM (C293-02)).

2.4.2 Four-point bending test

Specifications for standard test method for four-point bending test by American Society for Testing and Materials ASTM (D6272-10). The test method is a bar of rectangular cross section rests on two supports and is loaded at two points or two loading noses, each an equal distance from the adjacent support point. The distance between the loading noses (the load span) is either one third or one half of the support span shown in Figure 2.4.

When a beam is loaded in flexure at two central points and supported at two outer points, the maximum stress in the outer fibers occurs between the two central loading points that define the load span. This stress may be calculated for any point on the load deflection curve for relatively small deflections by the following equation for a load span of one third of the support span:

$$S = PL / bd^2 \quad (2.3)$$

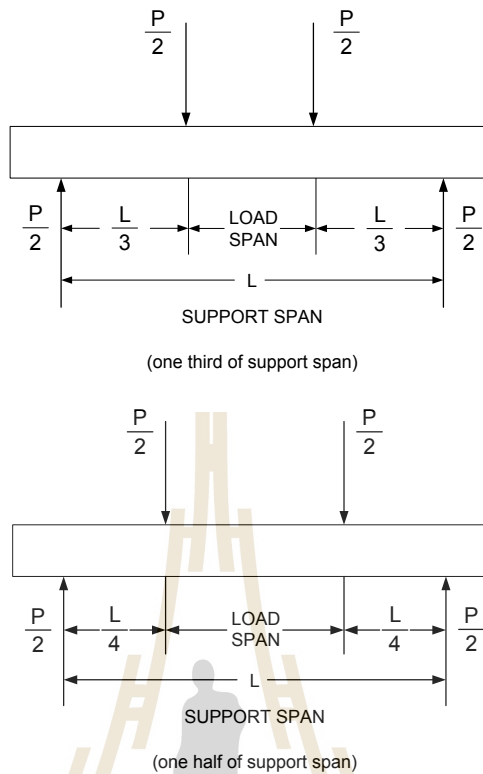


Figure 2.4 Loading Diagram (ASTM (D6272-10)).

For a load span of one half of the support span:

$$S = 3PL / 4bd^2 \quad (2.4)$$

where S is stress in the outer fiber throughout the load span, P is load at a given point on the load-deflection curve, L is support span, b is width of beam and d is depth of beam.

The tangent modulus of elasticity is the ratio, within the elastic limit, of stress to corresponding strain and shall be expressed in megapascals (pounds per square inch). It is calculated by drawing a tangent to the steepest initial straight-line portion of the load-deflection curve and using equation (2.5) for a load span of one third the

support span and equation (2.6) for a load span of one half of the support span, as follows:

$$E_B = 0.21L^3m / bd^3 \quad (2.5)$$

$$E_B = 0.17L^3m / bd^3 \quad (2.6)$$

where E_B is modulus of elasticity in bending, L is support span, B is width of beam tested, D is depth of beam tested and m is slope of the tangent to the initial straight-line.

Obert and Duvall (1967) propose the solution for the maximum stress values at the abutments for compression (bottom of beam) or tension (top of beam) (σ_{\max}) as well as the maximum beam deflection (δ) can be easily calculated using closed form beam equations, as follows:

$$\sigma_{\max} = \gamma S^2 / 2T \quad (2.7)$$

$$\delta = \gamma S^4 / 32ET^2 \quad (2.8)$$

where E is the Young's modulus of the rock, γ is the specific weight and T is thickness.

The maximum stress at the midspan is one half of the maximum stress at the abutments. Therefore, for such a beam with fixed ends and distributed loading, yield is assumed when the maximum tensile stress in the upper part of the beam at the abutments exceeds the tensile strength of the rock. Vertical tensile fractures form at the abutments and the beam becomes simply supported (assuming no slip at the abutments) as shown in Figure 2.5(b) with a maximum tensile stress at the midspan given by

$$\sigma_{\max} = 2\gamma S^2 / 3T \quad (2.9)$$

This stress is now higher than the previous abutment stress, and therefore higher than the rock tensile strength. This leads to subsequent fracturing centered about the midspan as shown by Stimpson and Ahmed (1992). Snyder (1983) considers a laminated rock beam an excavation with a horizontal span by the normal thickness of the single layer under analysis. An elastic beam with no joints and with constant cross section a distribution of compression and tension symmetrical about the horizontal centreline of the beam is found across all plane sections within the beam as shown in Figure 2.5(a).

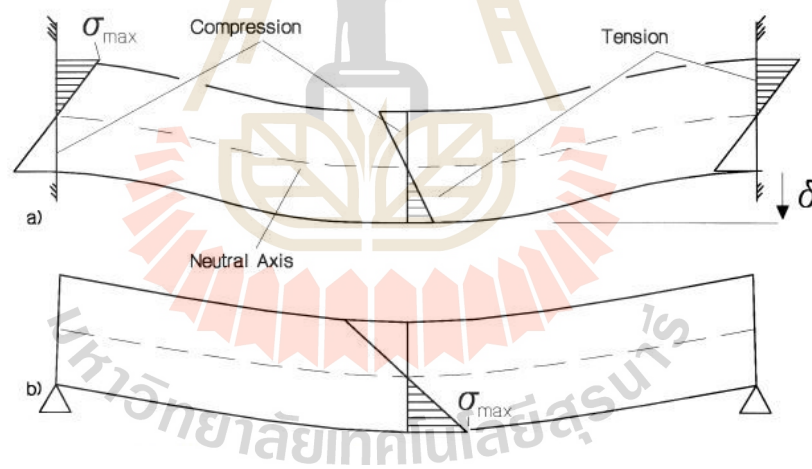


Figure 2.5 Elastic beam with (a) fixed ends and (b) simple (pin) supports. (Snyder, 1983).

Yokoyama (1988) derives a useful formulation for the stress-strain relation in a four-point bending test. His analysis utilizes the experimental measurements of the axial load, P , the strains at the top and bottom of the beam, and the geometry of the device and the beam. The derivations of Yokoyama (1988) lead to

the following values of σ_t and σ_c , the maximum tensile stress and the maximum compressive stress along the beam (fiber stresses)

$$\sigma_t = [dM(\varepsilon_t + \varepsilon_c) + 2M(d\varepsilon_t + d\varepsilon_c)] / (bh^2d\varepsilon_t) \quad (2.10)$$

$$\sigma_c = [dM(\varepsilon_t + \varepsilon_c) + 2M(d\varepsilon_t + d\varepsilon_c)] / (bh^2d\varepsilon_c) \quad (2.11)$$

where $M = 0.5P(L_t - L_c)$ is the bending moment of the beam (L_t and L_c are the spacing of pairs of the loading point for the tensile side and for the compressive side, respectively); ε_t and ε_c are the tensile and compressive strain measured at the top and bottom of the deformed beam, respectively (fiber strains); b is the beam width; h is the beam height; dM , $d\varepsilon_t$ and $d\varepsilon_c$ are the increments of the moment and the strain during the experiment (the differentials between two consecutive steps in the experiment).

2.5 Tensile strength of salt

Beam tests were undertaken by Forster (1967) and Sen (1961) on cylindrical and prismatic rock salt specimens, using either a three-point or four-point loading device, with aim of determining the flexural strength, and hence the tensile strength of the outer fiber of the material. The results of beam bending (three point, four point and uniformly loaded) are in general higher than those from the Brazilian disc tests. Figure 2.6 also confirms that the tensile strength is an exponential function of the length/height ratio of the salt beam. The beam test results showed a significant variation depending on the beam geometry and the petrology.

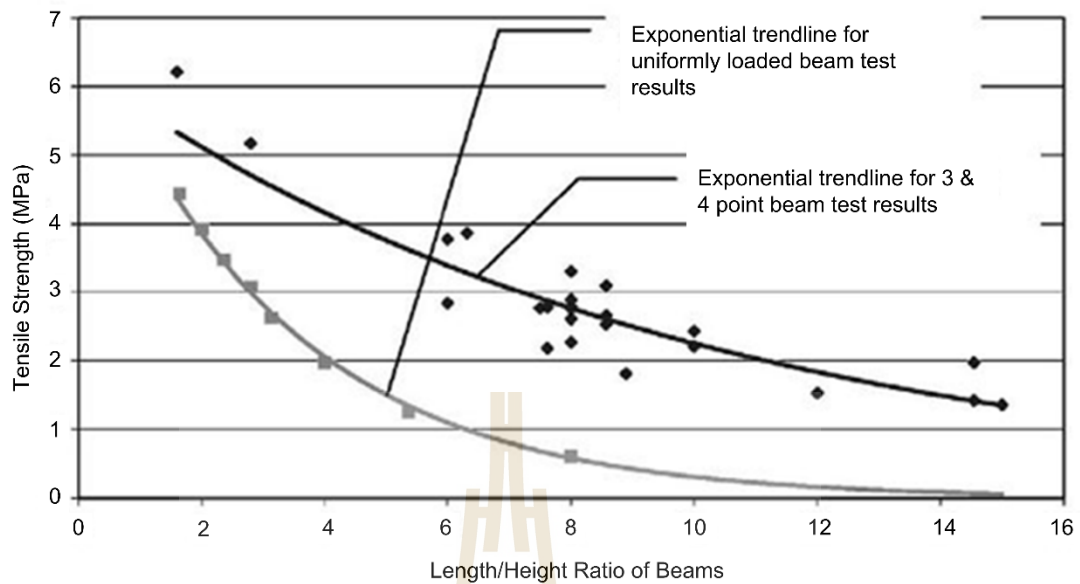


Figure 2.6 Beam tensile test results showing that the UTS is an exponential function of the beam length / height ratio (Forster, 1967; Sen, 1961).

Jaeger et al. (2007) stated that values of the tensile strength determined from bending test on rock are significantly greater than the uniaxial tensile strength. While this effect are not understood, it is well recognized, and the term modulus of rupture is used for the extreme tensile stress determined form a bending test. Obert et al. (1946) include three-point bending of 6 in. length of drill core in their standardized test for studying mine rock, and Pomeroy and Morgans (1956), Berenbaum and Brodie (1959), and Evans (1961) have used bending to study the tensile strength of coal, which is, of course, extremely difficult to test in direct uniaxial tension. Fairhurst (1961) discusses the effects of difficult value for Young's modulus in tension and compression on bending test and describes apparatus for four-point loading. Bending is the simplest method of studying time-dependent behavior of rock, such as creep, and has been used for this purpose by Price and Cosgrove (1964).

Liu et al. (2010) used MTS815 Flex text GT rock mechanics test system and PCI-II three-dimensional acoustic emission test system to study the damage and fractal characteristics of tensile failure in bedded salt rock are studied under indirect and direct tensile test conditions. The tensile strength as well as the correlation between indirect strength and direct tensile strength are obtained. Under indirect and direct tensile test conditions, the spatial distribution of acoustic emission and the damage evolution trend are derived for each stress stage during the full failure process. Based on the fractal column covering method, the fractal characteristic of acoustic emission spatial distribution in rock damage under indirect and direct tensile test conditions are studied. The test results indicate that indirect tensile strength of interlayer salt rock are higher than of pure salt rock and direct tensile strength of pure salt rock are much lower than that of the indirect tensile strength. From the tensile strength difference between the indirect and direct tensile test and failure states, can tell that the tensile strength value from direct tensile test compared with the one from indirect strength test is closer to the virtual strength properties of salt rock. The research results show that with fracture dimensions of damage spatial distribution increasing, the tensile stress decreases following negative exponential law.

2.6 Loading rate effects

Zhang and Wong (2014) discussed the loading mechanisms associated with different loading rates in the bonded-particle model (BPM) and examines the numerical outputs under these different rates for used in which calibration against the results from Brazilian tensile tests have been commonly conducted. The specimens in the numerical analysis of the Brazilian tensile tests are subjected to vertical loading

applied at six different loading rates: 0.005, 0.01, 0.02, 0.08, 0.2 and 0.6 m/s. The induced tensile stress σ_t is calculated as follows:

$$\sigma_t = F/\pi RT \quad (2.12)$$

where F is the compressive force acting on the platens, R and t are the radius and thickness of the Brazilian disk, respectively. The peak value of the induced tensile stress is the Brazilian tensile strength of the test specimen. The results from the Brazilian tensile tests indicate that the Brazilian tensile strength (σ_t) increases as the loading rate increases.

Wisetsaen et al. (2015) studied the effects of loading rate and temperature on tensile strength and deformation of rock salt to determine the time-dependent tensile strength and deformability of the Maha Sarakham salt under temperatures ranging from 273 to 375 K. The ring tension tests are performed under various loading rates which are equivalent to the tensile stress rates induced at the crack initiation point of 3×10^{-5} , 3×10^{-4} , 3×10^{-3} , 3×10^{-2} and 3×10^{-1} MPa/s. The results indicate that the tensile strength increases with the loading rate, and decreases with increasing temperatures.

Chobsranoi and Fuenkajorn (2016) studied the effects of loading rate on tensile strength of Maha Sarakham with various carnallite contents. The time-dependent tensile strengths of rock salt are determined with various carnallite contents ranging from 0 to 95%. The applied loading rates are varied which are equivalent to the tensile stress rates of 10^{-6} to 10^{-3} MPa/s. The results indicate that tensile strengths (σ_t) decrease when the carnallite contents ($C\%$) increase and the stress rates (σ_R) decrease, as shown in Figure 2.7.

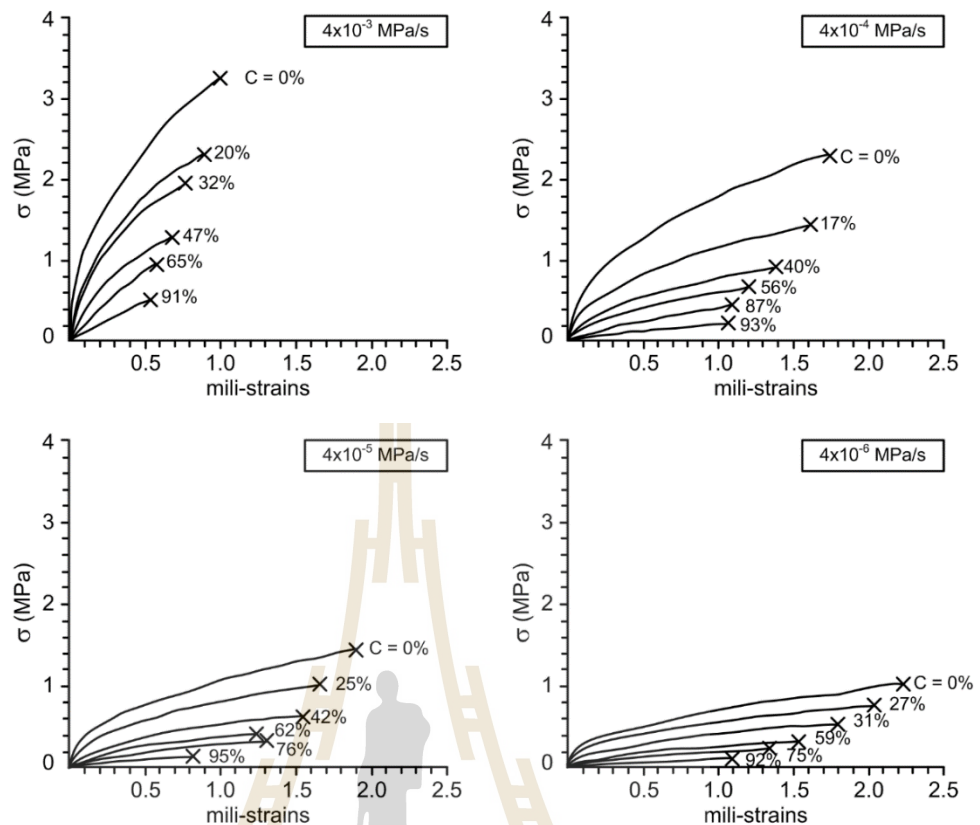


Figure 2.7 Tensile stress-strain curves for various loading rates (Chobsranoi and Fuenkajorn, 2016).

2.7 Cyclic loading of salt in tension

Wang et al. (2016) conducted experiments including Brazillian splitting test, constant average load splitting fatigue test in which we use constant frequency and constant amplitude sine wave individually, and variable mean load splitting fatigue test. The results of Brazilian split fatigue test can be seen that the load-vertical deformation curve is divided into two parts from Figure 2.8. The first part of the curve is a static loading stage, the load increase at the constant rate of 0.05kN/s till the average load level, and it is a linear relationship between load and deformation. The second part of the curve is a splitting fatigue stage; the cyclic load begins with the average load level

at the frequency of 1 Hz. The vertical deformation-load curve of test specimen is shown in Figure 2.9. As can be taken from Figure 2.9, cyclic loading loads 500 times at the first load level and the curve goes through the first stage of the three stages of “sparse-dense-sparse”, resulting in larger deformation. Improving the average load level and load 500 times, the deformation is less than the first level. It remains at the “dense” stage (second stage); thus, although the average load is slightly larger than previous one, the deformation amount is less than the first stage. The deformation of each stage is gradually increasing with the gradual increase of load level. During the last stage of the load level, the deformation increases rapidly in the course of cyclic loading, and the specimen is suddenly destroyed with the increase of deformation. Conclusion of this paper can be used as part of experiences and reference providing for the gas storage operations in salt caverns.

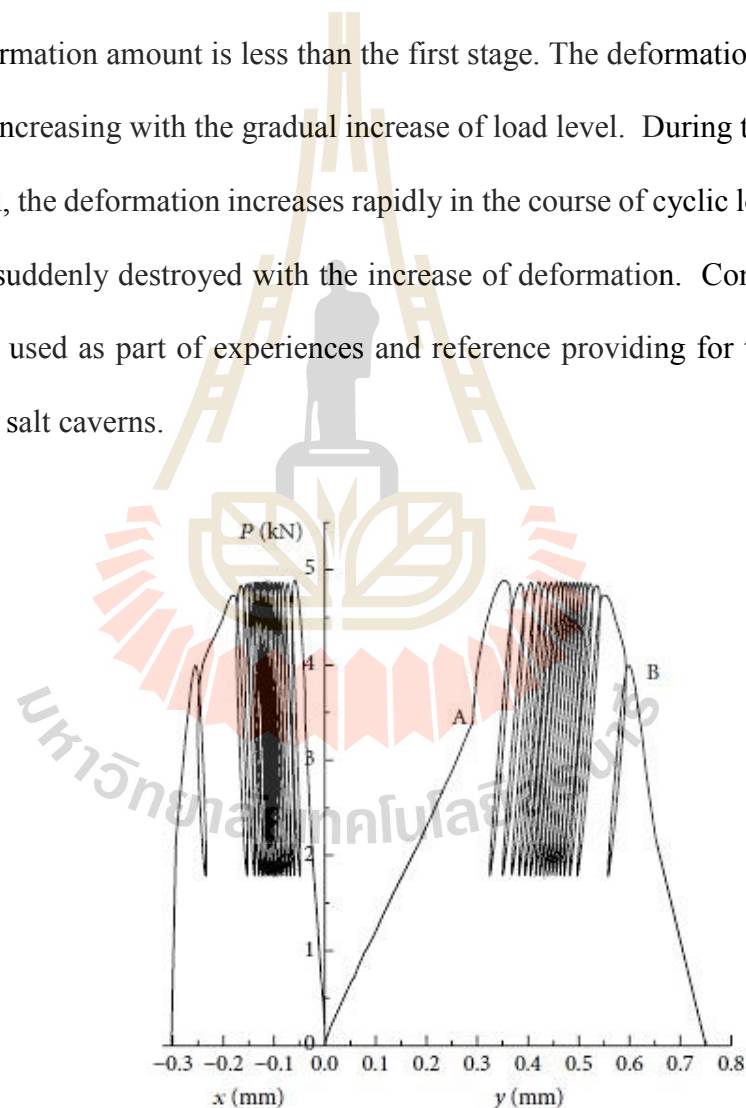


Figure 2.8 Load-deformation curves of Brazilian split fatigue tests of constant average load (Wang et al., 2016).

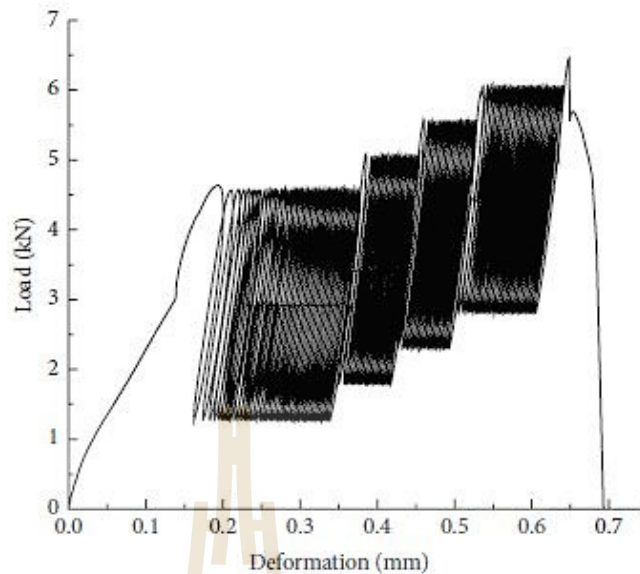


Figure 2.9 Load-deformation curves of Brazilian split fatigue tests of variation average load (Wang et al., 2016).

2.8 Roof stability and design

FLAC (Itasca, 1992) is a two-dimensional explicit finite difference program for engineering mechanics computation. This program simulates the behavior of structures built of soil, rock or other materials that may undergo plastic flow when their yield limits are reached. Materials are represented by elements, or zones, which form a grid that is adjusted by the user to fit the shape of the object to be modeled. Each element behaves according to a prescribed linear or nonlinear stress/strain law in response to the applied forces or boundary restraints. The material can yield and flow and the grid can deform (in large-strain mode) and move with the material that is represented. The explicit, Lagrangian calculation scheme and the mixed-discretization zoning technique used in FLAC ensure that plastic collapse and flow are modeled very accurately. Because no matrices are formed, large two-dimensional calculations can be made

without excessive memory requirements. The drawbacks of the explicit formulation (i.e., small time step limitation and the question of required damping) are overcome to some extent by automatic inertia scaling and automatic damping that do not influence the mode of failure.

Bauer et al. (1998) studied the roof stability of long horizontal leached caverns in bedded rock salt formations, and built a cantilever beam model to calculate the stresses in an interlayer. They thought shear and tensile failure were the main reasons causing roof stability. As shown in Figure 2.10, a 1000 psi tensile strength results in roof width to bed thickness ratios of 1 to 1.4 for 2000 and 1000 psi loads, respectively. Therefore, the bed thickness should be greater than the roof span to be stable during the operational phase of the cavern. The bed thickness less than 70 percent of the length of the roof span are predicted to fracture near middle. When the roof bed fractures and starts to sag from the cavern roof, it will fail in tension if its thickness is less than 30 percent of its length or 15 percent of the cavern roof span.

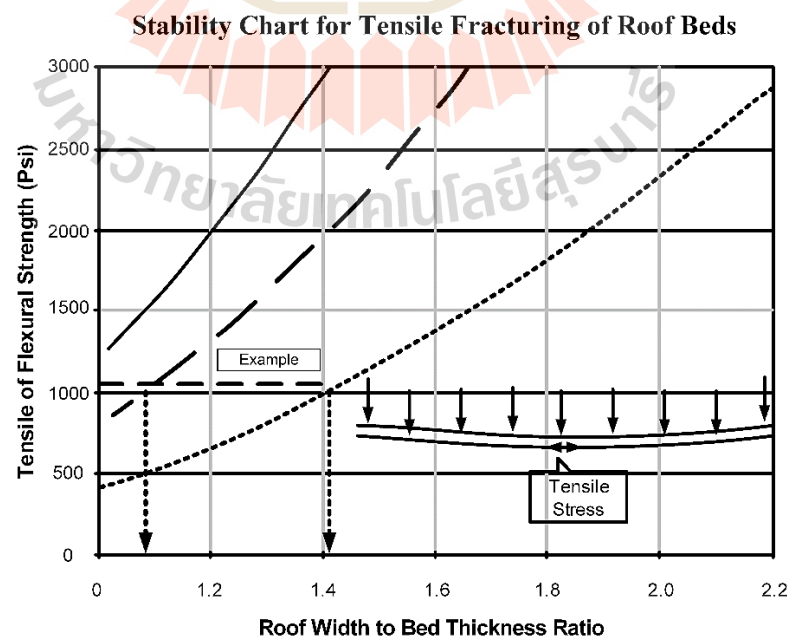


Figure 2.10 Stability chart for tensile fracturing of roof beds (Bauer et al., 1998).

Swift and Reddish (2005) presented numerical modelling analysis of the current stability of the Winsford salt mine by used FLAC software to simulations of the room and pillar in rock salt. A cross section through the Bostock No. 5 panel indicating the geometry of the model is reproduced in Figure 2.11. The pillar sequence run with FLAC assumed a plane-strain situation although this is not modelling the real three-dimensional geometry. The result simulation indicate that the principal load bearing elements are the pillars. Figure 2.12 shows the maximum principal stress redistribution around the central two rooms of the Bostock No. 5 panel and within the adjacent pillars. The plot indicates that the redistribution of stresses is concentrated in the rock close to the mine excavation, and the influence of the excavation reduces with increasing distance from the mine voids. This plot indicates stress concentrations in the pillar centre of approximately 7 MPa, increasing to 9 MPa at the pillar abutments. The pillar core as previously defined can be clearly identified, representing the central 8 m of the pillar. The central part of the immediate roof of the room shows stress concentrations of 4 MPa. Stress concentrations increase towards the room corners, as would be expected, to a maximum of 9 MPa. Safety factors for the central pillar and adjacent rooms have been calculated as a means of illustrating the relative stability of the mine structures. Strength/stress ratios of 3 are shown in the side walls and immediate roof this would be considered to indicate very stable conditions in mining situations. However, towards the central pillar section and further in to the roof strata, the strength/stress ratio increases to in excess of 9 indicating a very stable pillar core and mine roof.

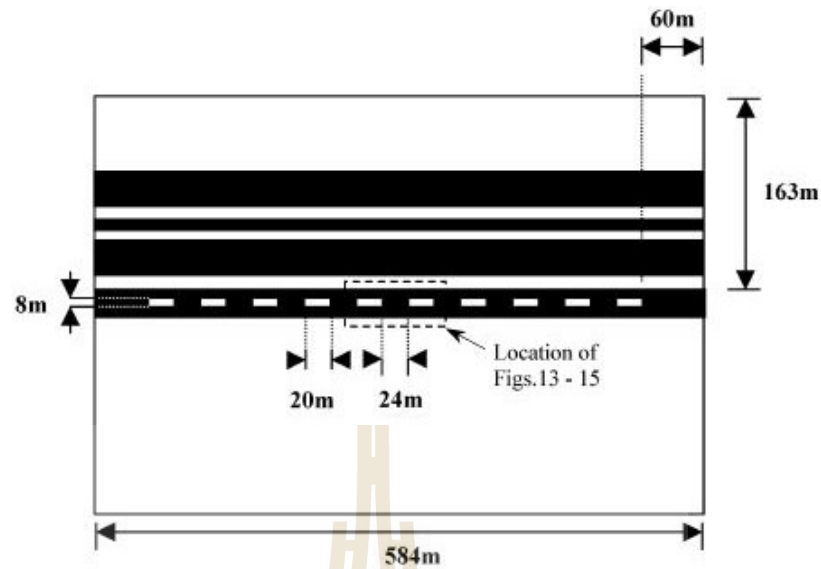


Figure 2.11 Cross section through the Bostock No. 5 panel showing model configuration (Swift and Redish, 2005).

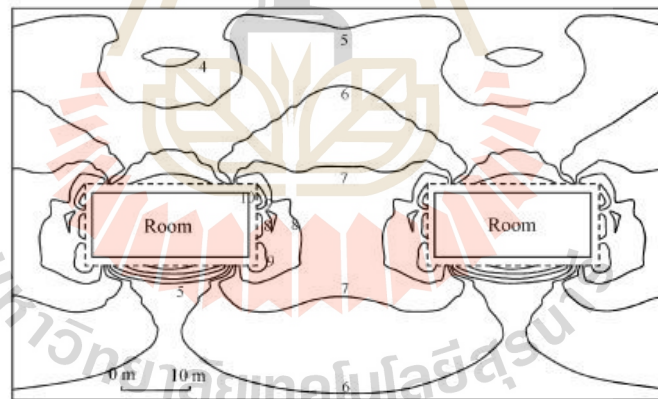


Figure 2.12 Maximum principal stress distribution around central two rooms in the Bostock No. 5 panel (MPa) (Swift and Reddish, 2005).

Han et al. (2006) studied the tensile failure in anhydrite layer implies an increase in the vertical displacement of the cavern roof, and thus more damage in the salt itself (Figure 2.13). Calculation indicates that, when overburden becomes soft, the vertical displacement of the cavern roof increase to as much as 0.14m (0.46ft), from 0.01m

(0.0328ft) in the baseline study. Furthermore, the interface slippage between the salt layer and the anhydrite layer now covers the entire cross section of cavern. This simulation clearly demonstrates that the overburden stiffness is a significant factor in evaluating roof stability of caverns.

Wang et al. (2012) build up the numerical simulation model. According to the cavern dimensions and properties of rock salt and non-salt, the 3D numerical model of bedded rock salt cavern gas storage is established by Flac^{3D} software. The results show that buried depth, roof span and gas pressure have significant effects on the roof stability and can be controlled in the designs and operations. Therefore, the proper buried depth, strictly designed cavern roof and short time of low gas pressure are recommended in the design of bedded rock salt cavern gas storage. As the stiffness and strength of non-salt are usually very low, a relative thick roof salt is recommended to maintain the cavern roof stability.

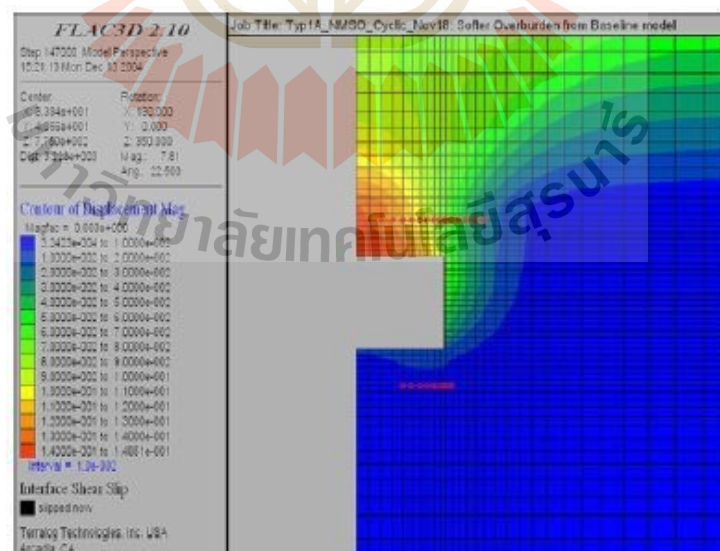


Figure 2.13 Rock displacement around a cavern with reduced overburden stiffness (Han et al., 2006).

Wang et al. (2015) improved calculation efficiency by used to FLAC 3D for the model symmetry. The model dimensions are 900 x 800 x 400 m in length, height, and width, respectively. The target of rock salt formation is located with depth from 1900 m to 2098 m. The thickness of top and bottom mudstone layers are about 300 m. The bottom of the model has zero displacement boundary. The relative horizontal and vertical displacements of the bottom are all zero. The left and right sides of the model both have zero horizontal displacement boundaries.

Yang et al. (2016) studied mechanical theory of the roof interbed in terms of land subsidence brought by brine in salt cavity after removal, and also they listed some possible failures of the interbed such as tension failure, shear failure, crushing failure, and plastic yield. Then, roof peel, tension failure and maximum deflection were obtained by FLAC software, but this study did not explain the detailed mechanical theory for kinds of failure, and the influence of horizontal stress on roof collapse also could not be introduced in their study.

CHAPTER III

SAMPLE PREPARATION

3.1 Introduction

This chapter describes the rock salt sample preparation procedure to be used in the four point bending test. Three test series are performed: static loading tests, cyclic loading tests and constant loading rate tests.

3.2 Sample preparation

The tested samples have been obtained from underground openings of ASEAN Potash Mining Co., Ltd. (APMC). They belong to the Lower Salt Member of the Maha Sarakham formation. Warren (1999) describes the origin and geological structures of the Maha Sarakham salt. The samples contain pure halite. The specimens used for four point bending tests are therefore prepared as rectangular blocks with nominal dimensions of $50 \times 50 \times 200 \text{ mm}^3$ (Figure 3.1). A high speed rock cutting device is used. Organic oil is used as cutting fluid. Figure 3.2 shows some specimens prepared for the four point bending test.

The ratio of specimen length to specimen diameter (L/D) is 4.0. The eight, twelve and seven salt specimens are prepared for static loading tests, cyclic loading tests and constant loading rate tests (Table 3.1). Tables 3.2 to 3.4 show the summary of salt specimen dimensions prepared for each test type.

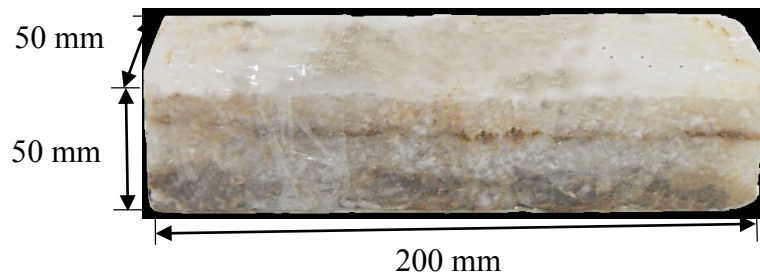


Figure 3.1 Example of prismatic salt specimens with nominal dimensions of $50 \times 50 \times 200 \text{ mm}^3$.

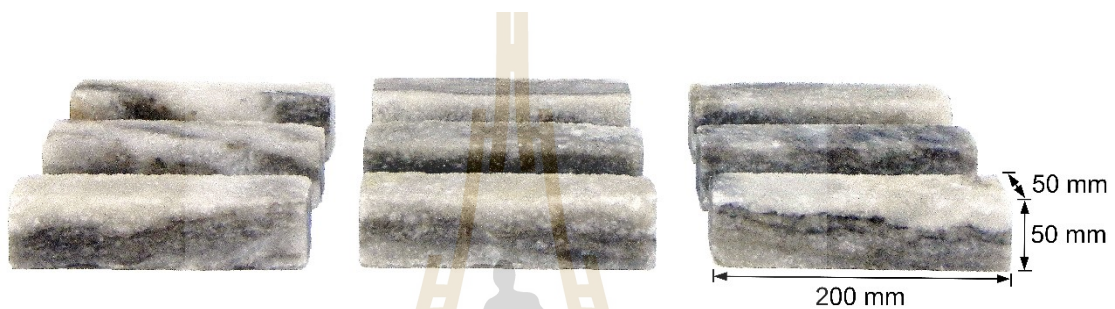


Figure 3.2 Some salt specimens prepared for four point bending test with $L/D = 4.0$.

3.3 Strain gage installation

A strain gage (TML, PFL-20-11-1L, 20 mm) is installed to measure tensile strains at the center of the specimen in horizontal. The main axis of the specimen is parallel to the bedding planes (Figure 3.3). Gage length is 20 mm, and gage factor is $2.13 \pm 1\%$.

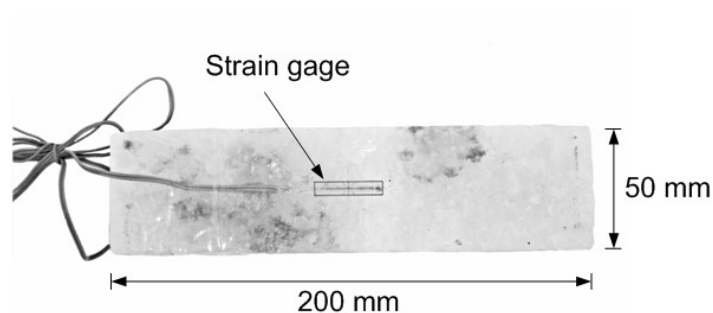


Figure 3.3 Examples of prismatic salt specimen with strain gage position salt specimens prepared for four point bending test.

Table 3.1 Nominal dimensions of specimens for difference tests.

| Methods | L/D ratio | Nominal Width (mm) | Nominal Length (mm) | Number of Specimens |
|-----------------------------|-----------|--------------------|---------------------|---------------------|
| Static loading tests | 4.0 | 50 | 200 | 8 |
| Cyclic loading tests | 4.0 | 50 | 200 | 15 |
| Constant loading rate tests | 4.0 | 50 | 200 | 7 |

Table 3.2 Salt specimens prepared for static loading tests.

| Specimen Number | Average Width (mm) | Average Height (mm) | Average Length (mm) | Weight (g) | Density (g/cc) |
|-----------------|--------------------|---------------------|---------------------|------------|----------------|
| RS-Creep-01 | 52.01 | 48.81 | 199.31 | 1083.0 | 2.14 |
| RS-Creep-02 | 49.31 | 48.48 | 196.31 | 999.5 | 2.13 |
| RS-Creep-03 | 49.81 | 49.57 | 200.37 | 1077.5 | 2.18 |
| RS-Creep-04 | 50.31 | 49.96 | 200.30 | 1069.5 | 2.12 |
| RS-Creep-05 | 49.76 | 49.69 | 200.52 | 1034.5 | 2.10 |
| RS-Creep-06 | 49.95 | 49.90 | 199.83 | 1059.0 | 2.13 |
| RS-Creep-07 | 50.23 | 49.89 | 199.93 | 1062.0 | 2.10 |
| RS-Creep-08 | 49.95 | 49.90 | 199.83 | 1059.0 | 2.13 |

Table 3.3 Salt specimens prepared for cyclic loading tests.

| Specimen Number | Average Width (mm) | Average Height (mm) | Average Length (mm) | Weight (g) | Density (g/cc) |
|-----------------|--------------------|---------------------|---------------------|------------|----------------|
| RS-Cyclic-01 | 50.27 | 50.45 | 199.97 | 1075.0 | 2.12 |
| RS-Cyclic-02 | 50.36 | 48.95 | 198.28 | 1043.0 | 2.13 |
| RS-Cyclic-03 | 50.93 | 50.08 | 198.83 | 1081.0 | 2.13 |
| RS-Cyclic-04 | 50.72 | 49.56 | 202.74 | 1086.5 | 2.13 |
| RS-Cyclic-05 | 50.35 | 50.37 | 202.53 | 1081.5 | 2.11 |

Table 3.3 Salt specimens prepared for cyclic loading tests (continuous).

| Specimen Number | Average Width (mm) | Average Height (mm) | Average Length (mm) | Weight (g) | Density (g/cc) |
|-----------------|--------------------|---------------------|---------------------|------------|----------------|
| RS-Cyclic-06 | 49.03 | 49.79 | 200.15 | 1027.5 | 2.10 |
| RS-Cyclic-07 | 50.24 | 50.14 | 203.33 | 1077.0 | 2.10 |
| RS-Cyclic-08 | 50.19 | 49.98 | 199.31 | 1051.0 | 2.11 |
| RS-Cyclic-09 | 50.23 | 40.26 | 199.90 | 1086.0 | 2.16 |
| RS-Cyclic-10 | 50.20 | 50.11 | 199.64 | 1079.0 | 2.14 |
| RS-Cyclic-11 | 49.92 | 50.04 | 199.90 | 1087.5 | 2.18 |
| RS-Cyclic-12 | 48.63 | 50.13 | 199.60 | 1034.0 | 2.13 |

Table 3.4 Salt specimens prepared for constant loading rate tests.

| Specimen Number | Average Width (mm) | Average Height (mm) | Average Length (mm) | Weight (g) | Density (g/cc) |
|-----------------|--------------------|---------------------|---------------------|------------|----------------|
| RS-Rate-01 | 52.01 | 48.81 | 199.31 | 1083.0 | 2.14 |
| RS-Rate-02 | 49.31 | 48.48 | 196.31 | 999.0 | 2.13 |
| RS-Rate-03 | 49.81 | 49.57 | 200.37 | 1077.5 | 2.18 |
| RS-Rate-04 | 50.31 | 49.96 | 200.30 | 1069.5 | 2.12 |
| RS-Rate-05 | 49.76 | 49.69 | 200.52 | 1034.5 | 2.10 |
| RS-Rate-06 | 49.95 | 49.90 | 199.83 | 1059.0 | 2.13 |
| RS-Rate-07 | 50.23 | 49.89 | 199.93 | 1062.0 | 2.10 |

CHAPTER IV

LABORATORY TESTING METHOD AND RESULTS

4.1 Introduction

The objective of four-point bending test is to determine the maximum tensile stress of rock salt. This chapter describes the test methods and results of the bending tensile strength of the Maha Sarakham salt under various loading configurations. The testing procedures and equipment are also described.

4.2 Test method

The test method and calculation follow the standard practice (ASTM D6272-10). Figure 4.1 shows the loading directions which are normal to the bedding plane. A data logger (TC-32K) connected with the switching box (Type B-2760) is used to monitor the induced tensile strains while loading (Figure 4.2). The salt specimen deflections of the four point creep tests and loading rate tests are monitored by dial gage with high precision (± 0.01 mm) which are placed in vertical at the center of specimen. The creep specimens are subjected to the constant tensile stresses of 0.5, 0.75, 1.0 and 1.25 MPa. Each specimen is tested up to 21 days. The readings are made every one minute for the first hour. After that the reading interval are gradually increased to every hour. The induced tensile stress can be calculated by (ASTM D6272-10). :

$$\sigma_t = PL/bd^2 \quad (4.1)$$

where σ_t is tensile stresses, P is the applied load, L is support span (180 mm), b is specimen width (50 mm), and d is specimen thickness (50 mm)

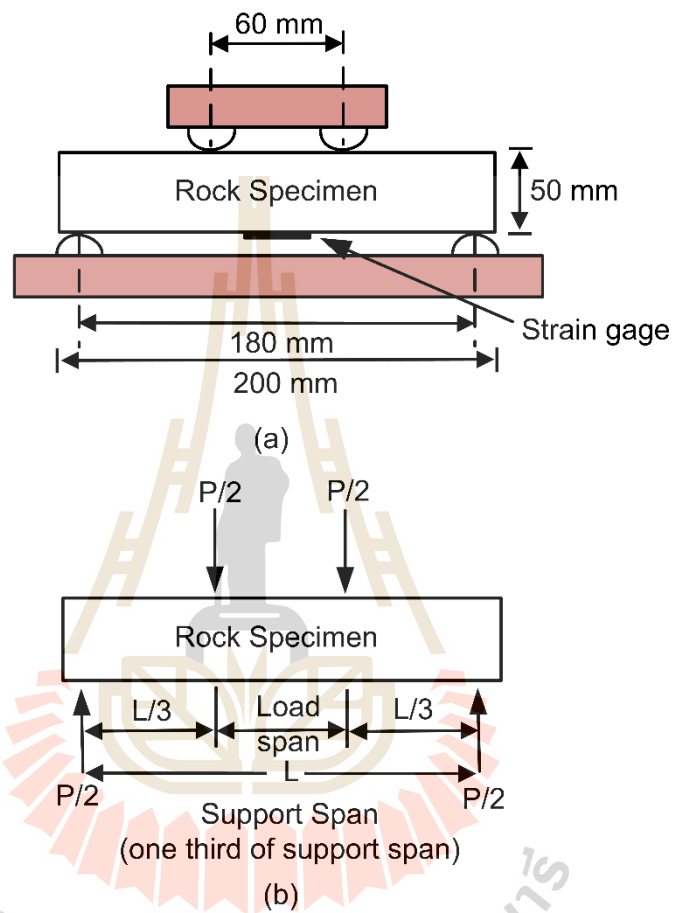


Figure 4.1 Test arrangement for four-point bending test (ASTM (D6272-10)).

The cyclic loading tests are performed for two frequencies: 1 and 10 mHz. The loading-unloading frequency and amplitude in the test are controlled by the pressure pump.

The loads for the rate-controlled testing are applied under five constant magnitudes which are equivalent to the induced stress rates from 4×10^{-3} MPa/s to 4×10^{-7} MPa/s at the center of the specimen. The specimen deformations are monitored and are used to calculate the principal strains during loading. The readings are recorded every 50 N of load increment until failure.

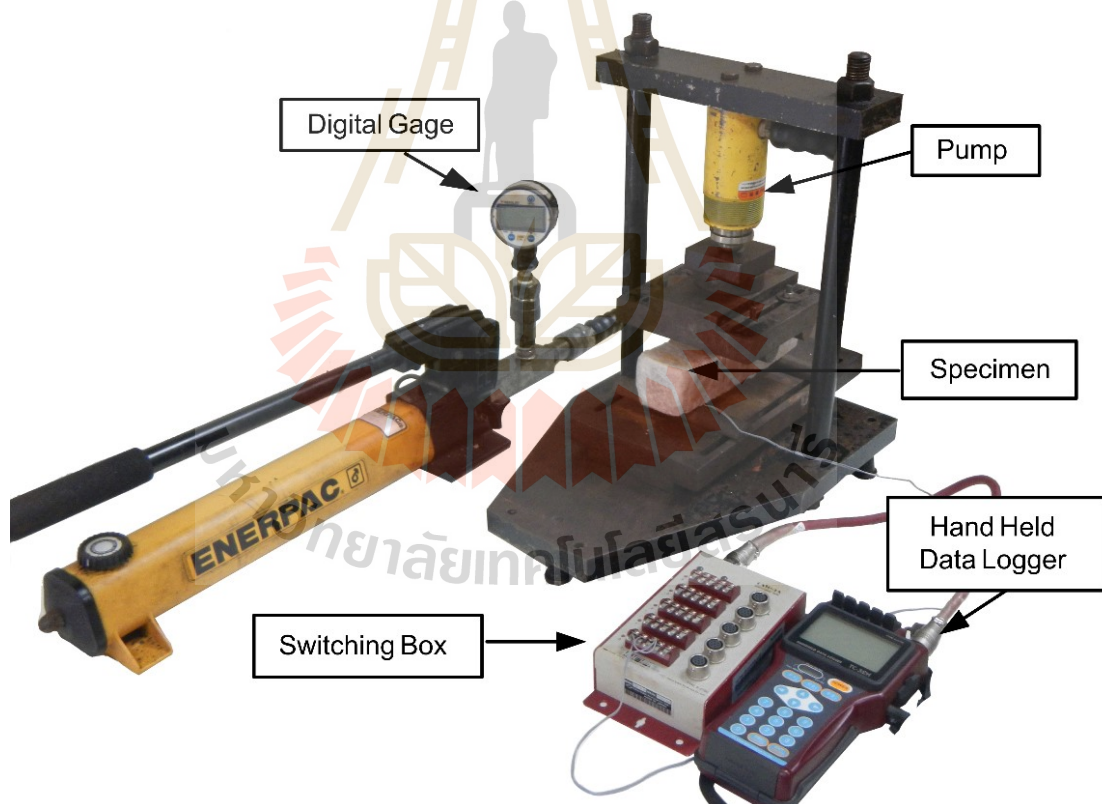


Figure 4.2 Four point bending test equipment.

4.3 Four point bending with constant loading test

For this test series the tests are determined the time-dependent behavior of salt specimens for constant stresses from 0.5, 0.75, 1.0 to 1.25 MPa. Eight specimens are tested up to 21 days. Table A.1 in Appendix A show the applied load for this test. The results are presented in forms of tensile strains and compressive strains as a function of time in Figures 4.3 and 4.4. The curves show the instantaneous and transient creep phases of the rock salt. The creep deformation for the pure halite specimens agrees well with those of Fuenkajorn (2007) who performs compression creep testing on the same salt. The results indicate that the tensile stresses (σ_t) of salt and the tensile creep strains are higher than the compressive creep strains. Larger creep strains are obtained for the specimens with higher tensile stress. Figure 4.5 shows the deflection as a function of time. From the diagram it is clear that the deflection increases with increasing tensile stresses. The discrepancies of the creep results are probably due to the intrinsic variability of the salt specimens. The tensile stress is defined as negative values and the compressive stress is defined as positive values.

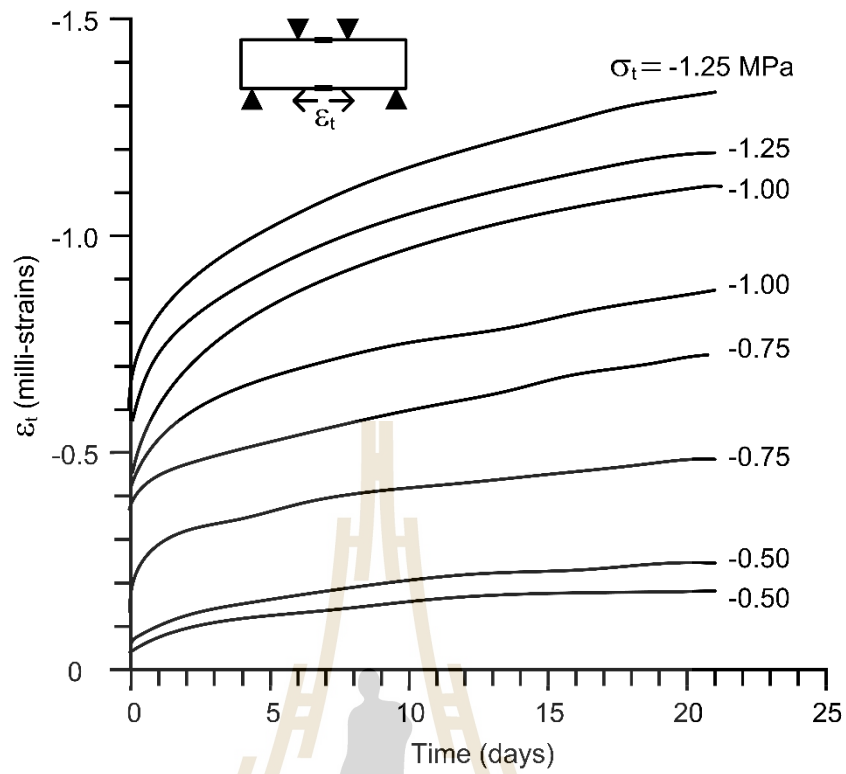


Figure 4.3 Tensile strain (ϵ_t) as a function of time (t) for constant loading under tensile stresses of 0.5, 0.75, 1.0 and 1.25 MPa.



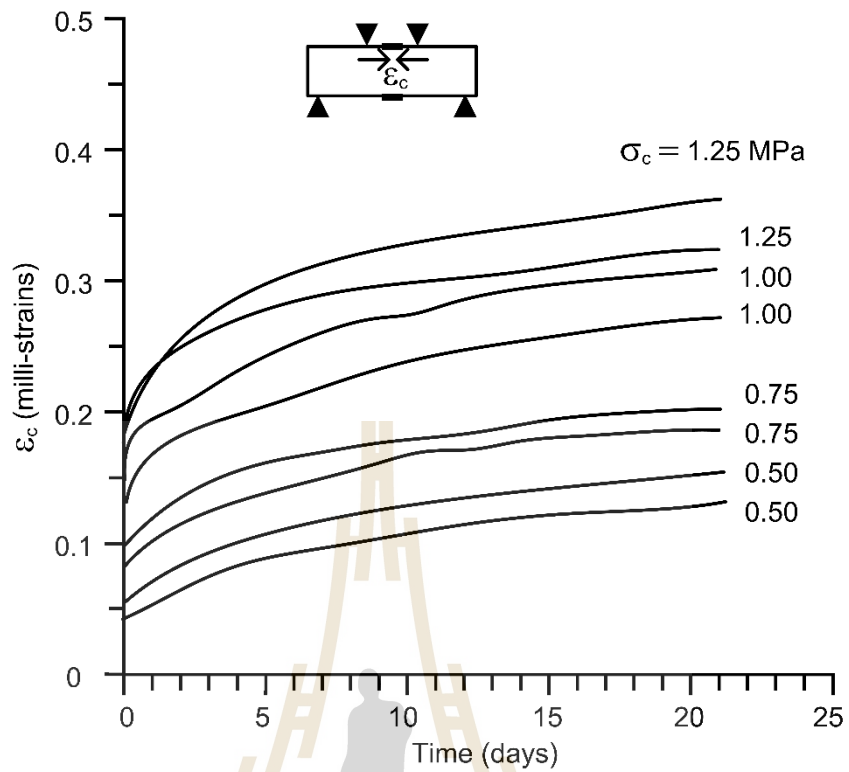


Figure 4.4 Compressive strain (ϵ_c) as a function of time (t) for constant loading under compressive stresses of 0.5, 0.75, 1.0 and 1.25 MPa.

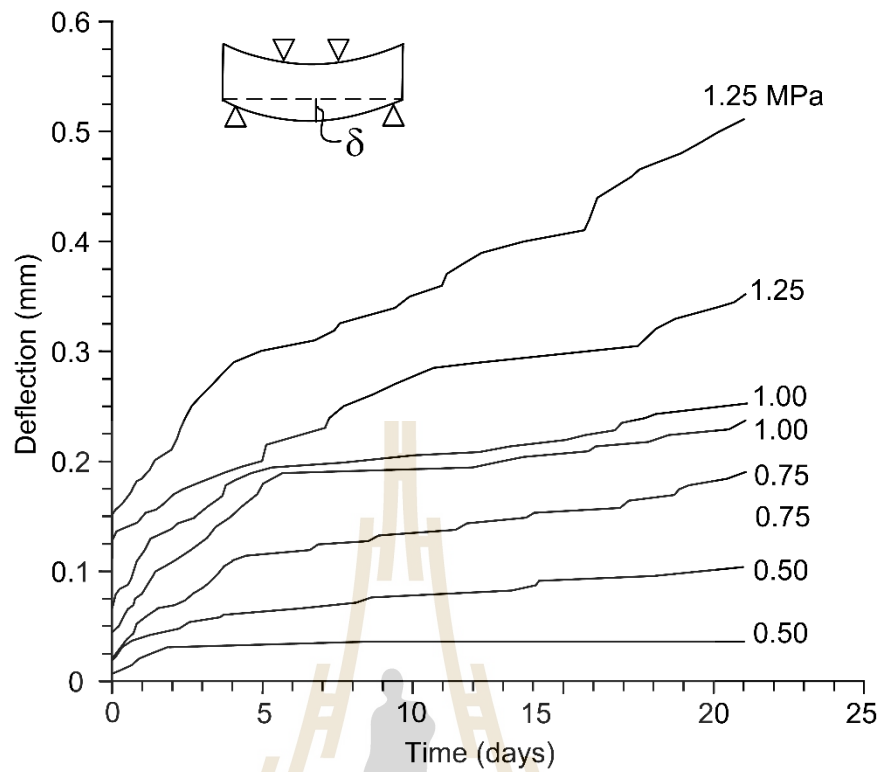


Figure 4.5 Deflection as a function of time (t) for static loading under tensile stresses of 0.5, 0.75, 1.0 and 1.25 MPa.

4.4 Four point bending with cyclic loading test results

The maximum tensile stresses used in the cyclic loading test vary among salt specimens from 1.21 MPa to 3.20 MPa. The loading frequencies range from 1 mHz to 10 mHz. Table A.2 in Appendix A show the applied load for this test. The tensile stress-strain curves measured during loading for all specimens are given in Figures 4.6 to 4.9. It can be interpreted as hysteresis loops compaction and hardening behavior of specimens. This is because the salt behave as a strain-hardening material. Figures 4.10 and 4.11 show the tensile strain-time curves compiled from loci of the loading cycles for loading frequencies of 1 mHz and 10 mHz. The curves show the transient, steady-state and tertiary creep phases which are similar to those obtained from static creep testing. The cyclic loading test results indicate that the maximum number of loading cycles increases with decreasing the maximum applied stresses (amplitudes). Similar behavior also observed from the compression cyclic loading test results obtained by Fuenkajorn and Phueakphum (2010). The accumulated tensile strain, fatigue tensile stresses (S) and time are monitored during loading. Figure 4.12 shows the decrease of the failure (fatigue, S) stresses as the number of loading cycle (N) increases, which can be represented by a logarithmic equation as:

$$S = - 0.209\ln(N) + 3.071 \text{ MPa} \quad (\text{for } 10 \text{ mHz}) \quad (4.2)$$

$$S = - 0.191\ln(N) + 2.826 \text{ MPa} \quad (\text{for } 1 \text{ mHz}) \quad (4.3)$$

For each specimen, the elastic moduli calculated from the series of unloading curves are plotted as a function of loading cycles in Figures 4.13 and 4.14. For all stress levels, the salt elasticity decreases as the number of loading cycles increases. The calculated elastic moduli values range from 0.47 GPa to 1.93 GPa. They, however, tend to be independent of the applied maximum loads used here, as also evidenced by the

normalized elastic moduli (E/E_0) as a function of N in Figures 4.15 and 4.16, where E_0 is the modulus measured during the first loading cycle.

Table 4.1 Stresses and strains at failure for cyclic loading tests.

| f (mHz) | Maximum tensile stresses (MPa) | ϵ_t (milli-strains) | Number of cycles |
|--------------|-----------------------------------|---------------------------------|------------------|
| 10 | -3.20 | -0.78 | 0.5 |
| | -2.80 | -1.09 | 7 |
| | -2.55 | -1.25 | 15 |
| | -2.40 | -1.32 | 17 |
| | -2.24 | -1.38 | 55 |
| | -1.99 | -1.46 | 62 |
| | -1.87 | -1.58 | 810 |
| | -1.22 | -1.99 | 4814 |
| 1 | -2.90 | -0.76 | 0.5 |
| | -2.56 | -1.03 | 6 |
| | -2.40 | -1.10 | 10 |
| | -2.25 | -1.19 | 27 |
| | -1.99 | -1.33 | 42 |
| | -1.88 | -1.53 | 281 |
| | -1.40 | -1.54 | 1021 |

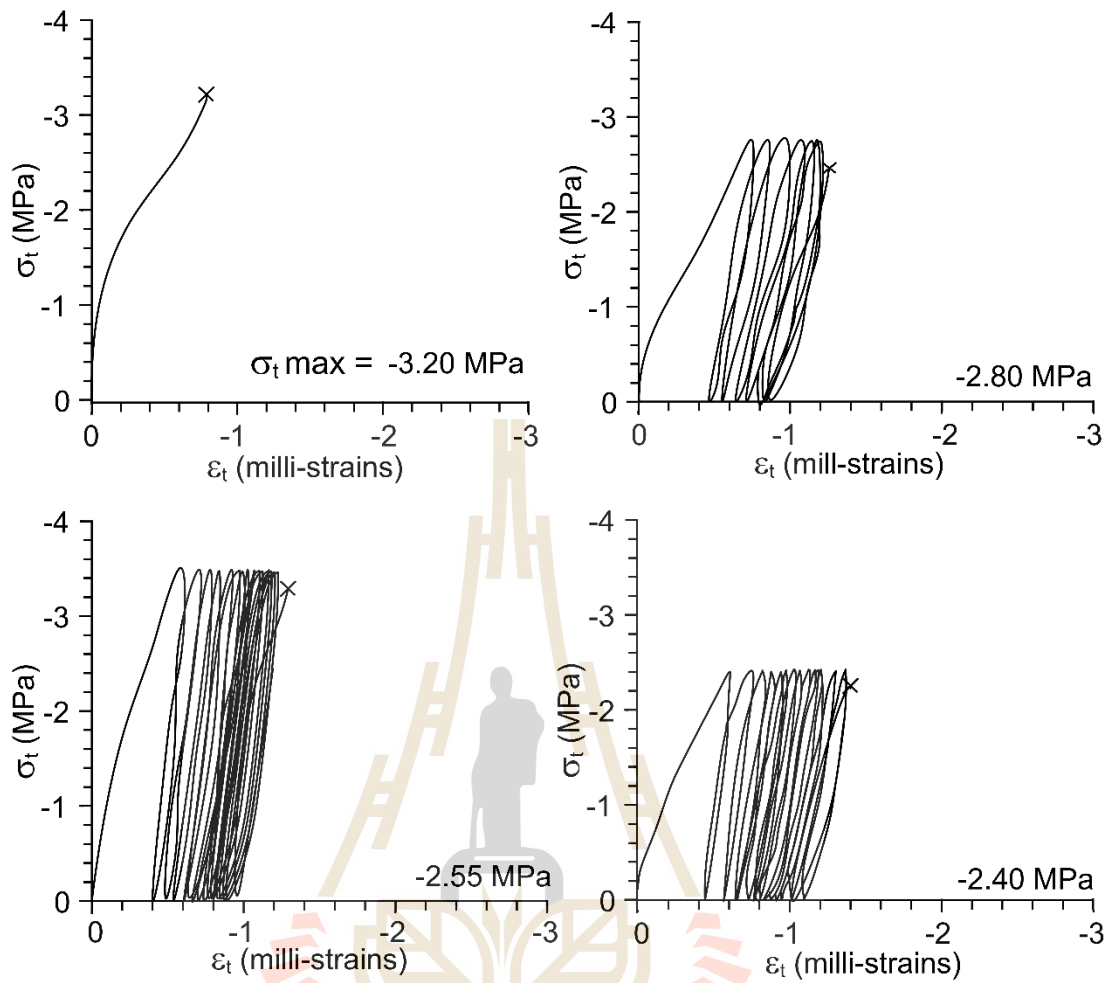


Figure 4.6 Applied tensile stresses (σ_t) plotted as a function of tensile strain (ϵ_t) for $f = 10 \text{ mHz}$.

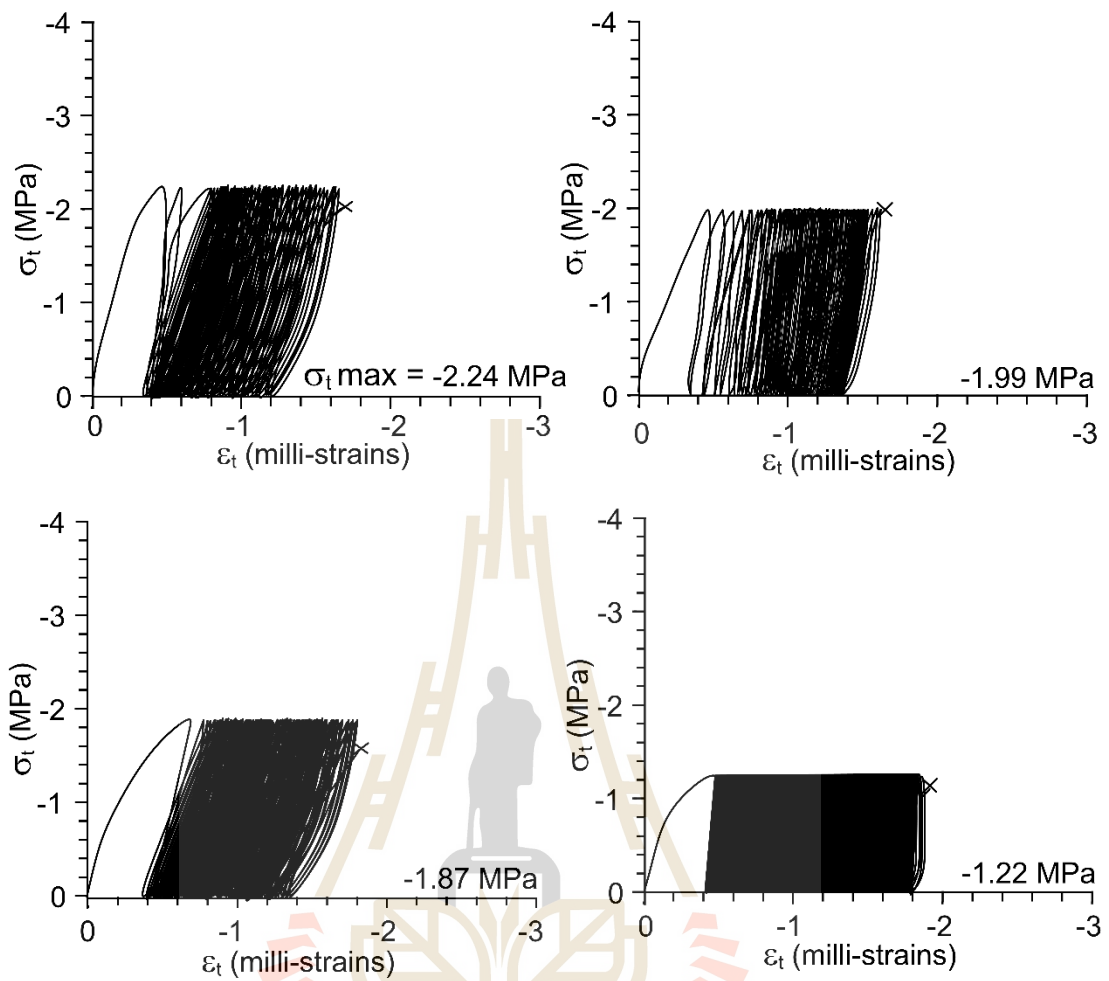


Figure 4.7 Applied tensile stresses (σ_t) plotted as a function of tensile strain (ε_t) for $f = 10$ mHz.

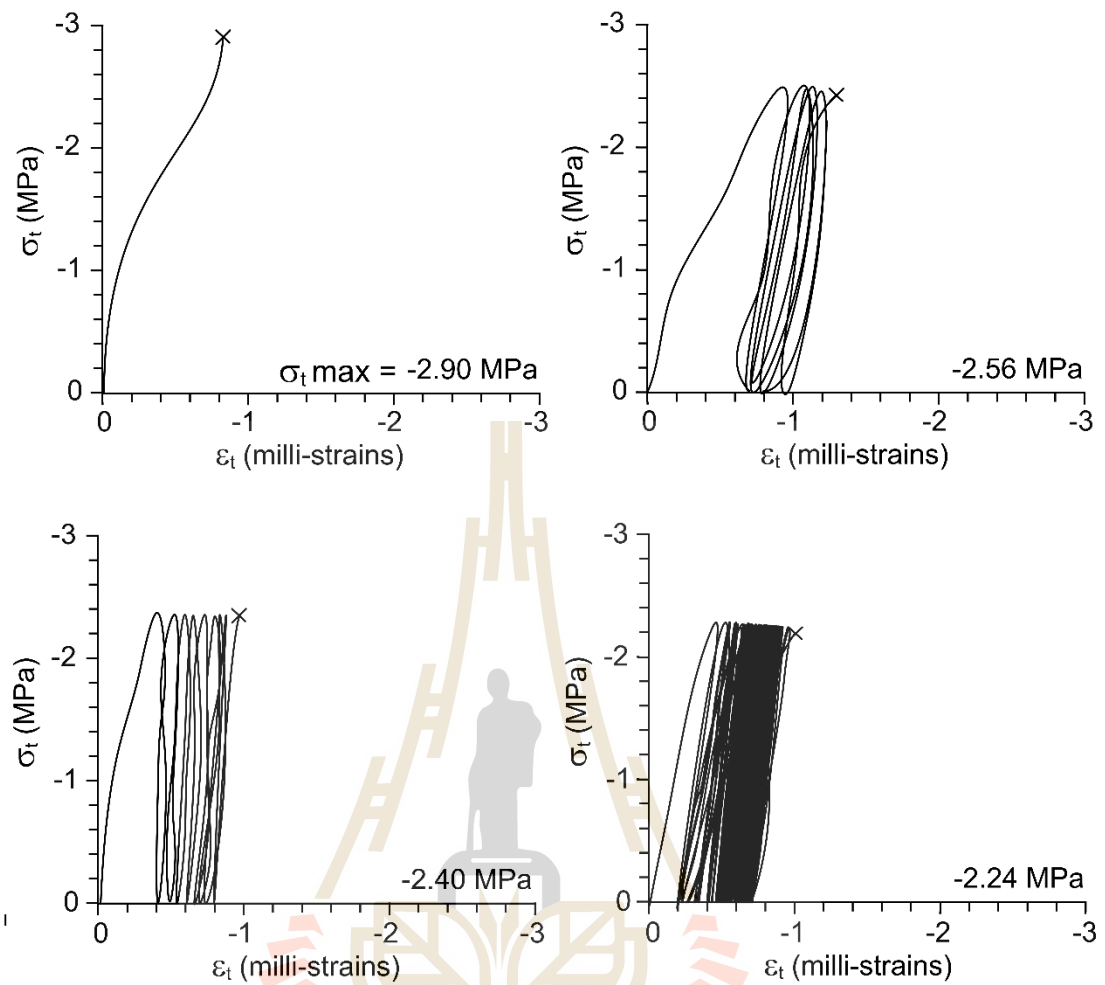


Figure 4.8 Applied tensile stress (σ_t) plotted as a function of tensile strain (ϵ_t) for $f = 1$ mHz.

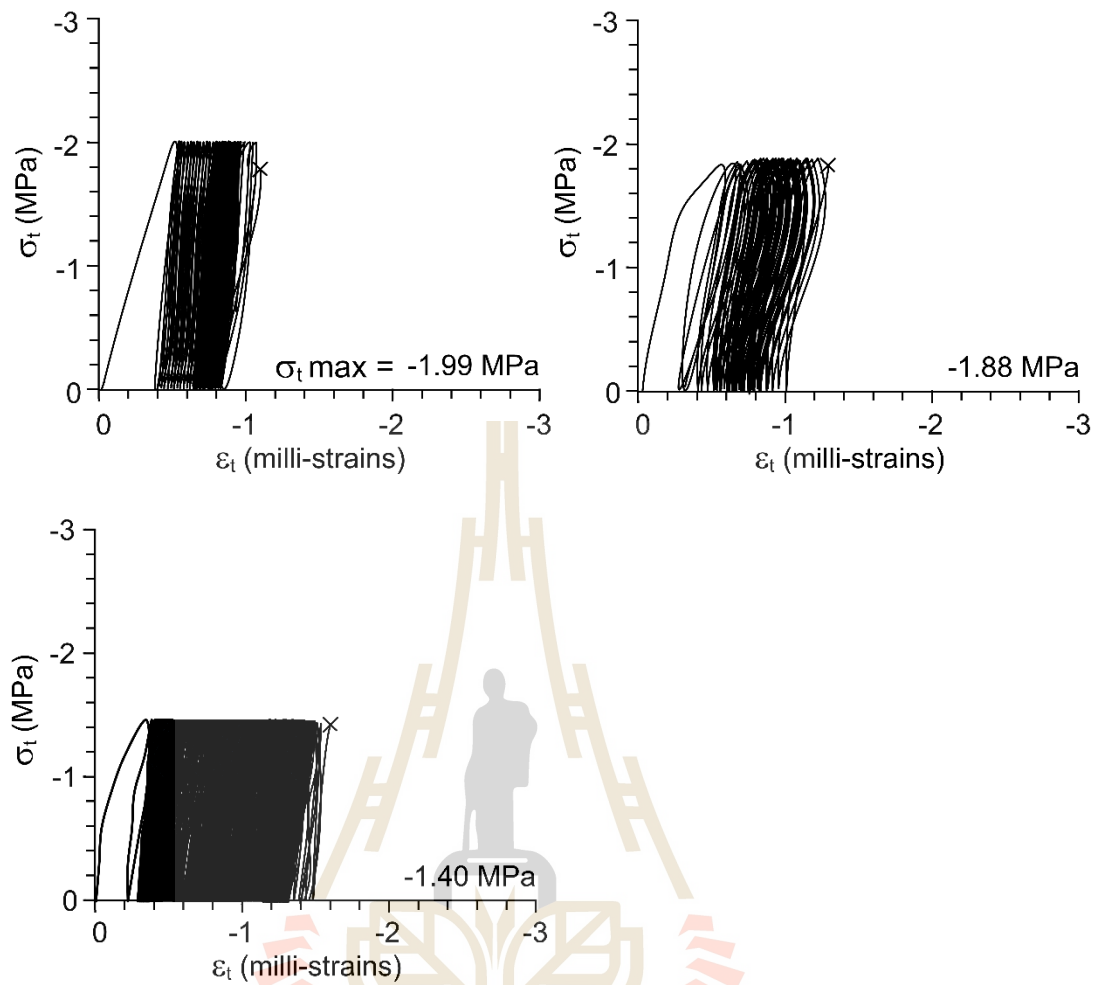


Figure 4.9 Applied tensile stress (σ_t) plotted as a function of tensile strain (ϵ_t) for $f = 1 \text{ mHz}$.

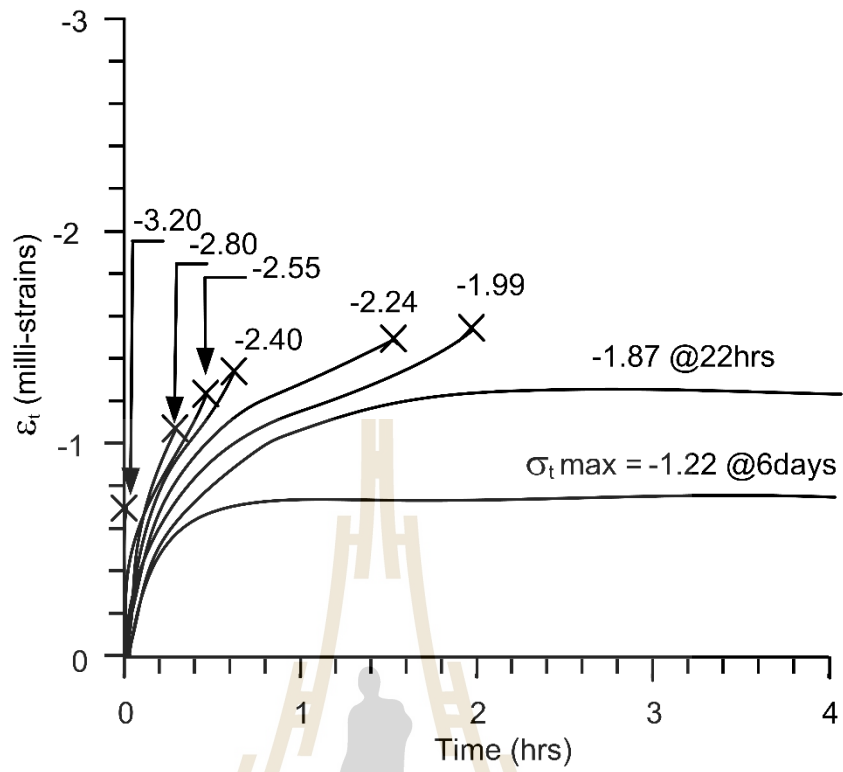


Figure 4.10 Accumulated tensile strain (ϵ_t) as a function of time for $f = 10$ mHz.



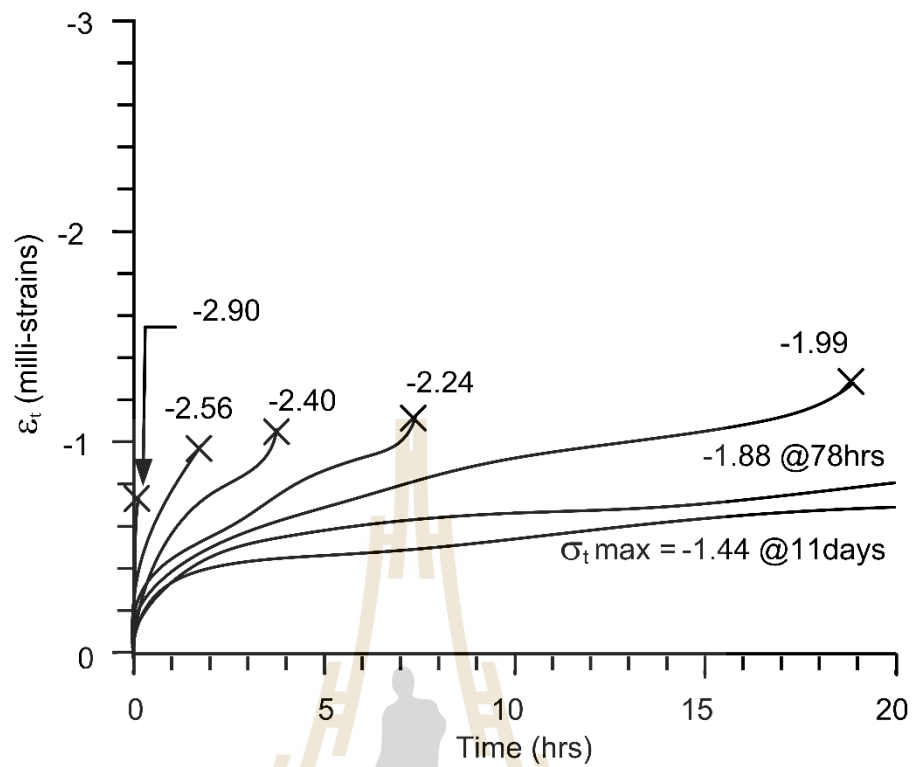


Figure 4.11 Accumulated tensile strain (ϵ_t) as a function of time for $f = 1$ mHz.



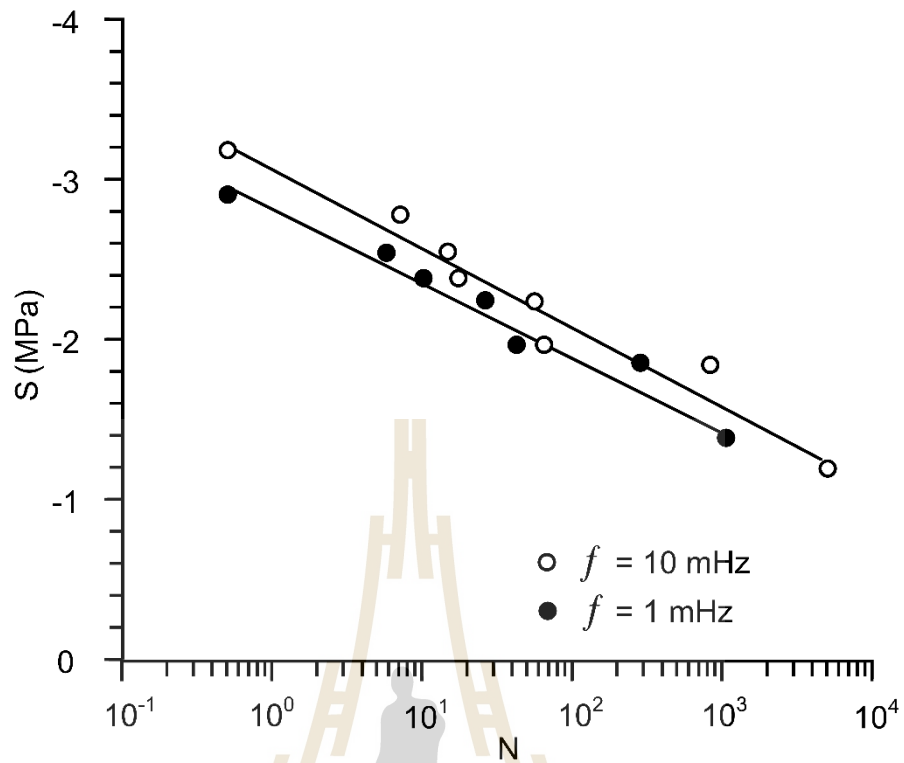


Figure 4.12 Fatigue tensile strengths (S) as a function of number of loading cycles at failure (N)

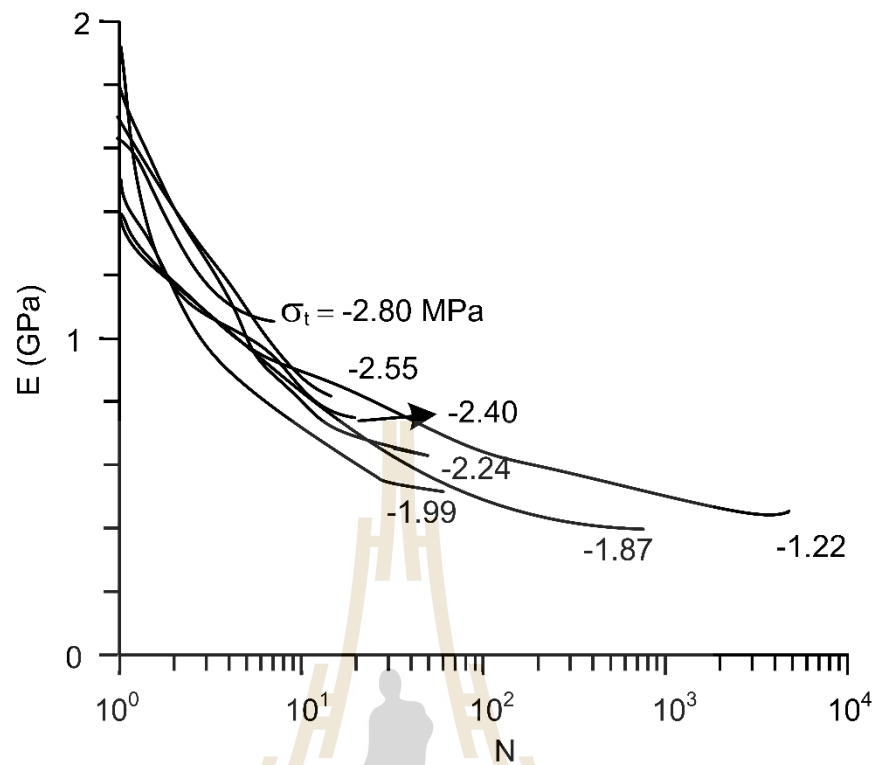


Figure 4.13 Elastic moduli (E) plotted as a function of number of loading cycles (N) up to failure for $f = 10$ mHz.

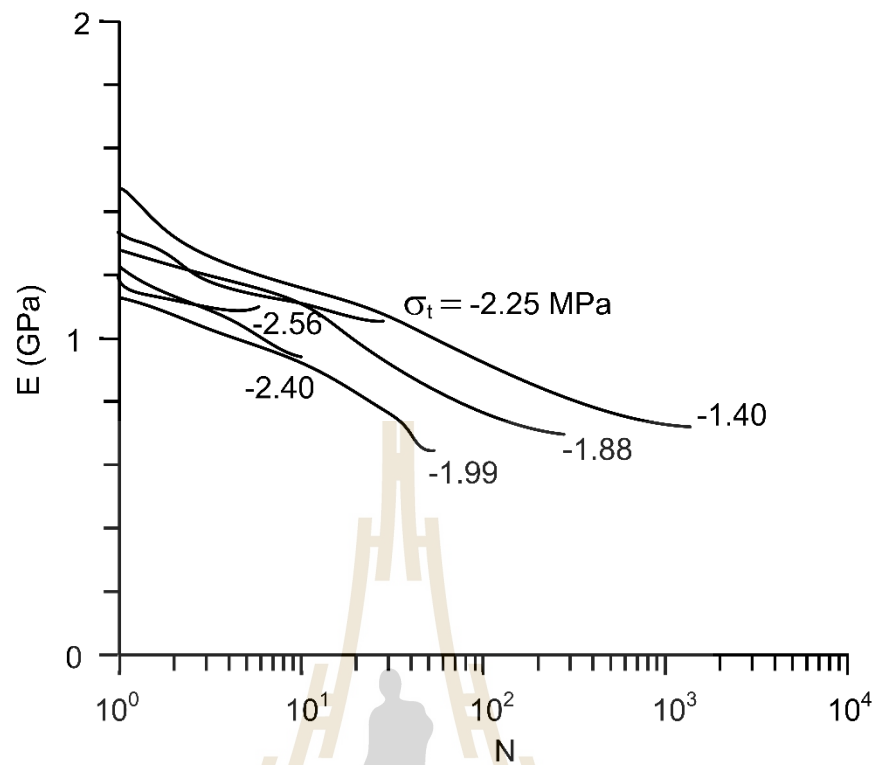


Figure 4.14 Elastic moduli (E) plotted as a function of number of loading cycles (N) up to failure for $f = 1$ mHz.

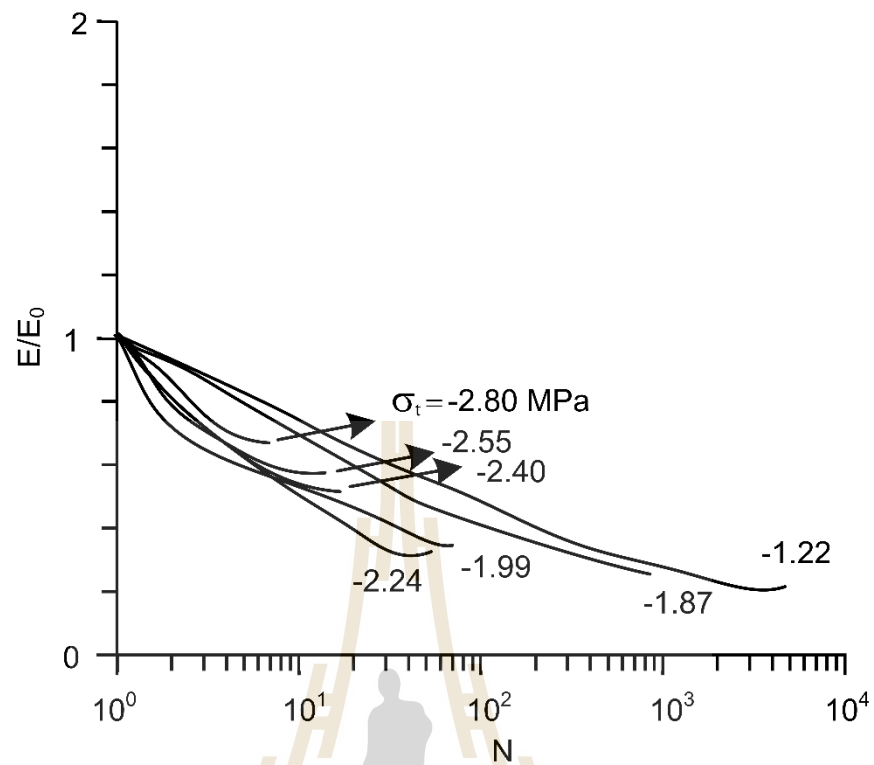


Figure 4.15 Normalized elastic moduli (E/E_0) plotted as a function of number of loading cycles (N) up to failure for $f = 10$ mHz.

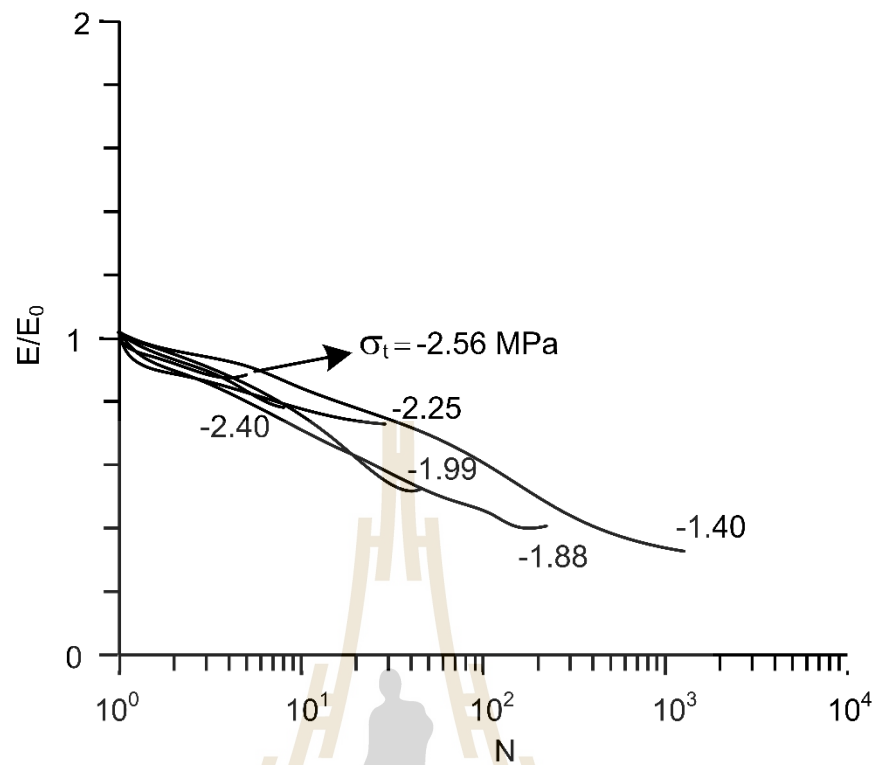


Figure 4.16 Normalized elastic moduli (E/E_0) plotted as a function of number of loading cycles (N) up to failure for $f = 1$ mHz.



4.5 Four point bending with constant loading rates test results

Figure 4.17 shows some post-test specimens of the Maha Sarakham salt obtained from the four-point bending testing under various loading rates. Table 4.2 summarizes the tensile strengths, tensile strains at failure, compressive strains at failure and deflections of four point bending test with constant loading rate test. Table A.3 in Appendix A show the applied load for this test. Post-failure observations show that there are two types of fracturing found in the rock salt specimens: cleavage fracturing (splitting of salt crystals at the cleavages) and inter-granular fracturing (Figure 4.18). The failure is induced within loading span. Figures 4.19 and 4.20 show the tensile and compressive stress-strain curves for loading rates of 4×10^{-7} to 4×10^{-3} MPa/s. Figure 4.21 shows deflections as a function of time. The higher deflection occurs under lower loading rate. Figure 4.22 shows tensile strains at failure as a function of deflection. The tensile strains increase with increasing deflection. Note that rate of deflections will rapidly increase before the failure occurs. The tensile and compressive elastic moduli for each specimen are determined from the tangent of the stress-strain curves at 40% failure stress. It is found that the deformation moduli increase with the loading rate. For all specimens the tensile elastic modulus is lower than the compressive elastic modulus. This agrees with the experimental obtained results by Jianhong et al. (2009). The test results indicate that the tensile strength increases with increasing loading rates, and tensile strains decreases with increasing loading rates also this agrees with the experimental observations by Wisetsaen et al. (2015), who conduct the ring tension test on the rock salt.

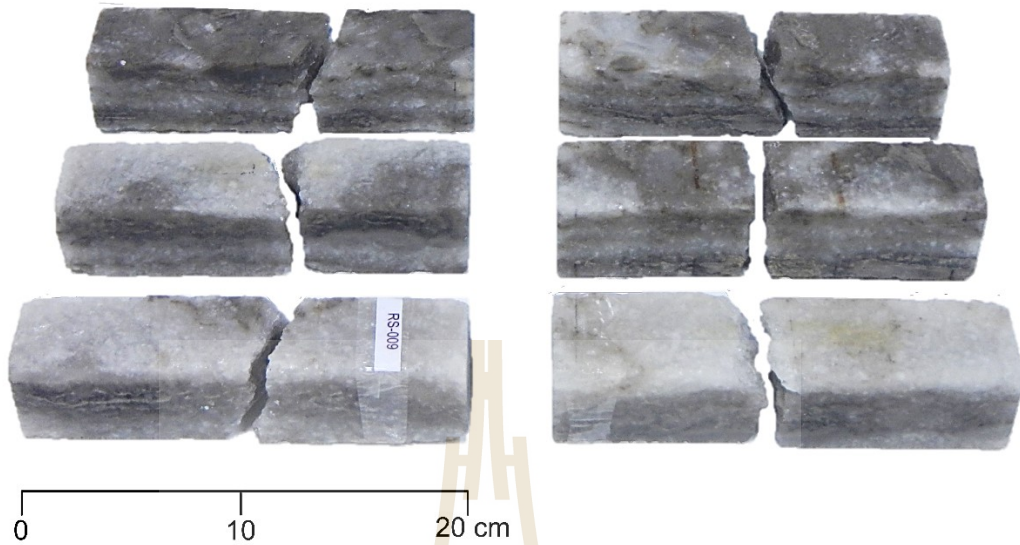


Figure 4.17 Some post-test specimens of Maha Sarakham salt obtained from four point bending testing under various loading rates.



Figure 4.18 Some cleavage fracturing and inter granular fracturing of salt specimens

Table 4.2 Stress, strain, deflection and elastic modulus for loading rates test.

| $\partial\sigma_T/\partial t$ (MPa/s) | σ_T (MPa) | ϵ_T (milli- strains) | ϵ_c (milli- strains) | Deflection (mm) | E_t (GPa) | E_c (GPa) |
|--|------------------|-------------------------------------|-------------------------------------|--------------------|----------------|----------------|
| 4×10^{-3} | 3.19 | 1.12 | -0.42 | 0.34 | 7.09 | 8.51 |
| 4×10^{-4} | 2.72 | 1.22 | -0.91 | 0.42 | 6.81 | 7.71 |
| | 2.21 | 1.42 | -1.08 | 0.44 | 4.02 | 4.23 |
| 4×10^{-5} | 1.53 | 1.80 | -1.20 | 0.45 | 2.78 | 2.91 |
| | 1.70 | 1.84 | -1.28 | 0.49 | 2.13 | 2.83 |
| 4×10^{-6} | 1.23 | 2.28 | -1.56 | 0.55 | 1.76 | 2.05 |
| 4×10^{-7} | 0.78 | 2.93 | -1.67 | 0.63 | 0.47 | 0.66 |

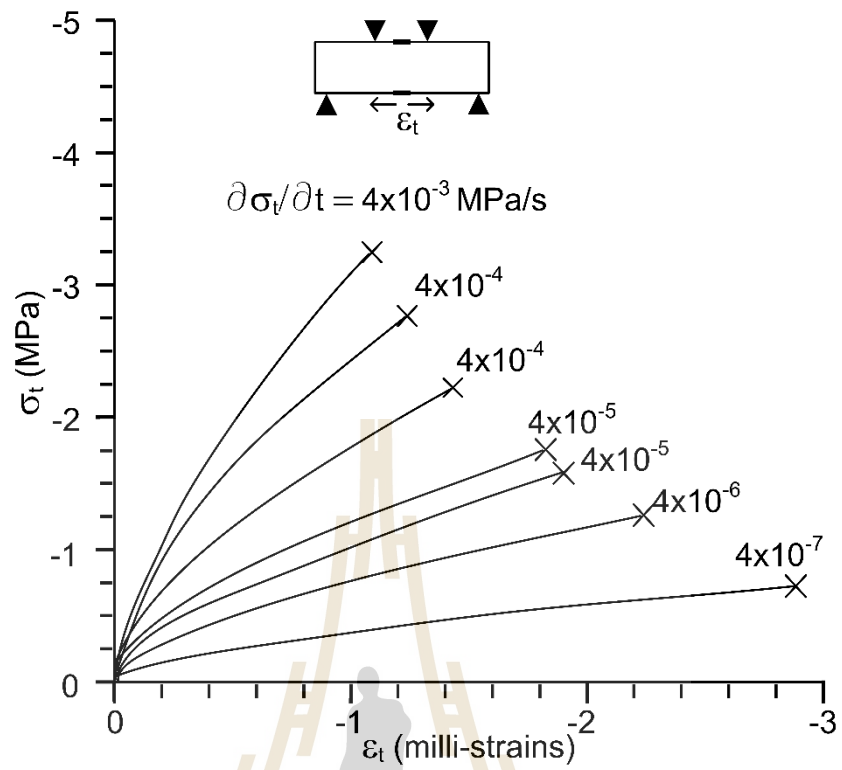


Figure 4.19 Tensile stress-strain curves for various loading rates.

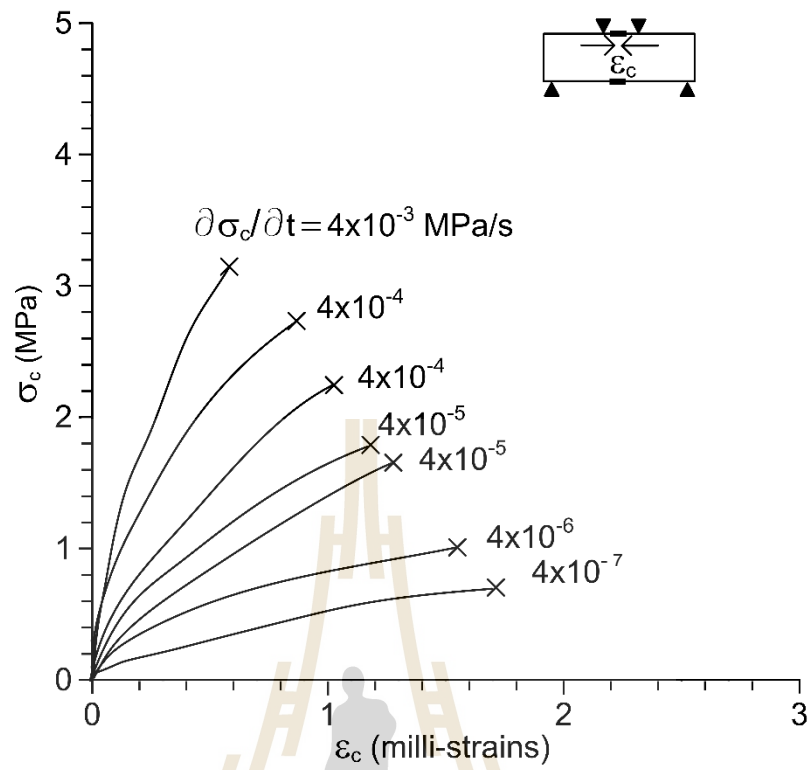


Figure 4.20 Compressive stress-strain curves for various loading rates.

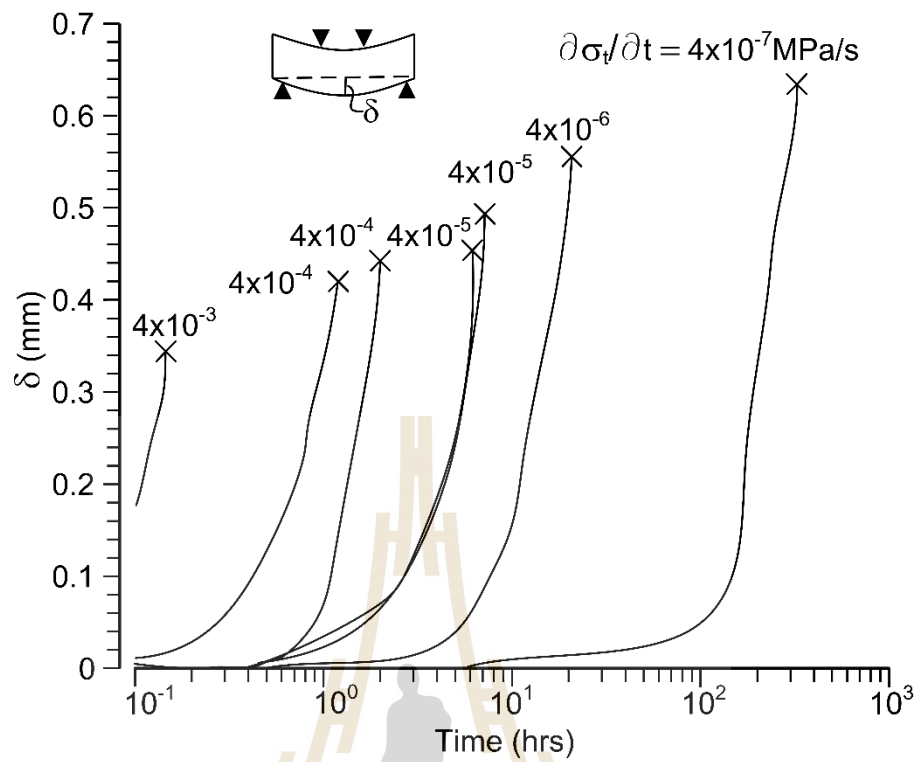


Figure 4.21 Deflection (δ) as a function of time (t) for loading rates under tensile stresses rates of 4×10^{-7} to 4×10^{-3} MPa.

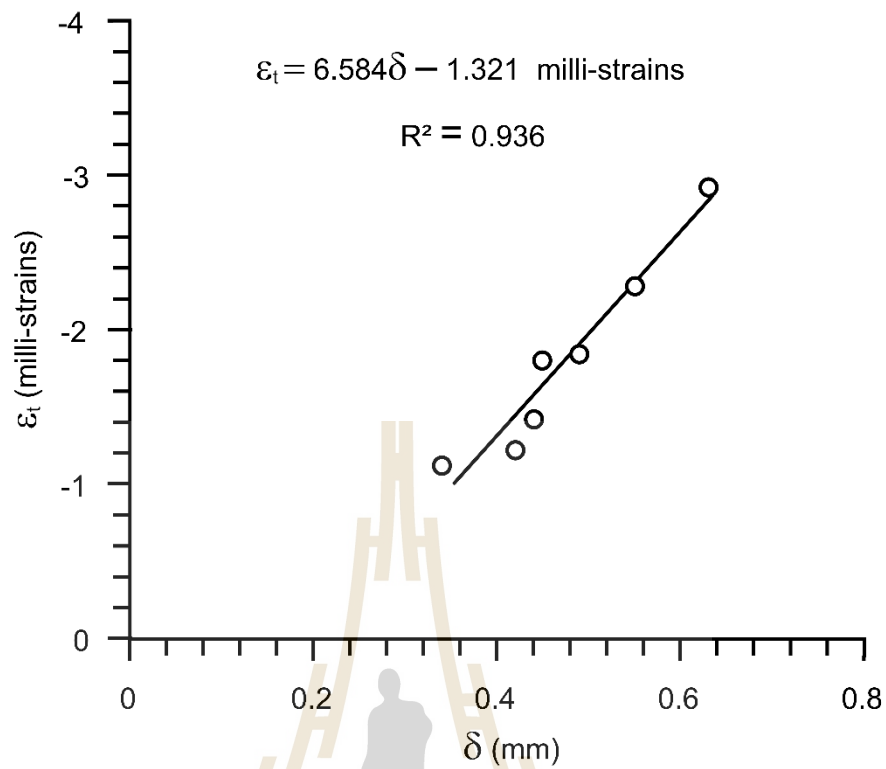


Figure 4.22 Tensile strain (ε_t) as a function of deflection (δ) for loading rates under tensile stresses rates of 4×10^{-7} to 4×10^{-3} MPa

CHAPTER V

SALT CREEP CALIBRATION AND STRENGTH CRITERION

5.1 Introduction

The purpose of this chapter is to describe the calibration results for the elastic and viscosity parameters. The regression analysis on the linear visco-elastic equation of the potential law is employed in the calibration. The data used in the calibrations are obtained from the four-point bending tests with creep loading and cyclic loading in chapter IV. Results from the laboratory measurements in terms of the tensile strength of rock salt under various loading frequencies and loading rates are also be used to formulate mathematical relations.

5.2 Potential Law

The tensile strains in previous chapter show the instantaneous and transient hgbhrdeformations which can be described by the potential law (Fuenkajorn and Daeman, 1988). The potential law is applied to describe salt behavior without considering the actual mechanism of deformation. Generally, empirical constitutive model is developed by linking the creep strain to stress time under isothermal condition. The potential law is power equation relating creep strain, stress and time. For this approach, the elastic strain (time-independent strain) is calculated by the classical elastic theory.

The total strain in salt can be divided into two parts, elastic strain (linear and recoverable strain) and plastic creep strain (time-dependent and nonrecoverable strain) (Senseny, 1983):

$$\varepsilon_t = \varepsilon_t^e + \varepsilon_t^c \quad (5.1)$$

where ε_t is axial strain, ε_t^e is elastic strain and ε_t^c is plastic creep strain. The elastic strain can be written as:

$$\varepsilon_t^e = \sigma_t / E \quad (5.2)$$

where ε_t^e is axial strain, σ_t is tensile stress and E is elastic modulus.

The plastic creep strain (ε_t^c) can be derived from the theory of plasticity based on the associated flow rule (Nair et al., 1974). The equivalent creep strain is directly obtained from one dimensional creep law which presents the plastic creep strain as a function of stress and time (Nair and Borese, 1970):

$$\varepsilon_t^c = \kappa \cdot \sigma_t^\beta \cdot t^\gamma \quad (5.3)$$

where κ , β and γ are material parameters. Substituting equations (5.1) and (5.2) into (5.3) we obtain the following:

$$\varepsilon_t = (\sigma_t / E) + \left[\kappa \cdot \sigma_t^\beta \cdot t^\gamma \right] \quad (5.4)$$

Regression analyses on the equation (5.4) using test data (σ , ϵ and t) with SPSS statistical software (Wendai, 2000) can determine the parameters κ , β and γ for each specimen. Table 5.1 summarizes the potential law parameters for all creep test and loading rates test. Figure 5.1 shows potential parameters as a function of tensile stress.

Table 5.1 Calibration of the potential parameters.

| Methods | σ_t (MPa) | Potential Parameters | | | | |
|--------------------|---------------------|----------------------|-------------------------|---------|----------|----------------|
| | | E (GPa) | κ (1/GPa·day) | β | γ | R ² |
| Creep | -1.25 | 3.02 | 0.33 | 1.02 | 0.32 | 0.943 |
| | -1.00 | 2.93 | 0.34 | 1.11 | 0.33 | 0.856 |
| | -0.75 | 4.01 | 0.23 | 1.13 | 0.36 | 0.938 |
| | -0.50 | 3.24 | 0.36 | 1.04 | 0.35 | 0.965 |
| Cyclic (10 mHz) | -2.80 | 4.32 | 0.01 | 0.41 | 0.66 | 0.843 |
| | -2.55 | 4.16 | 0.01 | 0.50 | 0.64 | 0.843 |
| | -2.40 | 4.18 | 0.01 | 0.43 | 0.63 | 0.865 |
| | -2.24 | 3.90 | 0.01 | 0.46 | 0.64 | 0.862 |
| | -1.99 | 4.36 | 0.01 | 0.43 | 0.64 | 0.912 |
| | -1.87 | 4.11 | 0.01 | 0.51 | 0.43 | 0.934 |
| | -1.22 | 4.20 | 0.01 | 0.50 | 0.36 | 0.956 |
| Cyclic (1 mHz) | -2.56 | 4.02 | 0.01 | 0.43 | 0.71 | 0.976 |
| | -2.40 | 4.27 | 0.01 | 0.46 | 0.72 | 0.834 |
| | -2.24 | 4.31 | 0.01 | 0.44 | 0.75 | 0.923 |
| | -1.99 | 4.17 | 0.01 | 0.46 | 0.53 | 0.812 |
| | -1.88 | 3.50 | 0.01 | 0.47 | 0.62 | 0.955 |
| | -1.40 | 3.61 | 0.01 | 0.37 | 0.64 | 0.976 |

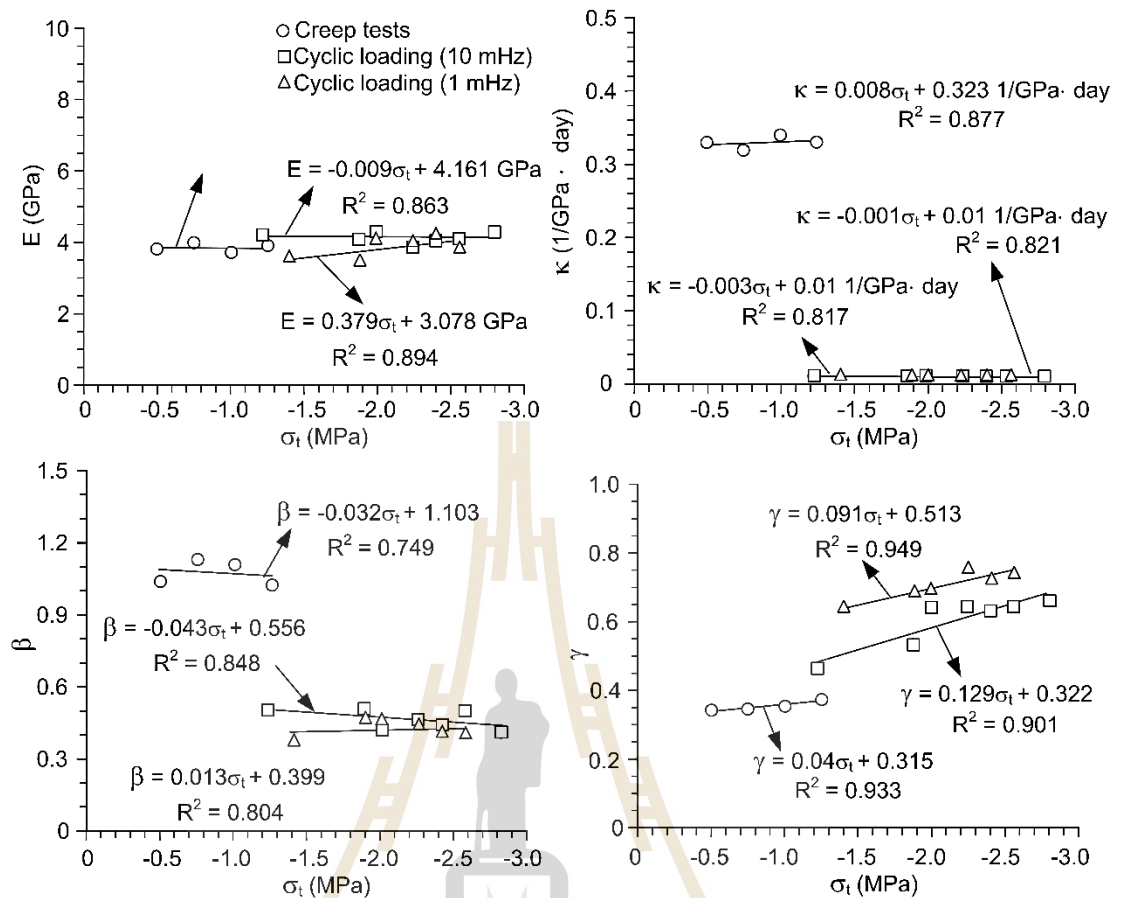


Figure 5.1 Potential parameters as a function of tensile stress.

The test results fit fairly well to potential law as suggested by the high values of the correlation coefficient (R^2). The parameter κ and β from creep test are higher than from cyclic loading test. The parameter γ from creep test is lower than from cyclic loading test.

5.3 Strength criterion

5.3.1 Tensile strength as a function of stress rate

The tensile strengths are plotted as a function of stress rates, as shown in Figure 5.2. The results indicate that the tensile strength linearly increases as the

stress rate increases. Good correlations are obtained ($R^2 > 0.9$). The strength reduction under different stress rates ($\partial\sigma_v/\partial t$) can be represented by a logarithm equation:

$$\sigma_T = \alpha \cdot \ln(\partial\sigma_v/\partial t) + \alpha' \quad (5.5)$$

where α and α' are empirical constants, equals to 0.265 and 4.501 MPa, respectively.

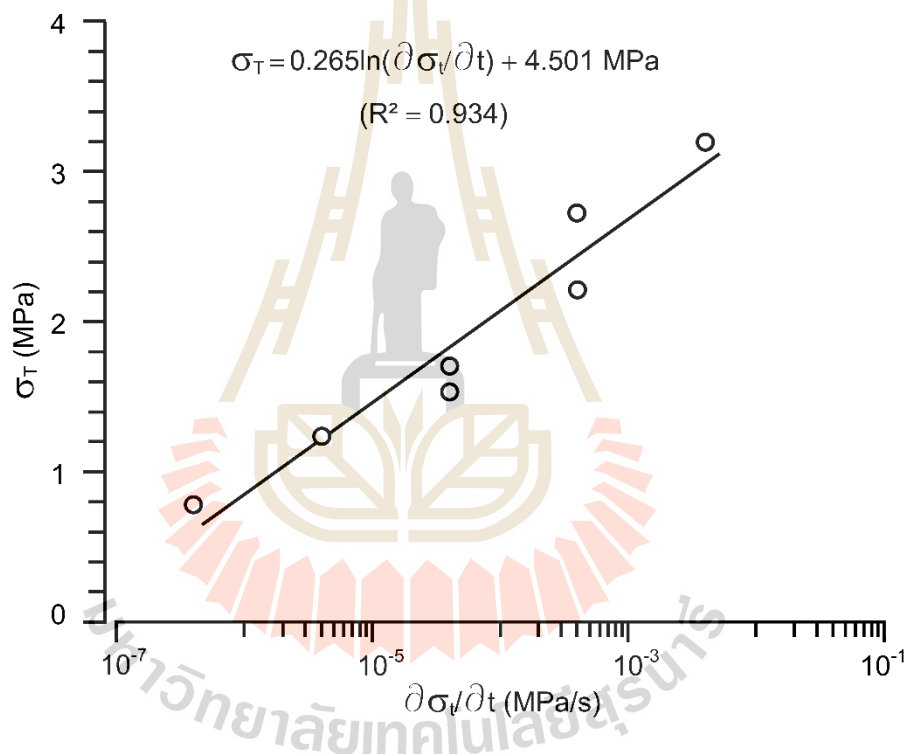


Figure 5.2 Tensile strengths (σ_T) as function of stress rate ($\partial\sigma_v/\partial t$).

5.3.2 Strain energy density criterion

The strain energy density principle is applied here to describe the salt strength and deformability under different loading rates, frequencies and amplitudes.

Assuming that the stress and strain obtained at the crack initiation point is in uniaxial

condition. For general (3D) loading, the distortional strain energy density can be calculated from the principal stress deviations and principal strain deviations for each salt specimen using the following relations (Jaeger et al., 2007):

$$W_d = (1/2) \cdot (s_1 e_1 + s_2 e_2 + s_3 e_3) \quad (5.6)$$

$$s_1 = \sigma_1 - s, \quad s_2 = \sigma_2 - s, \quad s_3 = \sigma_3 - s \quad (5.7)$$

$$e_1 = \varepsilon_1 - e, \quad e_2 = \varepsilon_2 - e, \quad e_3 = \varepsilon_3 - e \quad (5.8)$$

where s_1, s_2, s_3 and e_1, e_2, e_3 are the principle stress deviations and principle strain deviations at fatigue strengths. The relation under uniaxial condition; $\sigma_1 \neq 0, \sigma_2 = 0, \sigma_3 = 0, \varepsilon_1 \neq 0, \varepsilon_2 \neq 0$ and $\varepsilon_3 = 0$ as follows:

$$W_d = \sigma_1 \left\{ \left(\frac{\varepsilon_1}{3} \right) - \left(\frac{\varepsilon_2}{6} \right) \right\} \quad (5.9)$$

where ν is the Poisson's ratio equal to 0.36 (Artkhonghan, 2014)

$$\varepsilon_2 = -\nu \varepsilon_1$$

The distortional strain energy density can also be derived as a function of the mean strain energy as follows:

$$W_m = (3/2) \cdot s e \quad (5.10)$$

$$s = (1/3) \cdot (\sigma_1 + \sigma_2 + \sigma_3) \quad (5.11)$$

$$e = (1/3) \cdot (\varepsilon_1 + \varepsilon_2 + \varepsilon_3) \quad (5.12)$$

where s is the mean normal stress at dilation at fatigue strengths and e is the mean normal strain. The relation under uniaxial condition is as follows:

$$W_m = 1/6 \cdot \sigma_1 \cdot (\varepsilon_1 + \varepsilon_2) \quad (5.13)$$

Table 5.2 gives the strain energy density calculation. Figure 5.3 shows a linear trend of the test data in the $W_d - W_m$ relation which can be represented by:

$$W_d = \eta W_m \quad (5.14)$$

where η is empirical constant ($\eta = 3.478$).

This strain energy criterion explicitly incorporates the effects of loading rate, cyclic loading and frequencies, and hence can be used as a strength criterion for the roof of storage salt caverns.

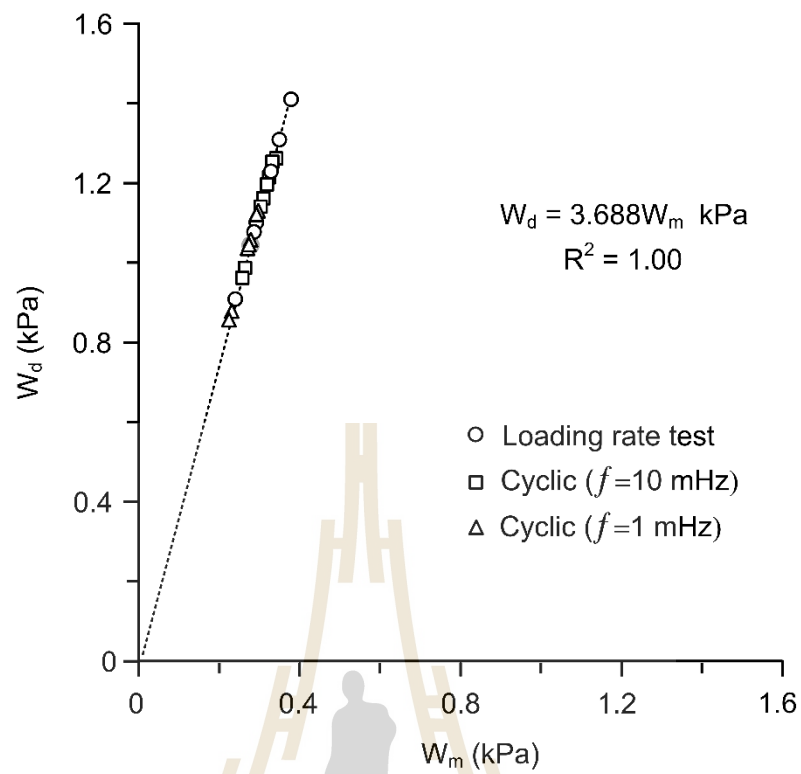


Figure 5.3 Strain energy of distortion (W_d) as a function of mean strain energy (W_m).

Table 5.2 Strain energy of each specimen.

| Loading rate test | | | | | | | | | |
|---------------------------------|--|---|---|-----------------------------------|-----------------------------------|-----------------------------------|--|--|--|
| Rate (MPa /s) | σ_1 (MPa) | ϵ_1 (10^{-3}) | ϵ_2 (10^{-3}) | s_1 (MPa) | s_2 (MPa) | s_3 (MPa) | e_1 (10^{-3}) | e_2 (10^{-3}) | e_3 (10^{-3}) |
| 4×10^{-3} | -3.19 | -1.12 | 0.40 | -2.13 | 1.06 | 1.06 | -0.88 | 0.64 | 0.24 |
| 4×10^{-4} | -2.72 | -1.22 | 0.44 | -1.81 | 0.91 | 0.91 | -0.96 | 0.70 | 0.26 |
| | -2.21 | -1.42 | 0.51 | -1.47 | 0.74 | 0.74 | -1.12 | 0.81 | 0.30 |
| 4×10^{-5} | -1.53 | -1.80 | 0.65 | -1.02 | 0.51 | 0.51 | -1.42 | 1.03 | 0.38 |
| | -1.70 | -1.84 | 0.66 | -1.13 | 0.57 | 0.57 | -1.45 | 1.05 | 0.39 |
| 4×10^{-6} | -1.23 | -2.28 | 0.82 | -0.82 | 0.41 | 0.41 | -1.79 | 1.31 | 0.49 |
| 4×10^{-7} | -0.78 | -2.93 | 1.05 | -0.52 | 0.26 | 0.26 | -2.30 | 1.68 | 0.63 |
| Cyclic loading test | | | | | | | | | |
| f (mHz) | σ_1 (MPa) | ϵ_1 (10^{-3}) | ϵ_2 (10^{-3}) | s_1 (MPa) | s_2 (MPa) | s_3 (MPa) | e_1 (10^{-3}) | e_2 (10^{-3}) | e_3 (10^{-3}) |
| 10 | -3.20 | -0.78 | 0.28 | -2.13 | 1.07 | 1.07 | -0.61 | 0.45 | 0.16 |
| | -2.80 | -1.09 | 0.39 | -1.87 | 0.93 | 0.93 | -0.86 | 0.62 | 0.23 |
| | -2.55 | -1.25 | 0.45 | -1.70 | 0.85 | 0.85 | -0.98 | 0.72 | 0.27 |
| | -2.40 | -1.32 | 0.48 | -1.60 | 0.80 | 0.80 | -1.04 | 0.76 | 0.28 |
| | -2.24 | -1.38 | 0.50 | -1.49 | 0.75 | 0.75 | -1.09 | 0.79 | 0.29 |
| | -1.99 | -1.46 | 0.53 | -1.33 | 0.66 | 0.66 | -1.15 | 0.84 | 0.31 |
| | -1.87 | -1.58 | 0.57 | -1.25 | 0.62 | 0.62 | -1.24 | 0.91 | 0.34 |
| | -1.22 | -1.99 | 0.72 | -0.81 | 0.41 | 0.41 | -1.56 | 1.14 | 0.43 |
| 1 | -2.90 | -0.76 | 0.27 | -1.93 | 0.97 | 0.97 | -1.54 | 0.44 | 0.17 |
| | -2.56 | -1.03 | 0.37 | -1.71 | 0.85 | 0.85 | -0.60 | 0.59 | 0.22 |
| | -2.40 | -1.10 | 0.40 | -1.60 | 0.80 | 0.80 | -0.81 | 0.63 | 0.23 |
| | -2.25 | -1.19 | 0.43 | -1.50 | 0.75 | 0.75 | -0.87 | 0.68 | 0.25 |
| | -1.99 | -1.33 | 0.48 | -1.33 | 0.66 | 0.66 | -0.94 | 0.76 | 0.28 |
| | -1.88 | -1.53 | 0.55 | -1.25 | 0.63 | 0.63 | -1.05 | 0.88 | 0.33 |
| | -1.40 | -1.54 | 0.55 | -0.93 | 0.47 | 0.47 | -1.20 | 0.88 | 0.33 |

Table 5.2 Strain energy of each specimen. (cont.)

| Loading rate test | | | | | | | |
|----------------------------|--|---|---|--------------------|-------------------------------------|---------------------|---------------------|
| Rate (MPa/s) | σ_1 (MPa) | ϵ_1 (10^{-3}) | ϵ_2 (10^{-3}) | s (MPa) | e (10^{-3}) | Wd (kPa) | Wm (kPa) |
| 4×10^{-3} | -3.19 | -1.12 | 0.40 | -2.13 | 1.06 | 0.64 | 0.24 |
| 4×10^{-4} | -2.72 | -1.22 | 0.44 | -1.81 | 0.91 | 0.70 | 0.26 |
| | -2.21 | -1.42 | 0.51 | -1.47 | 0.74 | 0.81 | 0.30 |
| 4×10^{-5} | -1.53 | -1.80 | 0.65 | -1.02 | 0.51 | 1.03 | 0.38 |
| | -1.70 | -1.84 | 0.66 | -1.13 | 0.57 | 1.05 | 0.39 |
| 4×10^{-6} | -1.23 | -2.28 | 0.82 | -0.82 | 0.41 | 1.31 | 0.49 |
| 4×10^{-7} | -0.78 | -2.93 | 1.05 | -0.52 | 0.26 | 1.68 | 0.63 |
| Cyclic loading test | | | | | | | |
| f (mHz) | σ_1 (MPa) | ϵ_1 (10^{-3}) | ϵ_2 (10^{-3}) | s (MPa) | e (10^{-3}) | Wd (kPa) | Wm (kPa) |
| 10 | -3.20 | -0.78 | 0.28 | -1.07 | -0.17 | 0.98 | 0.27 |
| | -2.80 | -1.09 | 0.39 | -0.93 | -0.23 | 1.20 | 0.33 |
| | -2.55 | -1.25 | 0.45 | -0.85 | -0.27 | 1.25 | 0.34 |
| | -2.40 | -1.32 | 0.48 | -0.80 | -0.28 | 1.25 | 0.34 |
| | -2.24 | -1.38 | 0.50 | -0.75 | -0.29 | 1.22 | 0.33 |
| | -1.99 | -1.46 | 0.53 | -0.66 | -0.31 | 1.14 | 0.31 |
| | -1.87 | -1.58 | 0.57 | -0.62 | -0.33 | 1.16 | 0.32 |
| | -1.22 | -1.99 | 0.72 | -0.41 | -0.42 | 0.95 | 0.26 |
| 1 | -2.90 | -0.76 | 0.27 | -0.97 | -0.16 | 0.86 | 0.24 |
| | -2.56 | -1.03 | 0.37 | -0.85 | -0.22 | 1.04 | 0.28 |
| | -2.40 | -1.10 | 0.40 | -0.80 | -0.24 | 1.04 | 0.28 |
| | -2.25 | -1.19 | 0.43 | -0.75 | -0.25 | 1.05 | 0.29 |
| | -1.99 | -1.33 | 0.48 | -0.66 | -0.28 | 1.04 | 0.28 |
| | -1.88 | -1.53 | 0.55 | -0.63 | -0.33 | 1.13 | 0.31 |
| | -1.40 | -1.54 | 0.55 | -0.47 | -0.33 | 0.85 | 0.23 |

CHAPTER VI

NUMERICAL MODELLING

6.1 Introduction

This chapter describes the method and results of finite difference analysis by using FLAC (Itasca, 1992) to simulate tensile stresses induced the mine roof in rock salt during compressed-air storage operation. The simulations calculate tensile stresses in mine roof under different storage pressures, depths and room widths. The stress results can be used to predict maximum storage cycles at failure from S-N curve presented in the previous chapter.

6.2 Numerical modelling (FLAC program)

The finite difference code FLAC 4.0 is used in the simulations of the compressed-air energy storage (Crotagino et al., 2001) operation in room and pillar mine openings under plane strain condition. The rock sequences at Bamnet Narong district, Chaiyaphum province are used in the simulations. The storage models are subjected to minimum pressures from 20%, 30%, 40% and 50% of the in-situ stress at the roof, with room widths from 10, 15 to 20 m. The pillar widths and room height are 30 and 15 m, respectively. The simulations determine the maximum tensile stresses in mine roof to predict maximum storage cycles at failure. The roof thickness is defined as 40% of the room width to comply with the local regulations. The opening depths are 175, 250 and 300 m. The overburden and underlying rocks are

inter-bedded of the rock salt group: Phutok Formation, Upper Salt, Middle Clastic, Middle Salt, Lower Clastic and Lower Salt members. The bottom boundary is fixed in the y-axis. The top boundary can move freely in both directions. The finite difference mesh for the simulation as shown in Figures 6.1 to 6.3.

6.3 Property parameters used in numerical modelling

Table 6.1 shows the overburden property parameters used for numerical modeling. The stresses in rock salt used in the computer modelling are assumed to be hydrostatic which depends on depth and density of rock layers. Therefore, the vertical stress at any depth can be calculated from the density in the model. All rock sequences are assumed to behave as the Mohr-Coulomb material.

Table 6.1 Material parameters used for numerical modeling

| Properties | Rock types | | | | | |
|---|-------------------------|----------------------|-------------------------|--|-------------------------|-----------------------------------|
| | Upper Clastics | Upper Salt | Middle Clastics | Middle Salt | Lower Clastic | Lower Salt |
| K (GPa) | 2.52 | 13.90 | 0.65 | 13.90 | 0.54 | 12.00 |
| G (GPa) | 1.44 | 10.40 | 0.27 | 10.40 | 0.25 | 6.66 |
| ρ (g/cm³) | 2.49 | 2.89 | 2.15 | 2.14 | 2.18 | 2.16 |
| c (MPa) | 3.50 | 5.00 | 0.56 | 6.00 | 0.38 | 4.82 |
| ϕ (°) | 25.00 | 49.70 | 23.00 | 51.60 | 5.00 | 45.00 |
| σ_t (MPa) | 1.00 | 1.88 | 0.83 | 1.88 | 0.83 | 1.88 |
| References | GMR report (2010) | Whetchasat (2002) | GMR report (2010) | Sriapai et al. (2012) and Luangthip et al. (2016) | GMR report (2010) | Luang thip et al. (2016) |

6.4 Numerical results

The minimum pressures of 20%, 30%, 40% and 50% of in-situ stress are determined in the middle of the roof (point A in Figures 6.1 to 6.3). The number of pressure cycles are calculated from S-N curve in previous chapter. Figure 6.4 shows the minimum pressures as function of number of cycles under different depths and room widths. The tensile stresses increase with depths and room widths under the same depth. The tensile stresses decrease with increasing minimum pressures. Examples of tensile stress at 300 m depth, minimum pressure at 20% of in-situ stress and 10, 15, 20 m room widths are given in Table 6.2. The results indicate that the maximum tensile stress are equal to 2.09, 2.35 and 2.71 MPa, respectively.

The distribution of the tensile stresses and compressive stresses in mine roof are illustrated in Figures A.1 to A.36 in Appendix A. The tensile stress concentrates at the center of the roof. The maximum compressive stress are concentrated at the top of roof.

The S-N curve can help defining the operational life (pressure cycles) of salt roof, as shown in Figures 6.4 to 6.6. The calculations also depend on the minimum storage pressures. The models 13D250Wo10 and 16D250Wo10 show the maximum number of cycles equal to 419 and 2751, respectively.

6.5 Discussions

The effect of frequency should be considered on the cyclic loading tested as it may play a significant role on salt around storage room (Phueakphum, 2003). The number of pressure cycles, which are calculated from S-N curve ($f=1$ mHz) may not be conservative because gas storage operation has much lower frequency during actual

operation. However it is a preliminary prediction. The actual conditions may take into account a variety of factors, such as structural geology, depth, thickness of roof and overburden.



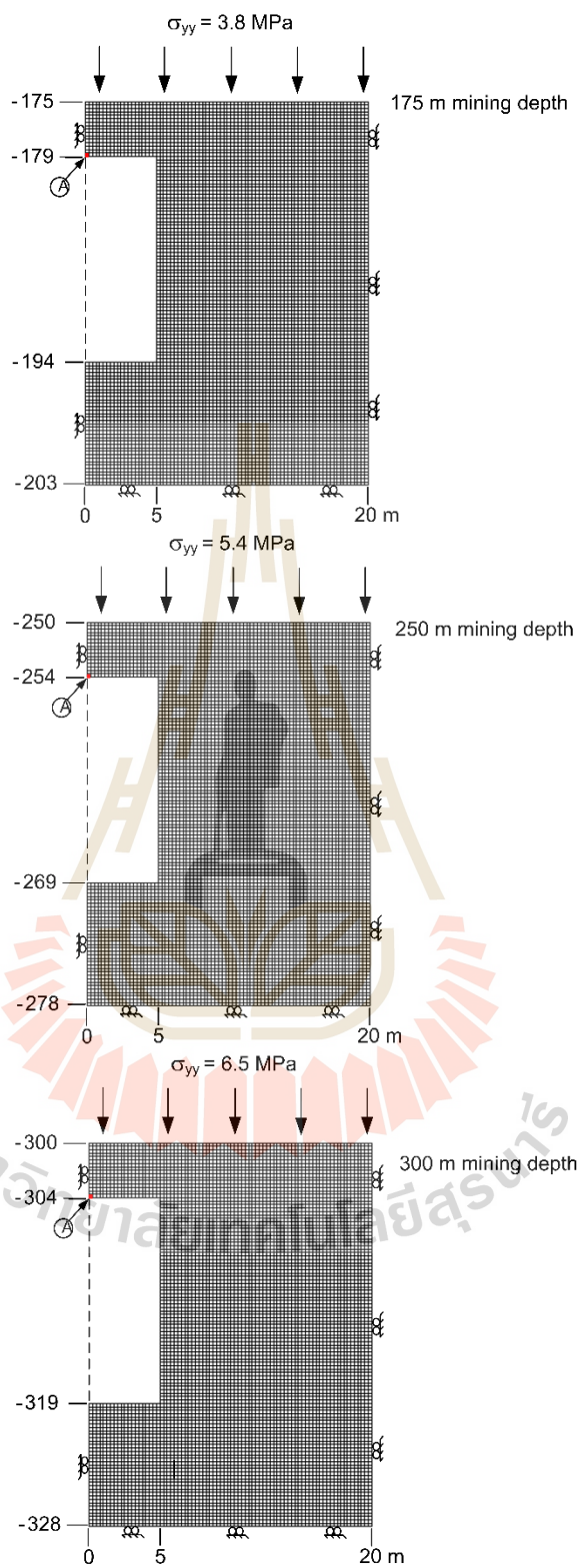


Figure 6.1 Finite difference mesh developed for FLAC simulation, mining depths are 175, 250 and 300 m and room width is 10 m.

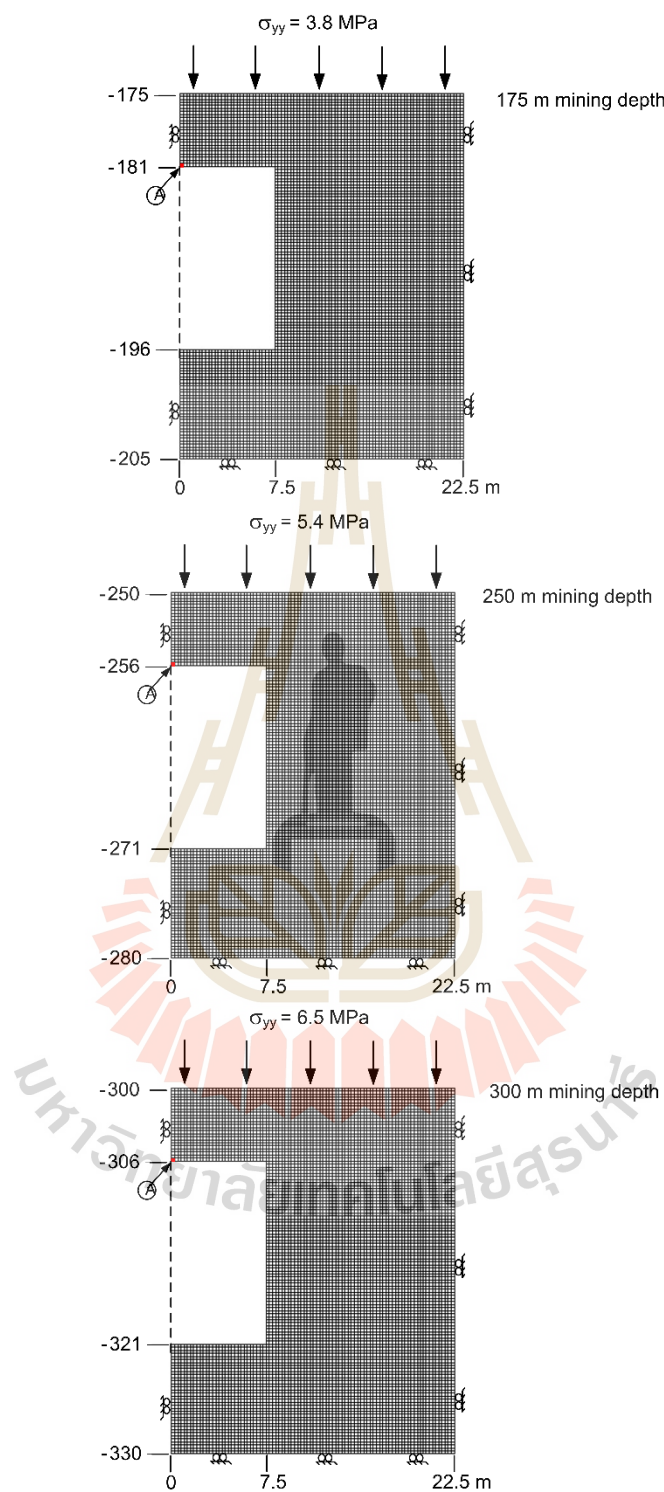


Figure 6.2 Finite difference mesh developed for FLAC simulation, mining depths are 175, 250 and 300 m and room width is 15 m.

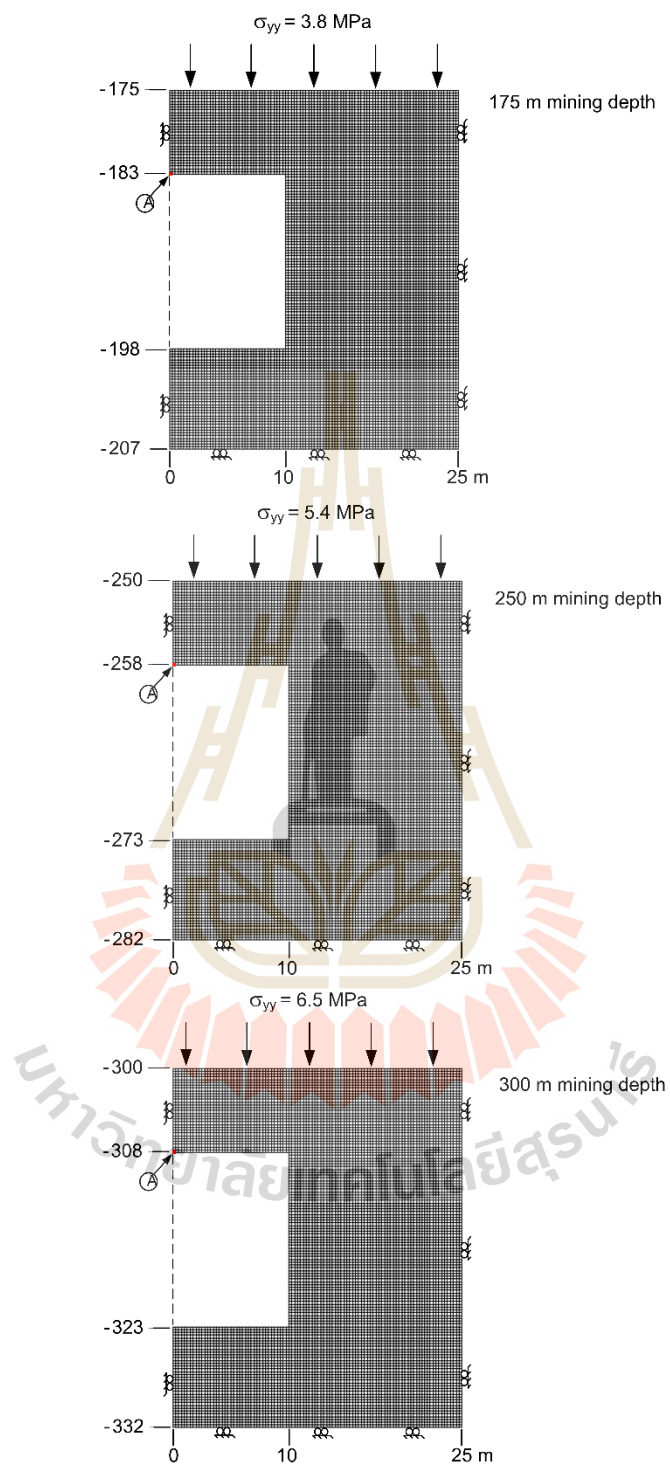


Figure 6.3 Finite difference mesh developed for FLAC simulation, mining depths are 175, 250 and 300 m and room width is 20 m.

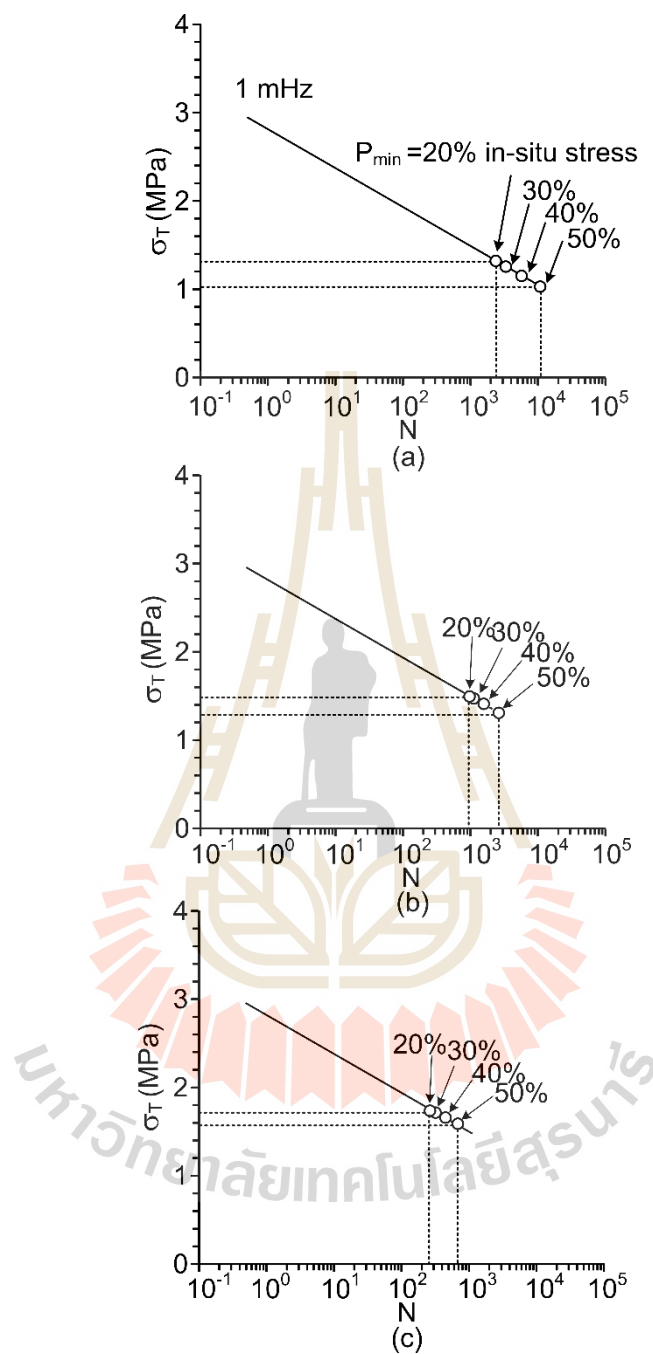


Figure 6.4 Fatigue tensile stresses as a function of cycle at 175 m with 10 m (a), 15 m (b) and 20 m (c) room widths.

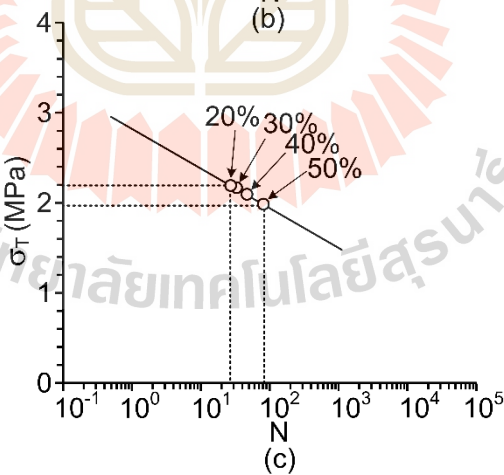
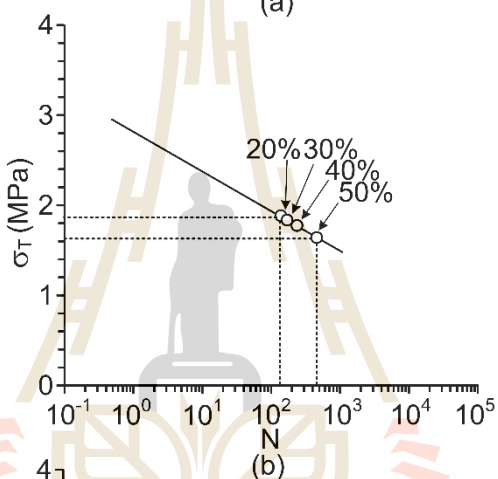
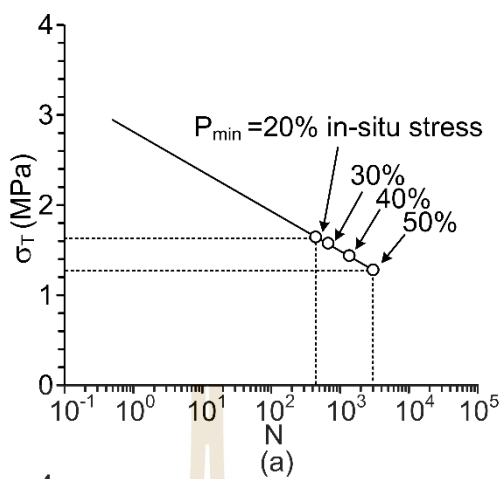


Figure 6.5 Fatigue tensile stresses as a function of cycle at 250 m with 10 m (a), 15 m (b) and 20 m (c) room widths.

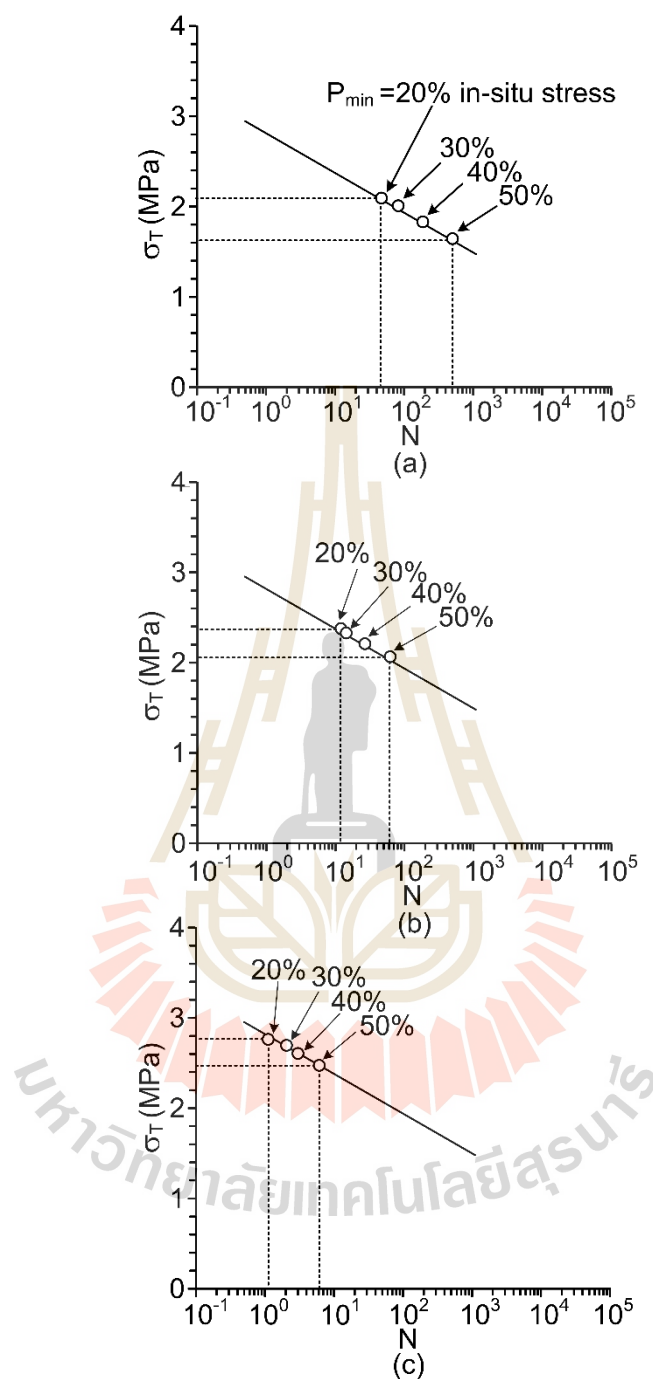


Figure 6.6 Fatigue tensile stresses as a function of cycle at 300 m with 10 m (a), 15 m (b) and 20 m (c) room widths.

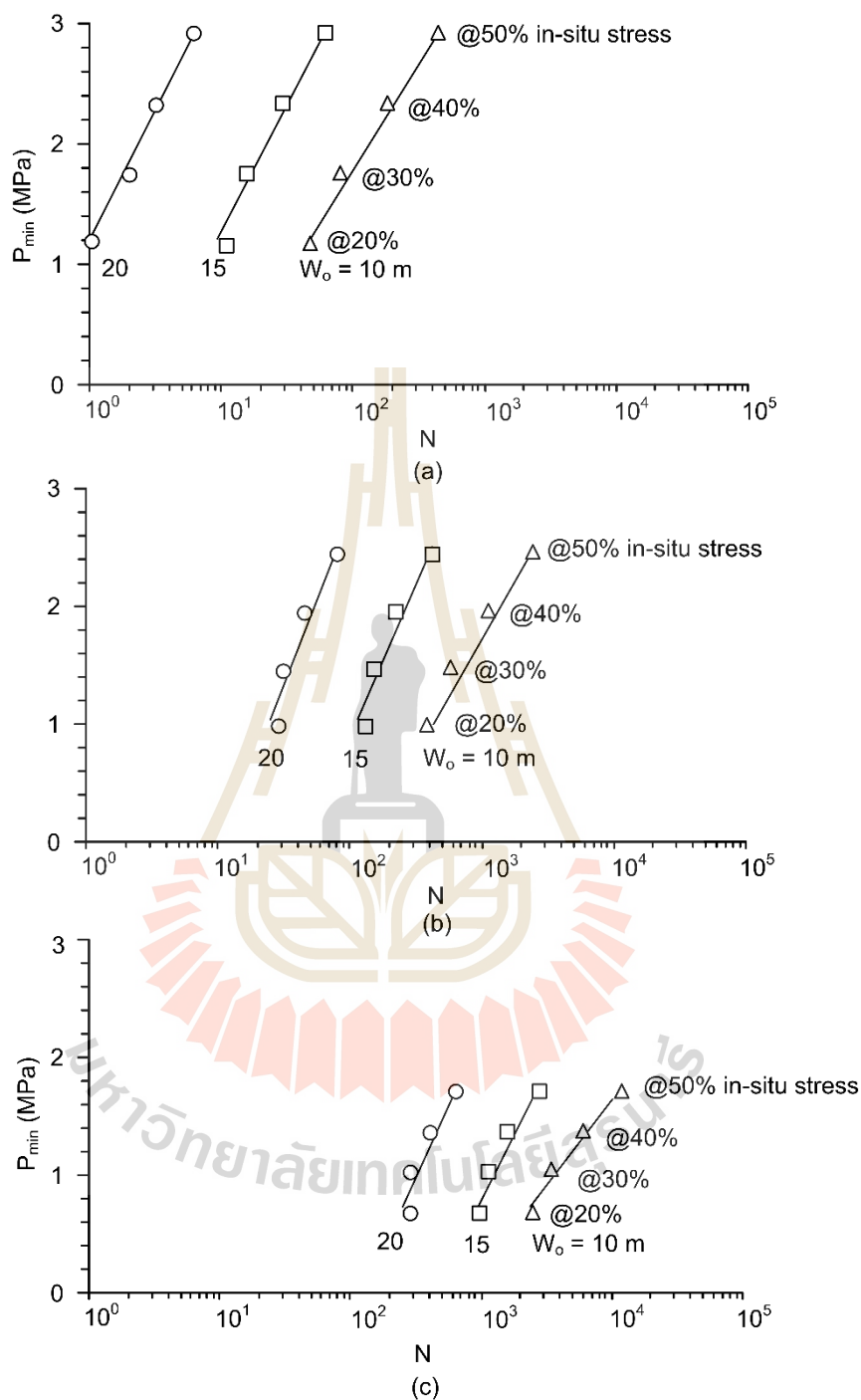


Figure 6.7 Minimum pressures as a function of cycles various mining depths (300 m (a), 250 m (b) and 175 m (c)).

Table 6.2 Minimum pressures, induced tensile stresses and maximum number of loading cycles.

| Model No. | P _{min} | | σ _t (MPa) | N |
|-------------------------|------------------|-------|-------------------------|-------|
| | (%) | (MPa) | | |
| 1D175W _o 10 | 20 | 0.68 | -1.33 | 2416 |
| 2D175W _o 10 | 30 | 1.03 | -1.27 | 3361 |
| 3D175W _o 10 | 40 | 1.37 | -1.17 | 5767 |
| 4D175W _o 10 | 50 | 1.71 | -1.04 | 10938 |
| 5D175W _o 15 | 20 | 0.68 | -1.50 | 1012 |
| 6D175W _o 15 | 30 | 1.03 | -1.47 | 1152 |
| 7D175W _o 15 | 40 | 1.37 | -1.42 | 1571 |
| 8D175W _o 15 | 50 | 1.71 | -1.31 | 2670 |
| 9D175W _o 20 | 20 | 0.68 | -1.73 | 304 |
| 10D175W _o 20 | 30 | 1.03 | -1.72 | 323 |
| 11D175W _o 20 | 40 | 1.37 | -1.66 | 437 |
| 12D175W _o 20 | 50 | 1.71 | -1.58 | 671 |
| 13D250W _o 10 | 20 | 0.97 | -1.67 | 419 |
| 14D250W _o 10 | 30 | 1.46 | -1.59 | 639 |
| 15D250W _o 10 | 40 | 1.94 | -1.46 | 1248 |
| 16D250W _o 10 | 50 | 2.43 | -1.31 | 2751 |
| 17D250W _o 15 | 20 | 0.97 | -1.88 | 141 |
| 18D250W _o 15 | 30 | 1.46 | -1.84 | 167 |
| 19D250W _o 15 | 40 | 1.94 | -1.77 | 242 |
| 20D250W _o 15 | 50 | 2.43 | -1.64 | 473 |
| 21D300W _o 10 | 20 | 0.97 | -2.16 | 31 |
| 22D300W _o 10 | 30 | 1.46 | -2.15 | 34 |
| 23D300W _o 10 | 40 | 1.94 | -2.08 | 49 |

Table 6.2 Minimum pressures, induced tensile stresses and maximum number of loading cycles (continued).

| Model No. | P_{min} | | σ_t (MPa) | N |
|-------------------------|-----------|-------|---------------------|-----|
| | (%) | (MPa) | | |
| 24D300W _o 10 | 50 | 2.43 | -1.97 | 85 |
| 25D300W _o 15 | 20 | 1.16 | -2.09 | 47 |
| 26D300W _o 15 | 30 | 1.74 | -1.99 | 79 |
| 27D300W _o 15 | 40 | 2.32 | -1.83 | 183 |
| 28D300W _o 15 | 50 | 2.90 | -1.64 | 497 |
| 29D300W _o 15 | 20 | 1.16 | -2.35 | 14 |
| 30D300W _o 15 | 30 | 1.74 | -2.31 | 15 |
| 31D300W _o 15 | 40 | 2.32 | -2.22 | 29 |
| 32D300W _o 15 | 50 | 2.90 | -2.06 | 66 |
| 33D300W _o 15 | 20 | 1.16 | -2.71 | 1 |
| 34D300W _o 15 | 30 | 1.74 | -2.69 | 2 |
| 35D300W _o 15 | 40 | 2.32 | -2.60 | 3 |
| 36D300W _o 15 | 50 | 2.90 | -2.47 | 6 |

CHAPTER VII

DISCUSSIONS, CONCLUSIONS AND RECOMMENDATIONS FOR FUTURE STUDIES

7.1 Discussions

This section discusses the key issues relevant to the reliability of the test schemes and the adequacies of the test results. Comparisons of the results and findings from this study with those obtained elsewhere under similar test conditions have also been made.

The tensile strength of salt can be obtained in the laboratory by various methods, including direct tension tests, Brazilian tension tests, ring tension tests, flexural tests, three- and four-point bending tests (Phueakphum et al., 2013; Wisetsaen et al., 2015; Forster, 1967 and Sen, 1961). The four-point bending test is more preferable than the others because it is the simplest method and subject to the stress configurations similar to those in the mine roof. The beam bending test under uniform load is very different to perform.

The post-test specimens obtained from the four-point bending test show that the tension crack occur at the center of specimen for all testing. This suggests that the test results are valid.

Most of the relevant literatures concentrate on the time-dependent on compressive strength of rock salt (Fuenkajorn and Daemen, 1988; Dusseault and Fordham, 1993; Jeremic, 1994; Knowles et al., 1998). Creep deformation occurs in

three different phases (instantaneous, steady state and transient). The tensile strains under static loading show the instantaneous and transient deformations creep phases of rock specimen which can be described by the potential creep law, as suggested by the good values of the correlation coefficient. The results from the four-point bending creep test show some variation which may be due to an inclusion (anhydrite and clay minerals) in salt specimens, as evidenced by the density variation among the specimens (density of pure halite is 2.16 g/cc).

The loading rate tests are performed under five stress rates from 1×10^{-7} to 1×10^{-3} MPa/s at the crack initiation point. The test results in terms of the tensile strength and loading rate is agree reasonably well with the related test results on the Maha Sarakham salt obtained by Wisetsaen et al. (2015) and Chobsranoi et al. (2016) that the tensile strengths of rock increase with the loading rate.

The cyclic loading tests have two frequencies: 1 and 10 mHz. The number of loading cycles increase with decreasing the maximum applied stresses (amplitudes). This agrees with those obtained by Voznesenskii et al. (2017). From the S-N curves, as shown in Figure 4.12, the effect of loading frequency is relatively small. The strength difference between 1 mHz and 10 mHz is about to 10%. The salt elasticity decreases as the number of loading cycles increases, as illustrated in Figures 4.13 to 4.14. It is probably because the microcracks occur in the salt specimen for each cycle, causing salt strength and elasticity decrease.

The specimens size used in this study are relatively small. Recognizing the size effects on the rock strengths (Jaeger et al., 2007), larger specimens should be used in summary the strengths obtained here under all test schemes would overestimate the strength of the salt under in-situ condition due to the scale effect.

7.2 Conclusions

All objectives and requirements of this study have been met. The results of the laboratory testing and analyses can be concluded as follows:

The constant loading tests indicate that the tensile stresses of salt and the tensile creep strains are higher than the compressive creep strains. Larger creep strains are obtained for the specimens with higher tensile stress and the deflection increases with increasing tensile stresses.

The effect of and loading rate on the rock tensile strength is assessed under five constant rates from 1×10^{-7} to 1×10^{-3} MPa/s. The results show that the tensile strength increases with increasing loading rates, and tensile strains decreases with increasing loading rates. The tensile elastic modulus is lower than the compressive elastic modulus. The higher deflection occurs under lower loading rate.

Results from cyclic loading tests indicate that the permanent strain increase and accumulates from each cycle until the specimen fails. The number of loading cycles increases with decreasing the maximum applied stresses (amplitudes). The number of cycles that causes failure are function of differential fatigue tensile strength and frequency. Relation between the number of cycles (N) and fatigue tensile strength (S) can be drawn as: $S = -0.209 \ln(N) + 3.071$ MPa (for 10 mHz) and $S = -0.191 \ln(N) + 2.826$ MPa (for 1 mHz). Elastic modulus of rock salt derived from the cyclic loading test results decrease as the number of cycles increase. The elastic moduli obtained from the test are varied from 0.47 GPa to 1.93 GPa.

The strength results are used to develop a strength criterion in form of the strain energy density. Obtaining the specimen strengths under a wide range of loading rates

from constant loading rates test, loading frequencies, and loading amplitudes would allow a rigorous calibration of the strain energy equation.

Numerical simulations of the mine roof under different storage pressures, depths and room widths provide the maximum tensile stress in the middle of the salt roof. The simulation indicate that the tensile stresses increase with depths and room widths while under the same depth and width decrease with increasing minimum pressures. The maximum deflection occurs at 300 m depth, 20 m room width and 20% minimum storage pressure.

7.3 Recommendations for future studies

1) The test specimens here are relatively small. Testing on larger specimens is desirable to confirm the research findings. Verification of the four-point bending test proposed concept should be tested under a wider range of salt from other sources.

2) This research can be considered as a preliminary study. For detailed study, more laboratory tests should be performed by emphasizing on the effects of changing in stress levels and temperatures.

3) Rate of air compressing and releasing from rock salt storage should be further studied because it is expected that these rates will affect the mechanical behavior and of rock salt around the storage.

4) The simulations to calculate tensile stresses in mine roof by used to FLAC software. It is a preliminary prediction only because the actual conditions may take into account a variety of factors, such as structural geology, depth, thickness of roof and overburden.

REFERENCES

- Artkhonghan, K. (2014). Effects of stress path on triaxial strength and elasticity of maha sarakham salt. **Doctor's Thesis**. Suranaree University of Technology.
- ASTM C293-02. Standard test method for flexural strength of concrete (Using simple beam with center-point loading). **Annual Book of ASTM Standards**, Vol. 04.08. West Conshohocken: American Society for Testing and Materials.
- ASTM D6272-10. Standard test method for flexural properties of unreinforced and reinforced plastics and electrical insulating materials by four-point bending. **Annual Book of ASTM Standards**, Vol. 04.08. Philadelphia: American Society for Testing and Materials.
- Bauer, S.J., Ehgartner, Levin, B.L., and Linn, J.K. (1998). Waste disposal in horizontal solution mined caverns-considerations of site location, cavern stability, and development considerations. In **Proceedings of SMRI Fall Meeting**. Rome, Italy.
- Berenbaum, R. and Brodie, I. (1959). The tensile strength of coal. **Journal of the Institute of Fuel**. 32: 320-327.
- Chobsranoi, M. and Fuenkajorn, K. (2016). Maximum unsupported span and standup time of potash mine roof as affected by carnallite contents. In **the 9th Asian Rock Mechanics Symposium**. 18-20 October 2016, Bali, Indonesia.
- Crotogino, F., Mohmeyer, K.U., and Scharf, R. (2001). Huntorf CAES: More than 20 years of successful operation. In **Proceedings of the Solution Mining Research Institute (SMRI)** (pp. 351-357). Spring Meeting, Orlando, FL, USA,

- 15-18 April, 2001. Solution Mining Research Institute (SMRI), Clarks Summit, PA, USA.
- Dusseault, M.B. and Fordham, C.J. (1993). Time-dependent behavior of rocks. **Comprehensive Rock Engineering Principles, Practice and Project: Rock Testing and Site Characterization.** London, Pergamon. 3: 119-149.
- Evans, I. (1961). The tensile strength of coal. **Colliery Engineering.** 38: 428-434.
- Fairhurst, C. (1961). Laboratory measurement of some physical properties of rock. In **Proceedings of the 4th U.S. Symposium on Rock Mechanics (USRMS).** 30 March-1 April 1961, University Park, Pennsylvania.
- Forster, I. (1967). Stability investigations applied to mining of evaporates, **Doctoral dissertation.** University of Newcastle upon Tyne.
- Fuenkajorn, K. (2007). Intrinsic variability of the mechanical properties of Maha Sarakham salt. **International Journal of Rock Mechanics and Mining Sciences.** 15(1): 33-48.
- Fuenkajorn, K. and Phueakphum, D. (2010). Effects of cyclic loading on mechanical properties of Maha Sarakham salt. **Engineering Geology.** 112 (1-4) 43-52.
- Fuenkajorn, K. and Daemen, J.J.K. (1988). Boreholes closure in salt. **Technical Report Prepared for The U.S. Nuclear Regulatory Commission.** Report No. NUREG/CR-5243 RW. University of Arizona.
- G.M.R. (2010). Subsidence prediction and impact assessment for Udon South Potash project. **Technical Report Prepared for Asia Pacific Potash Corporation Limited.** Suranaree University of Technology.

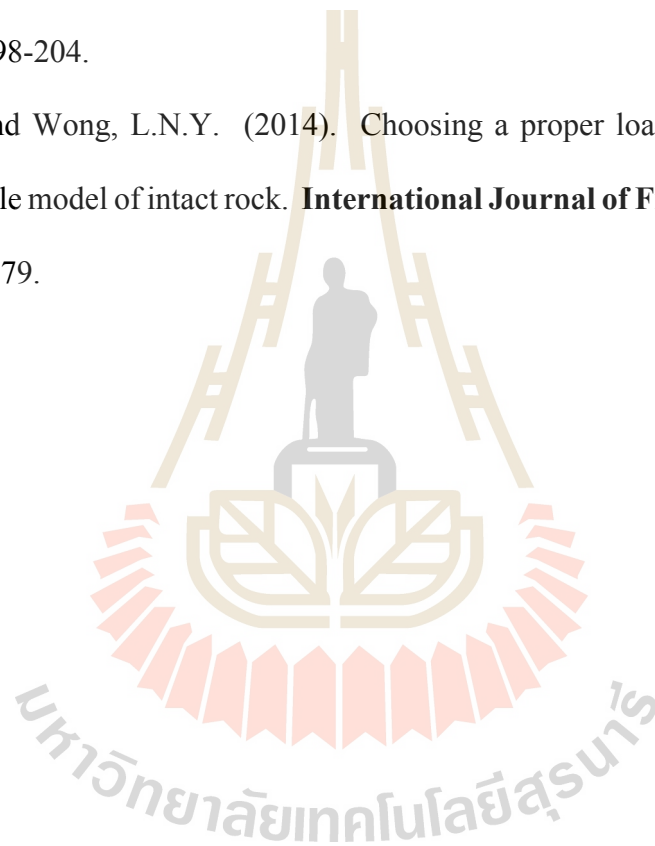
- Han, G., Bruno, M.S., Lao, K., Young, J., and Dorfmann, L. (2006). Gas Storage and Operations in Single-Bedded Salt Caverns: Stability Analyses. **SPE Gas Technology Symposium in Calgary**. Alberta, Canada.
- Itasca. (1992). **FLAC-Fast Lagrangian Analysis of Continua, Version 4.0, User Manual**. Itasca Consulting Group Inc., Minneapolis, MN, USA.
- Jaeger, J.C., Cook, N.G.W., and Zimmerman, R.W. (2007). **Fundamentals of Rock Mechanics Fourth Edition**, 4th edition, Blackwell publishing, Oxford.
- Jeremic, M.L. (1994). **Rock mechanics in salt mining**. Rotherdam: A. A. Balkema. pp. 530.
- Jianhong, Y., Wu, F.Q., and Sun, J.K. (2009) Estimation of the tensile elastic modulus using Brazilian disc by applying diametrically opposed concentrated loads. **International Journal of Rock Mechanics and Mining Sciences**. 48(3): 568-576.
- Knowles, M.K., Borns, D., Fredrich, J., Holcomb, D., Price, R., and Zeuch, D. (1998). Testing the disturbed zone around a rigid inclusion in salt. In **Proceedings of the Fourth Conference on the Mechanical Behavior of Salt**. (pp. 175-188). Clausthal, Germany: Trans Tech Publications.
- Kumar, A. (1968). The effect of stress rate and temperature on the strength of basalt and granite. **Geophysics**. 33(3): 501-510.
- Liang, W.G., Zhao, Y.S., Xu, S.G., and Dusseault, M.B. (2010). Effect of strain rate on the mechanical properties of salt rock. **International Journal of Rock Mechanics and Mining Sciences**. 48: 161-167.

- Liu, L.F., Pei, J.L., Ma, K., Zhou, H., and Hou, Z. (2010). Underground Storage of CO₂ and Energy. In **Proceedings of the Sino-German Conference**. (pp. 105-112). 6-7 July, 2010, Beijing, China.
- Luangthip, A., Khamrat, S., and Fuenkajorn, K. (2016). Effects of Carnallite Contents on Stability and Extraction Ratio of Potash Mine. In **9th Asian Rock Mechanics Symposium**. October 18-20, Bali, Indonesia.
- Nair, K. and Boresi, A. (1970). Stress analysis for time-dependent problems in rock mechanics. **International Society for Rock Mechanics**. 2(4-21): 531-536.
- Nair, R.S., Chang, C.Y., Singh, R.D., and Abdullah, A.M. (1974). Time-dependent analysis to predict closure in salt cavities. In **Proceedings of the 4th Symposium on Salt** (pp. 129-139). April 8-12, 1973, Houston, Texas.
- Obert, L., Windes, S.L., and Duvall, W.I. (1946). Standardized tests for determining the physical properties of mine rock. **US Bur. Mines Rep. Invest.** pp. 3891.
- Obert, L. and Duvall, W.I. (1967). **Rock Mechanics and the Design of Structures in Rock**. John Wiley and Sons. pp. 649.
- Phueakphum, D. (2003). Compressed-air energy storage in rock salt of the mahasarakham formation. **Master's Thesis**. Suranaree University of Technology.
- Phueakphum, D., Fuenkajorn, K., and Walsri, C. (2013). Effects of intermediate principal stress on tensile strength of rocks. **International Journal of Fracture**. 181: 163-175.
- Pomeroy, C.D. and Morgans, W.T.A. (1956). The tensile strength of coal. **British Journal of Applied Physics**. 7: 243-6.

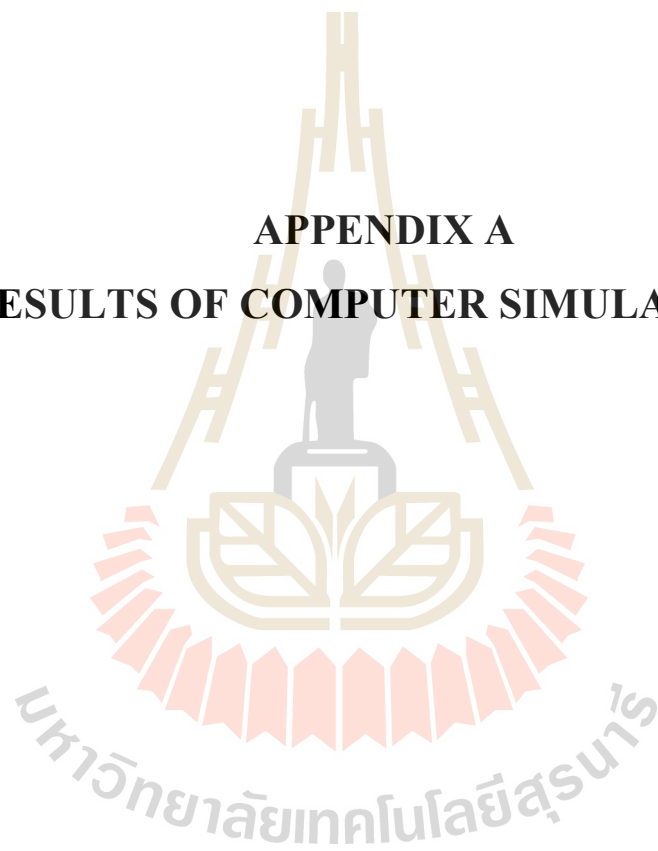
- Price, N.J. and Cosgrove, J.W. (1964). A study of the time-strain behavior of coal measure rocks. **International Journal of Rock Mechanics and Mining Sciences**. 1(2): 277-303.
- Sen, G.C. (1961). An investigation into the stability of room and pillar workings in rock salt. **Doctoral dissertation**. University of Newcastle upon Tyne.
- Senseny, P.E. (1983). Review of Constitutive Laws Used to Describe the Creep of Salt. **Report ONWI-295**. Columbus, Ohio: Office of Nuclear Waste Isolation, Battelle Memorial Institute.
- Snyder, V.W. (1983). Analysis of beam building using fully grouted roof bolts. In **Proceedings of the International Symposium on Rock Bolting** (pp. 187-194). Abisko, Sweden.
- Sriapai, T., Walsri, C., and Fuenkajorn, K. (2012). Effect of temperature on compressive and tensile strength of salt. **ScienceAsia**. 38: 166-174.
- Stimpson, B. and Ahmed, M. (1992). Failure of a linear voussoir arch: a laboratory and numerical study. **Canadian Geotechnical Journal**. 29: 188-194.
- Swift, G.M. and Reddish, D.J. (2005). Underground excavations in rock salt. **Geotechnical & Geological Engineering**. 23(1): 17-42.
- Thirumalai, K. and Demou, S.G. (1974). Thermal expansion behavior of intact and thermally fractured mine rocks. **International Journal of Rock Mechanics and Mining Sciences**. 17: 60-71.
- Voznesenskii, A.S., Krasilov, M.N., Kutkin, Y.O., Tavostin, M.N., and Osipov, Y.V. (2017). Features of interrelations between acoustic quality factor and strength of rock salt during fatigue cyclic loadings. **International Journal of Fatigue**. 97: 70-78.

- Wang, T., Yan, X., Yang, X., and Jiang, T. (2012). Roof stability evaluation of bedded rock salt cavern used as underground gas storage. **Research Journal of Applied Sciences, Engineering and Technology**. 4(20): 4160-4170.
- Wang, T., Yang, C., Shi, X., Ma, H., Li, Y., Yang, Y., and Daemen, J.J.K. (2015). Failure analysis of thick interlayer from leaching of bedded salt caverns. **International Journal of Rock Mechanics and Mining Sciences**. 73: 175-183.
- Wang, W., Wang, M., and Liu, X. (2016). Study on Mechanical Features of Brazilian Splitting Fatigue Tests of Salt Rock. **Advances in Civil Engineering**. 2016: 1-10.
- Warren, J. (1999). **Evaporites: Their evolution and economics**. Philadelphia: Blackwell Science. pp. 235-239.
- Wendai, L. (2000). Regression analysis, linear regression and probit regression in 13 chapters. **SPSS for Windows: statistical analysis**. Publishing House of Electronics Industry. Beijing.
- Wetchasat, K. (2002). Assessment of mechanical performance of rock salt formations for nuclear waste repository in northeastern Thailand. **Master's Thesis**. School of Geotechnology. Suranaree University of Technology.
- Wisetsaen, S., Walsri, C., and Fuenkajorn, K. (2015). Effects of loading rate and temperature on tensile strength and deformation of rock salt. **International Journal of Rock Mechanics and Mining Sciences**. 73: 10-14.
- Xiao, J.Q., Ding, D.X., Jiang, F.L., and Xu, G. (2010). Fatigue damage variable and evolution of rock subjected to cyclic loading. **International Journal of Rock Mechanics and Mining Sciences**. 47: 461-468.

- Yang, C., Wang, T., Qu, D.A., Ma, H., Li, Y., Shi, X., and Daemen, J.J.K. (2016). Feasibility analysis of using horizontal caverns for underground gas storage: A case study of Yunying salt district. **Journal of Natural Gas Science and Engineering**. 36: 252-266.
- Yokoyama, T.A. (1988). A microcomputer-aided four-point test system for determining uniaxial stress-strain curves. **Journal of Testing and Evaluation**. 16: 198-204.
- Zhang, X. and Wong, L.N.Y. (2014). Choosing a proper loading rate for bonded-particle model of intact rock. **International Journal of Fracture rock**. 189(2): 163-179.



APPENDIX A
RESULTS OF COMPUTER SIMULATIONS



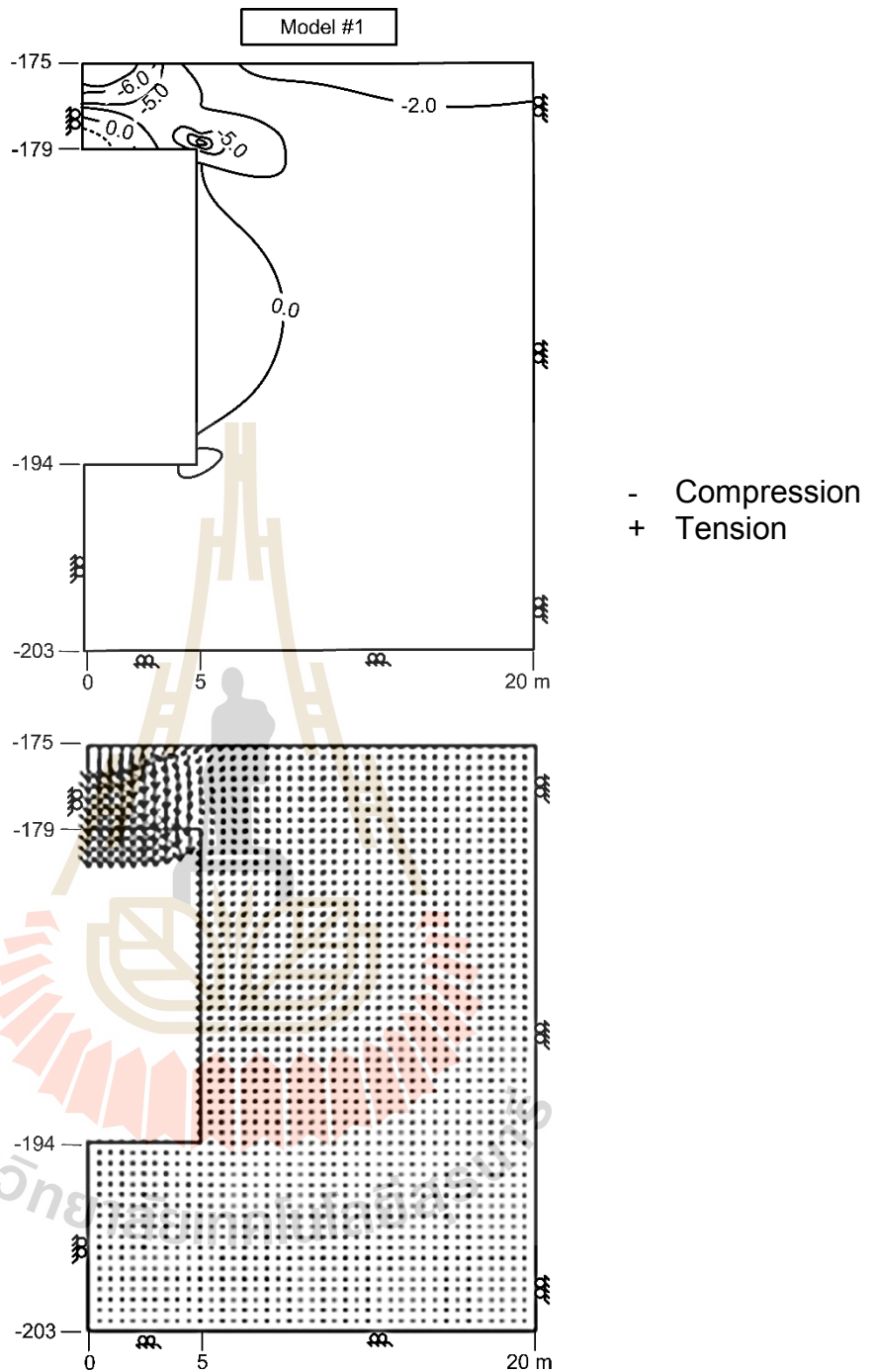


Figure A.1 Stress distribution (top) and displacement vectors (bottom) in mine roof for depths of 175 m and width of 10 m with minimum pressure at 20 % of in-situ stress

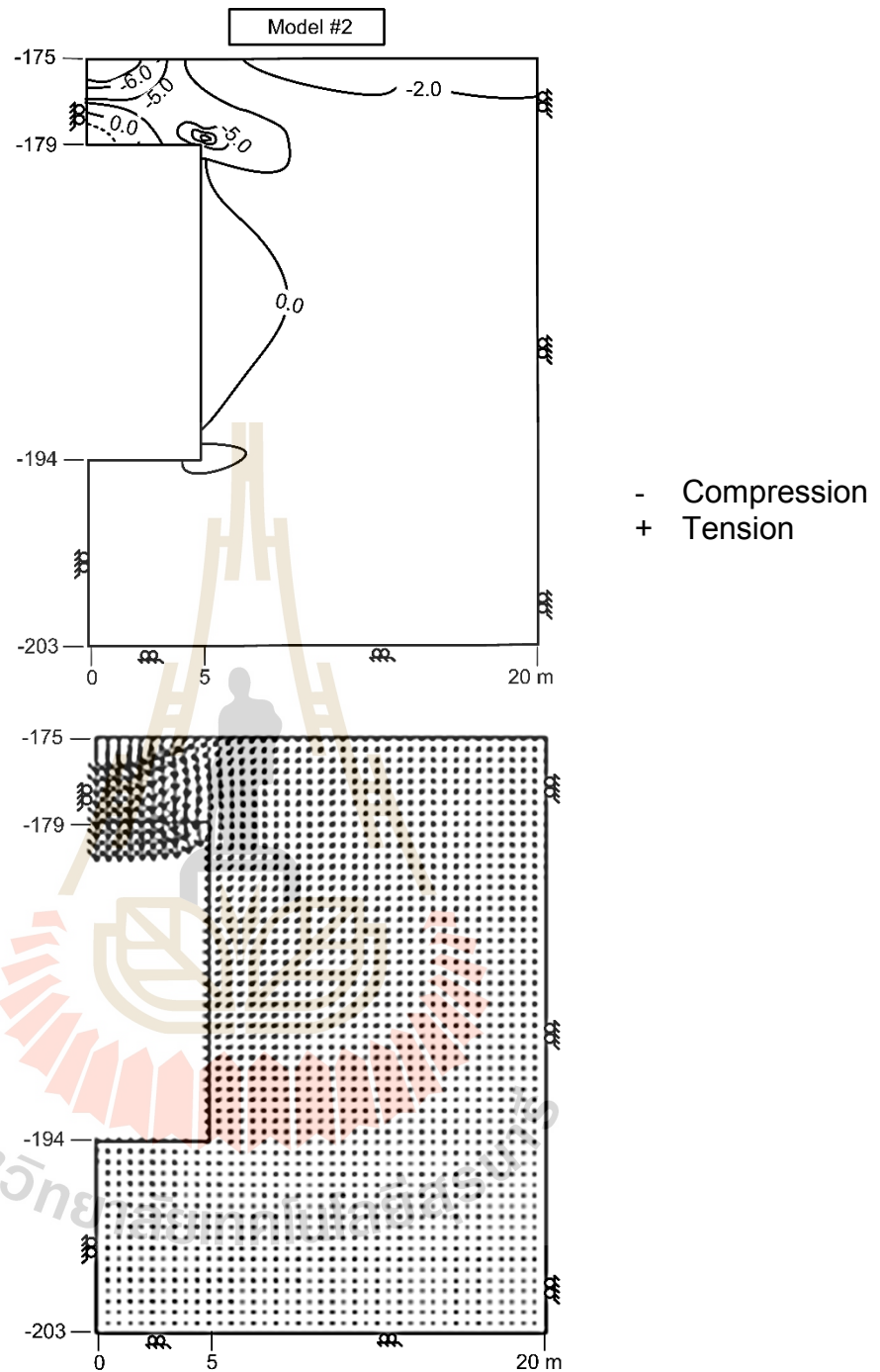


Figure A.2 Stress distribution (top) and displacement vectors (bottom) in mine roof for depths of 175 m and width of 10 m with minimum pressure at 30 % of in-situ stress

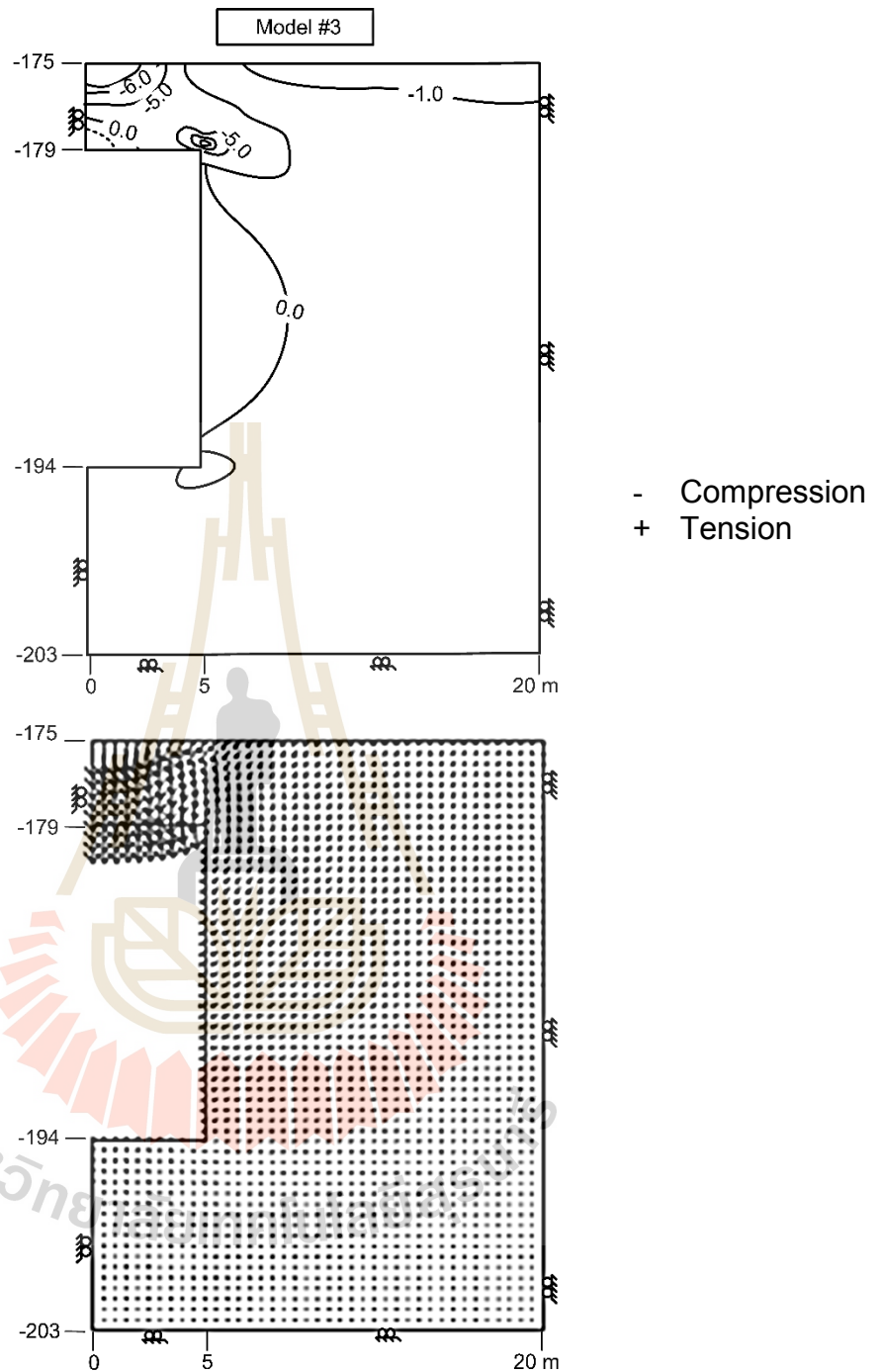


Figure A.3 Stress distribution (top) and displacement vectors (bottom) in mine roof for depths of 175 m and width of 10 m with minimum pressure at 40 % of in-situ stress

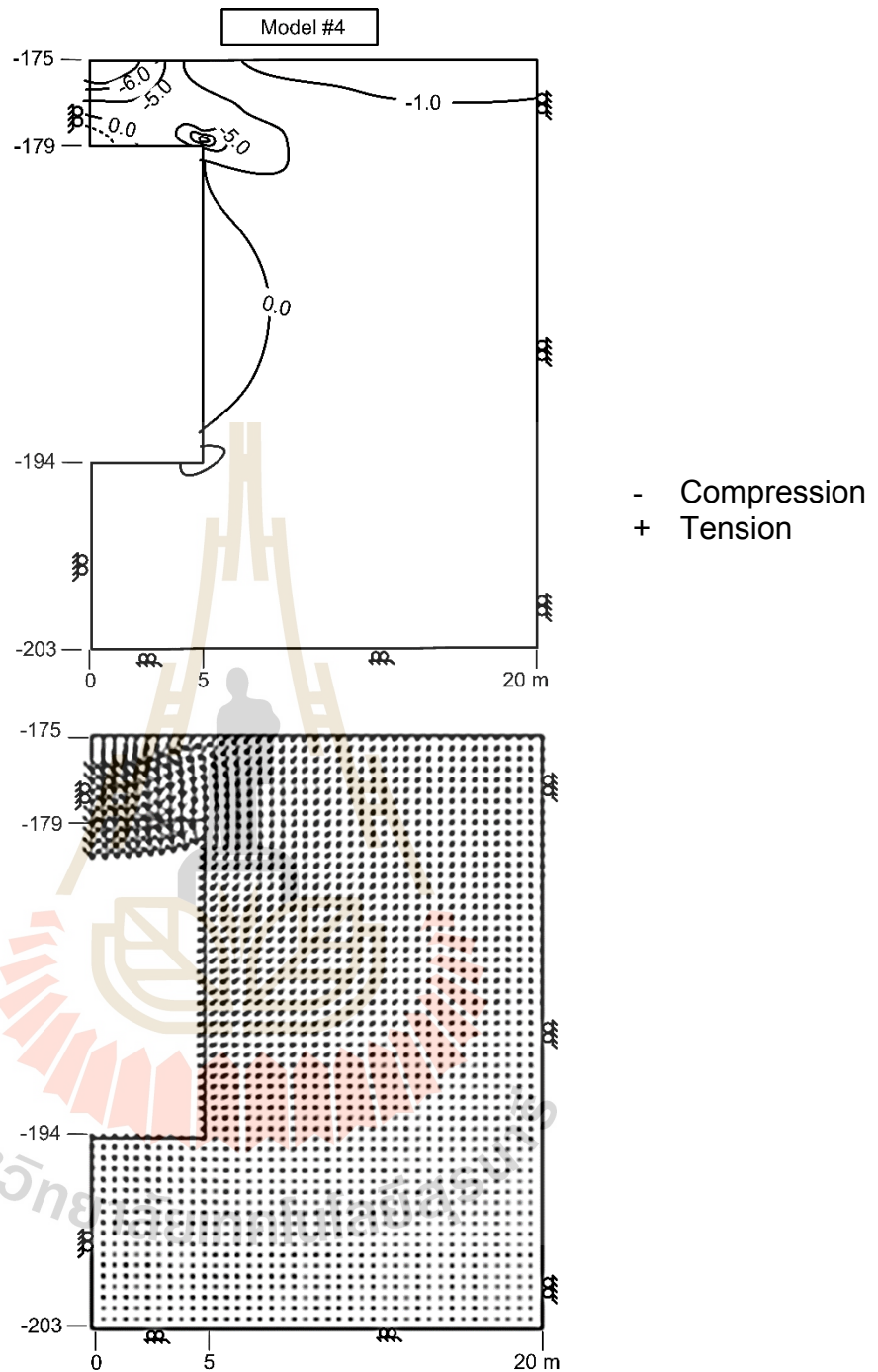


Figure A.4 Stress distribution (top) and displacement vectors (bottom) in mine roof for depths of 175 m and width of 10 m with minimum pressure at 50 % of in-situ stress

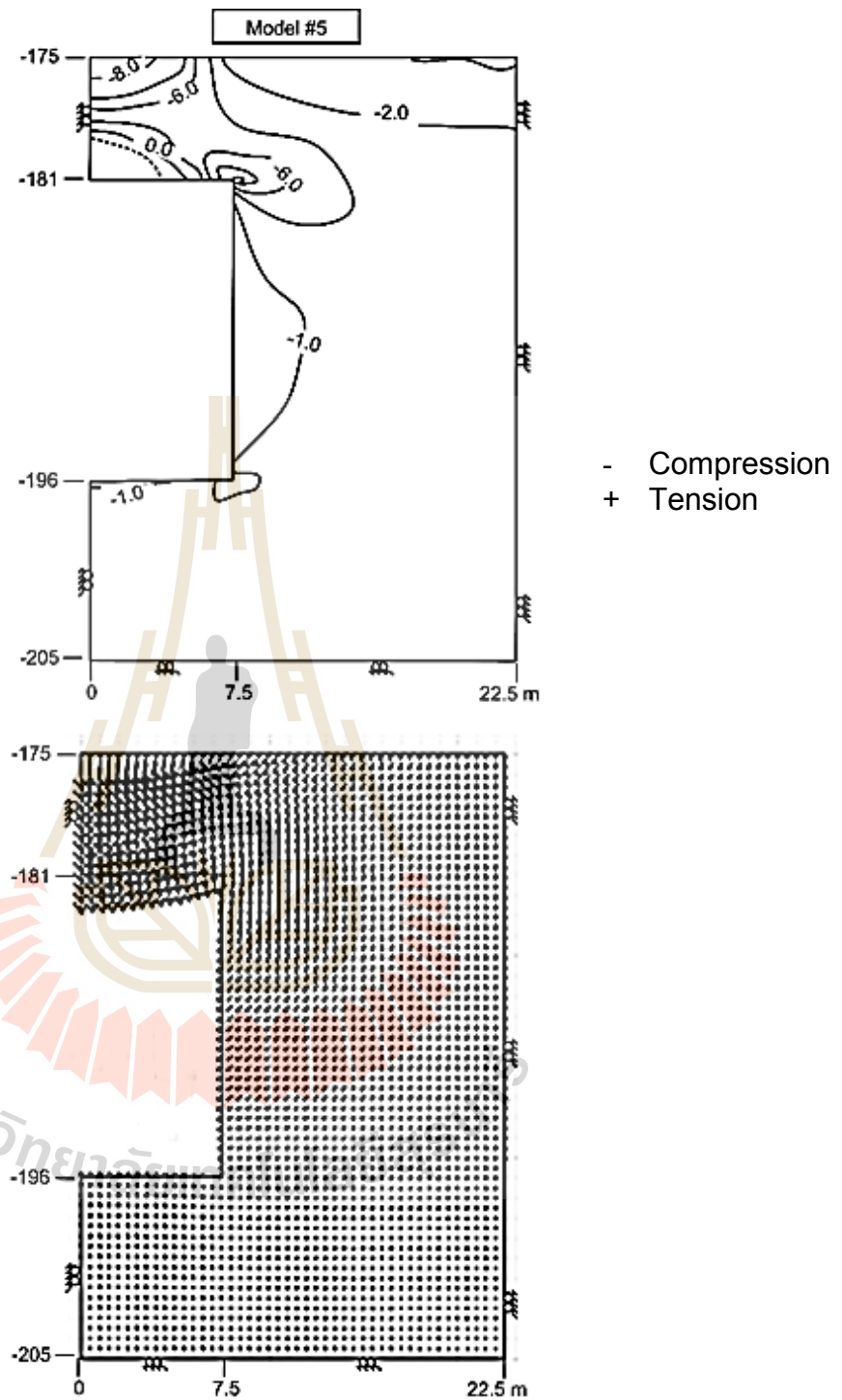


Figure A.5 Stress distribution (top) and displacement vectors (bottom) in mine roof for depths of 175 m and width of 15 m with minimum pressure at 20 % of in-situ stress

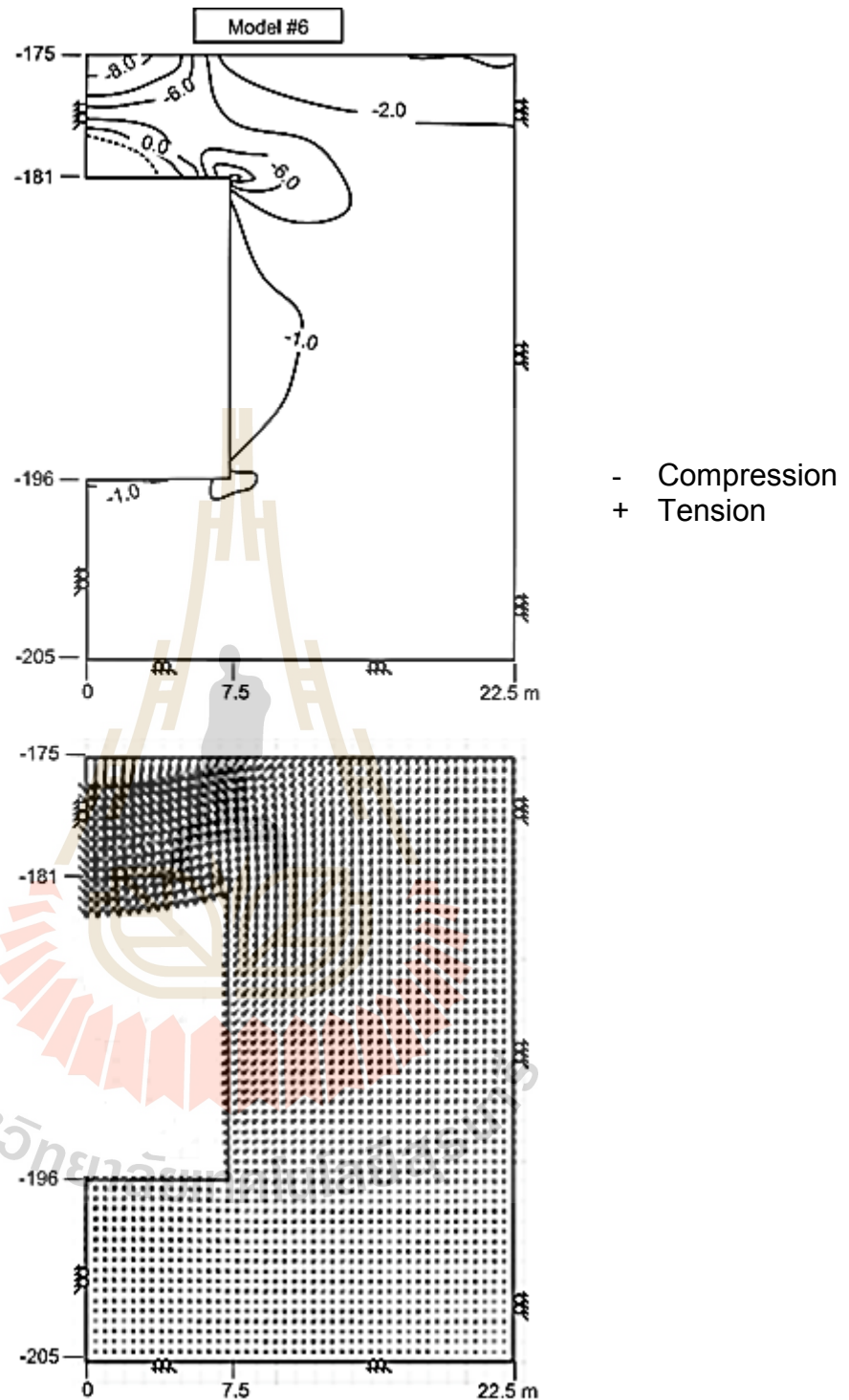


Figure A.6 Stress distribution (top) and displacement vectors (bottom) in mine roof for depths of 175 m and width of 15 m with minimum pressure at 30 % of in-situ stress

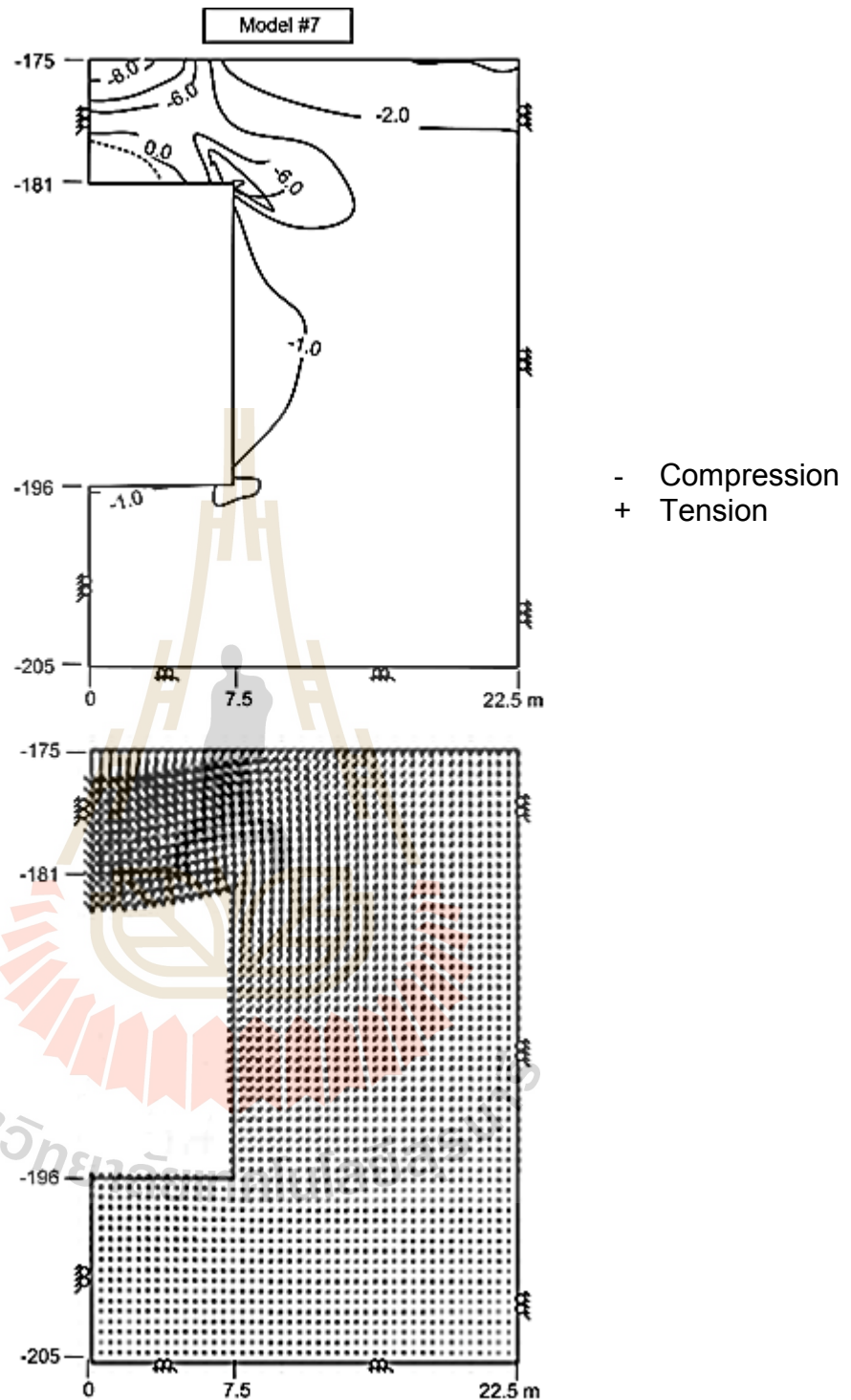


Figure A.7 Stress distribution (top) and displacement vectors (bottom) in mine roof for depths of 175 m and width of 15 m with minimum pressure at 40 % of in-situ stress

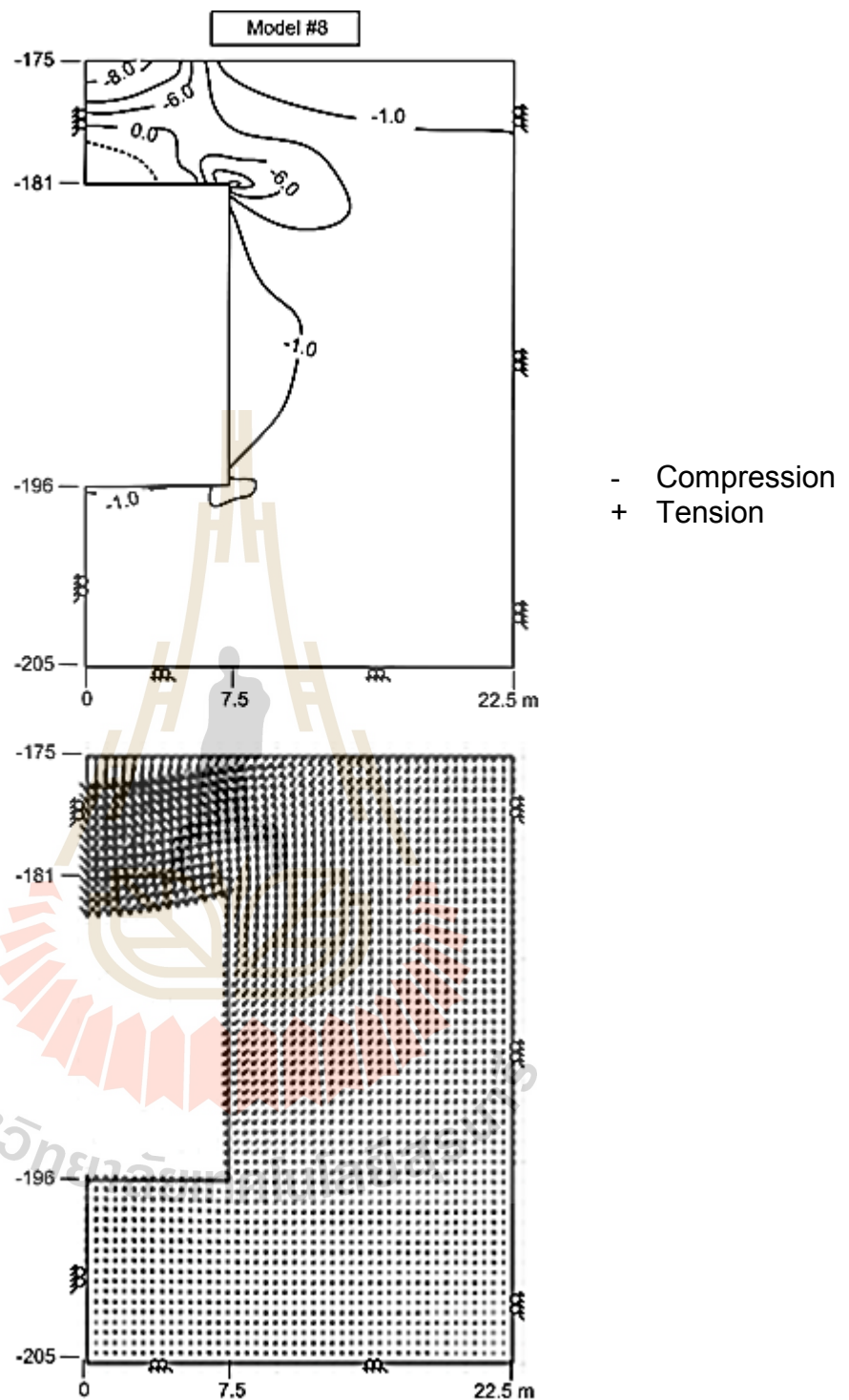


Figure A.8 Stress distribution (top) and displacement vectors (bottom) in mine roof for depths of 175 m and width of 15 m with minimum pressure at 50 % of in-situ stress

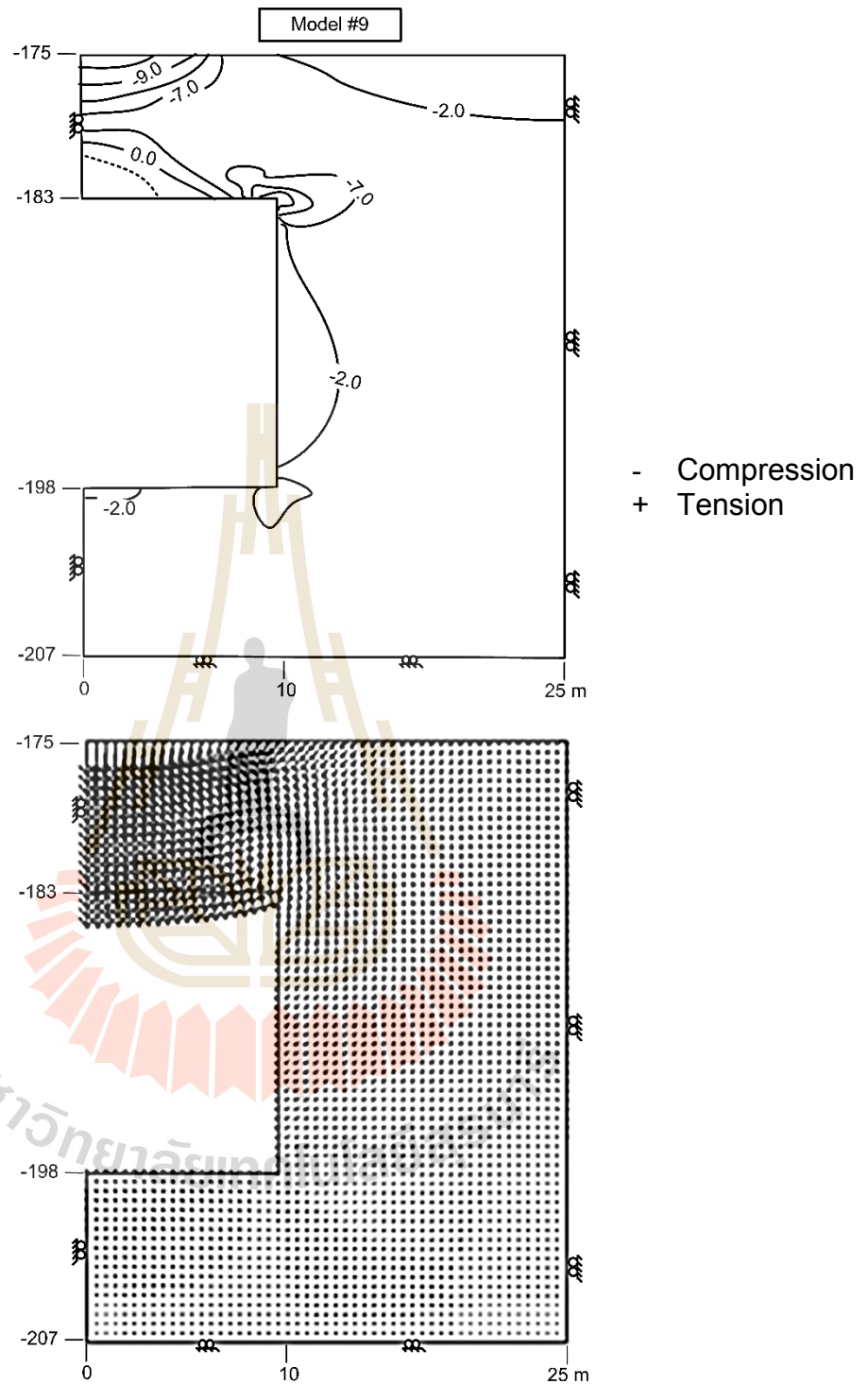


Figure A.9 Stress distribution (top) and displacement vectors (bottom) in mine roof for depths of 175 m and width of 20 m with minimum pressure at 20 % of in-situ stress

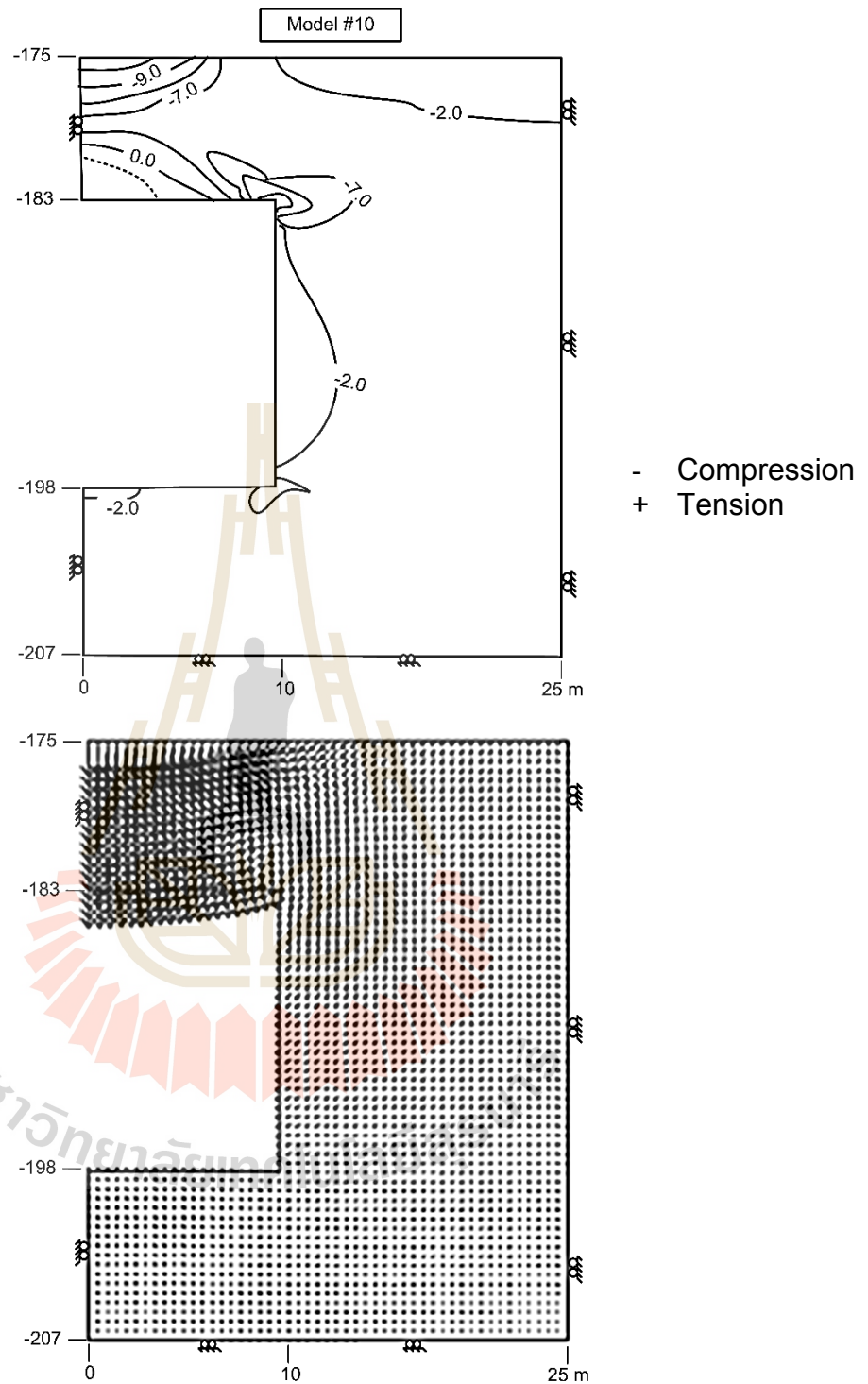


Figure A.10 Stress distribution (top) and displacement vectors (bottom) in mine roof for depths of 175 m and width of 20 m with minimum pressure at 30 % of in-situ stress

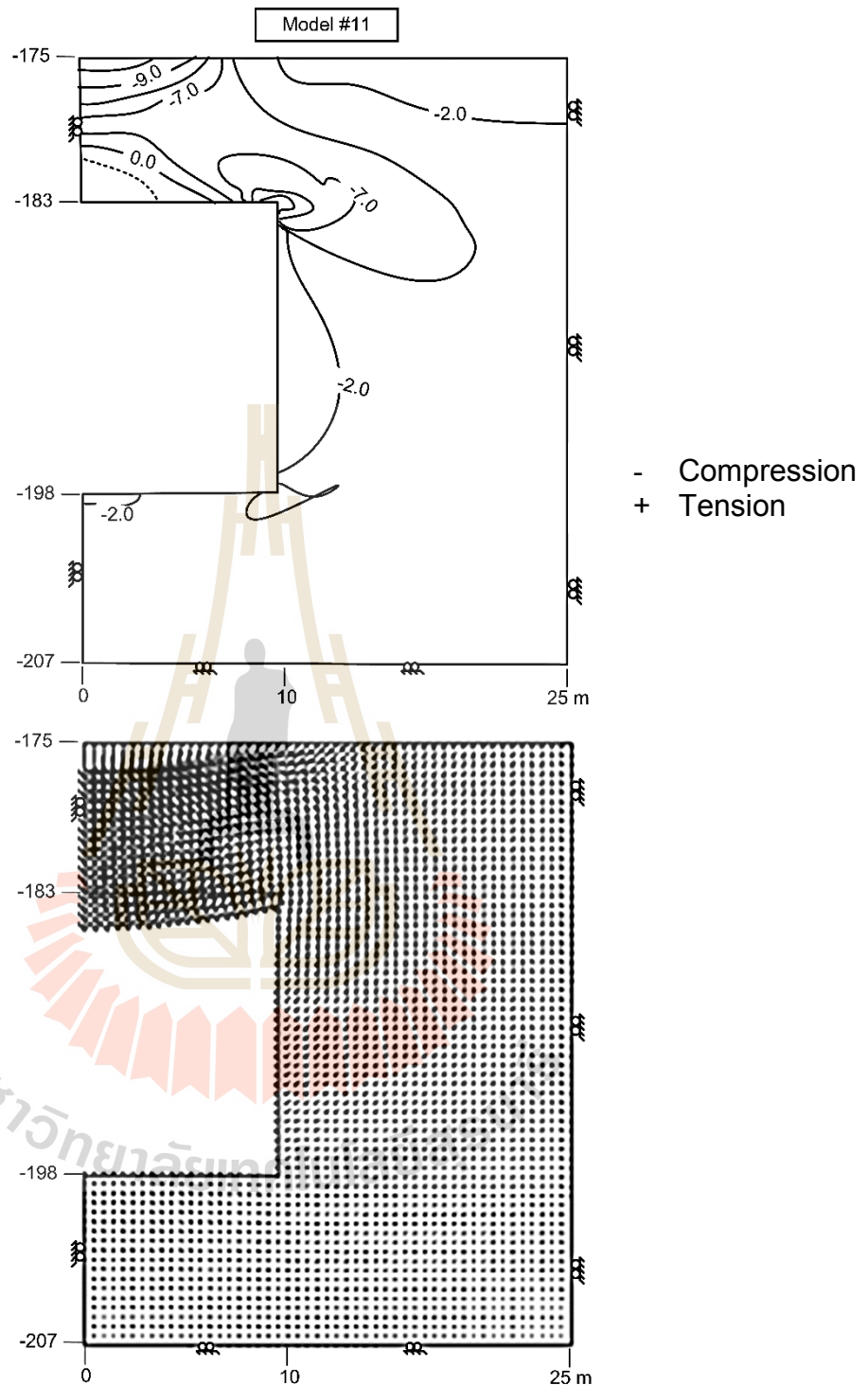


Figure A.11 Stress distribution (top) and displacement vectors (bottom) in mine roof for depths of 175 m and width of 20 m with minimum pressure at 40 % of in-situ stress

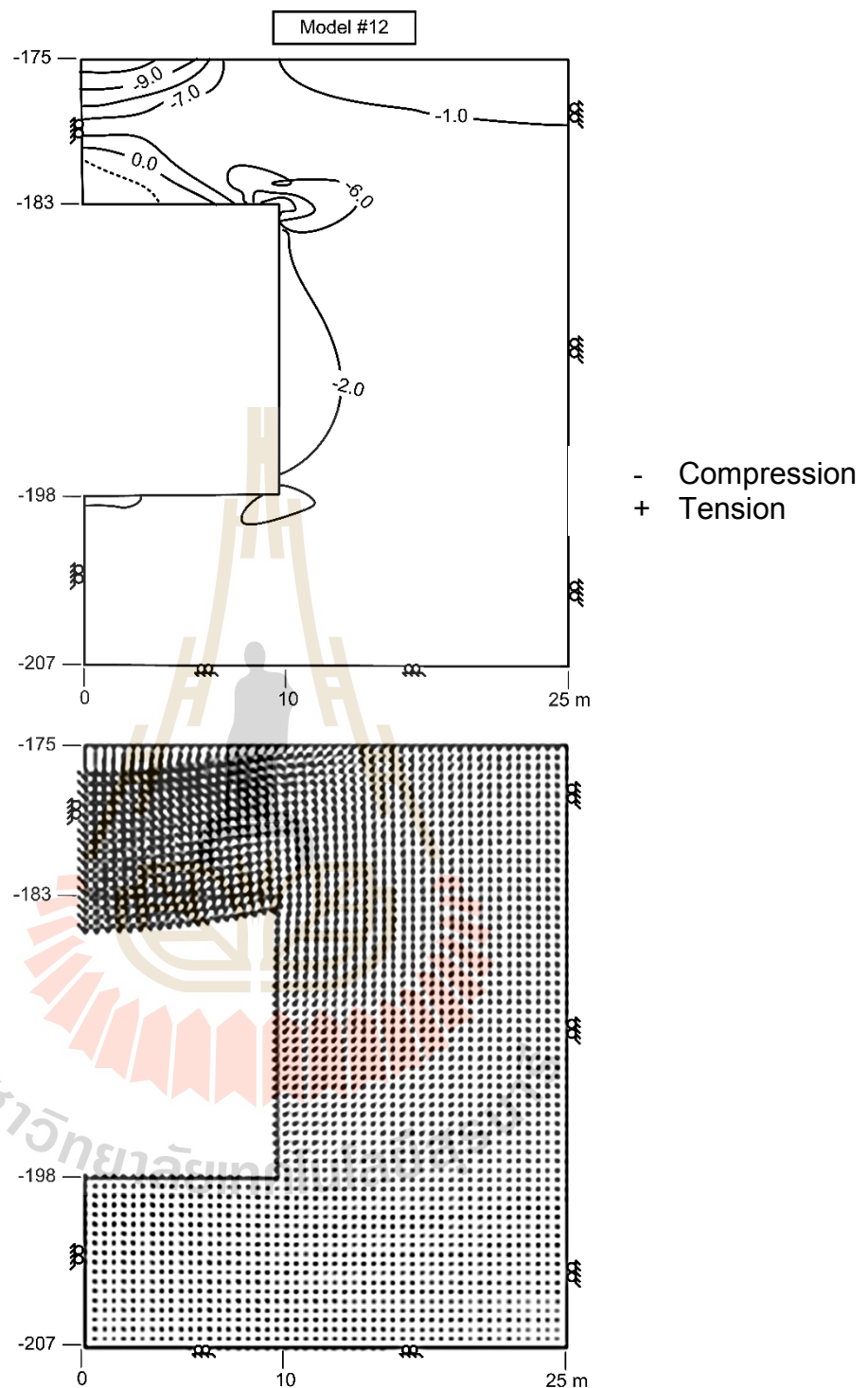


Figure A.12 Stress distribution (top) and displacement vectors (bottom) in mine roof for depths of 175 m and width of 20 m with minimum pressure at 50 % of in-situ stress

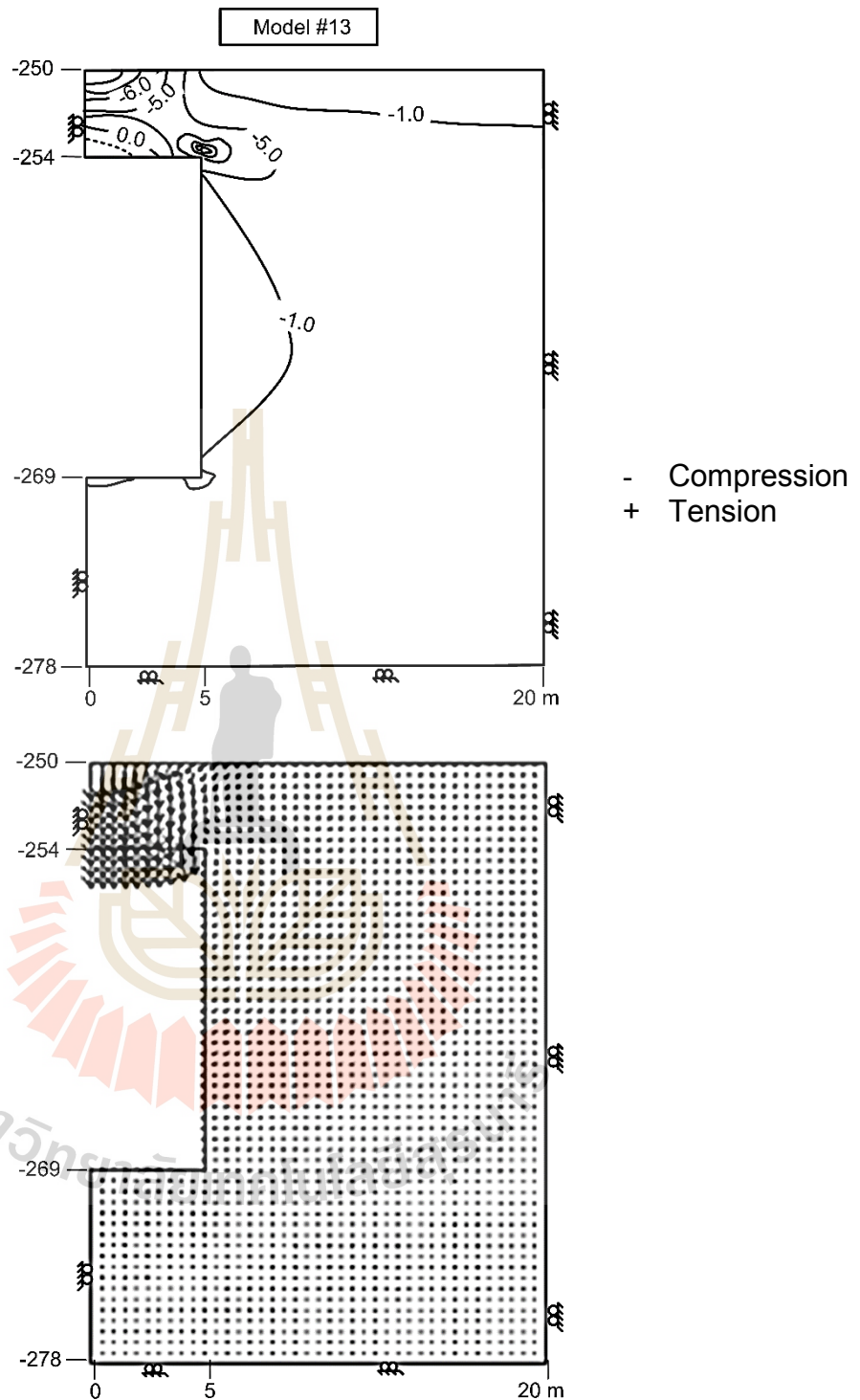


Figure A.13 Stress distribution (top) and displacement vectors (bottom) in mine roof for depths of 250 m and width of 10 m with minimum pressure at 20 % of in-situ stress

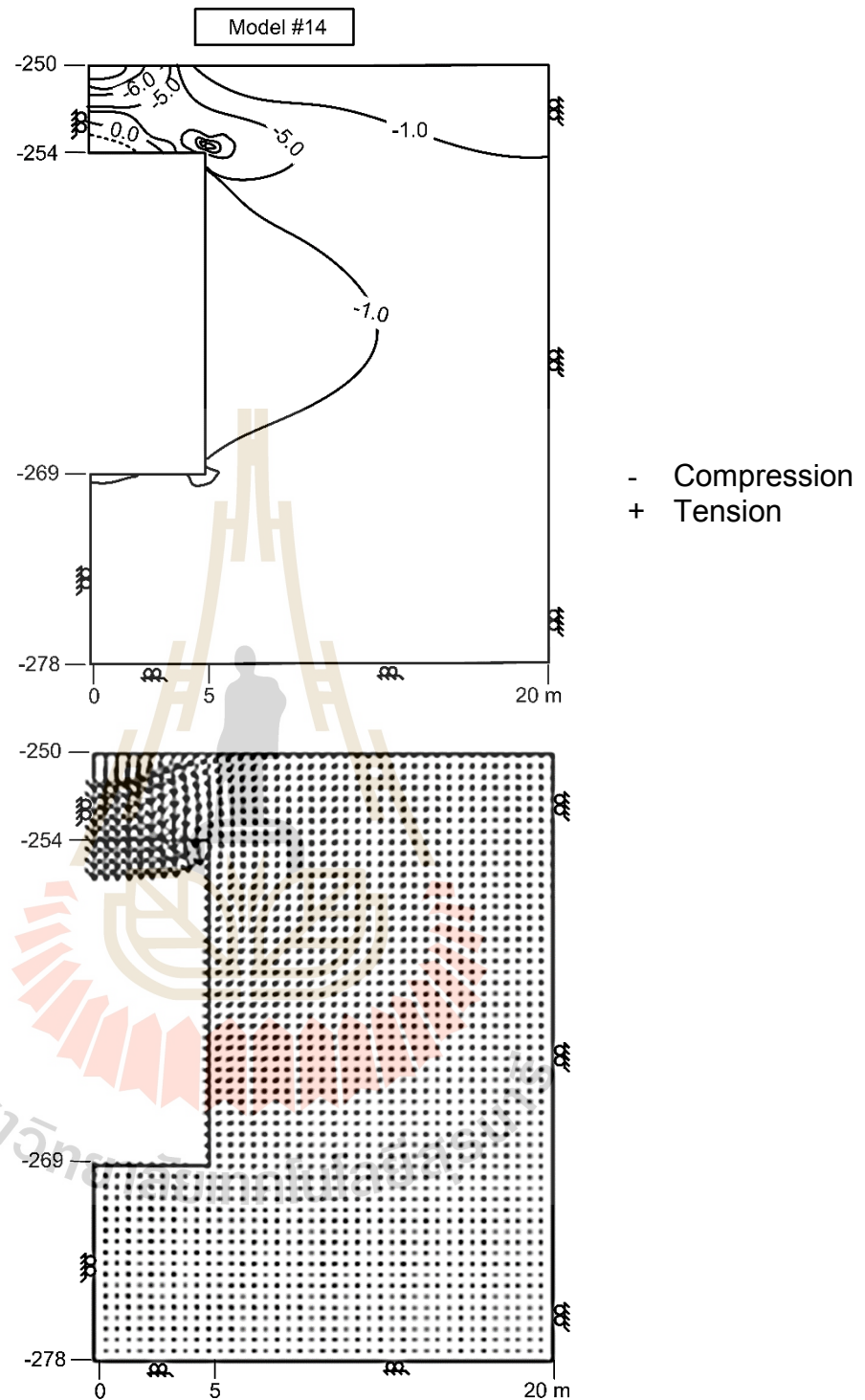


Figure A.14 Stress distribution (top) and displacement vectors (bottom) in mine roof for depths of 250 m and width of 10 m with minimum pressure at 30 % of in-situ stress

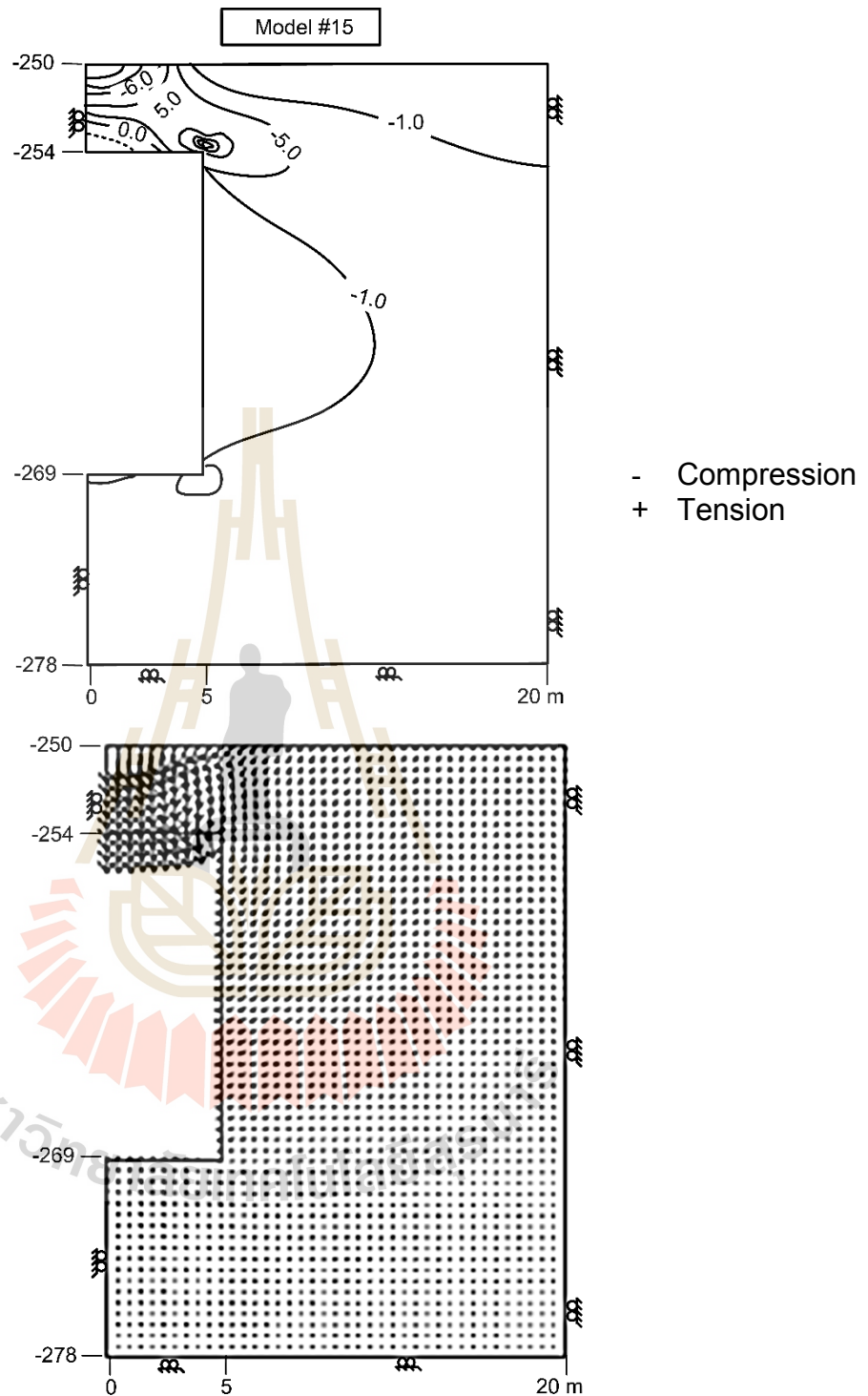


Figure A.15 Stress distribution (top) and displacement vectors (bottom) in mine roof for depths of 250 m and width of 10 m with minimum pressure at 40 % of in-situ stress

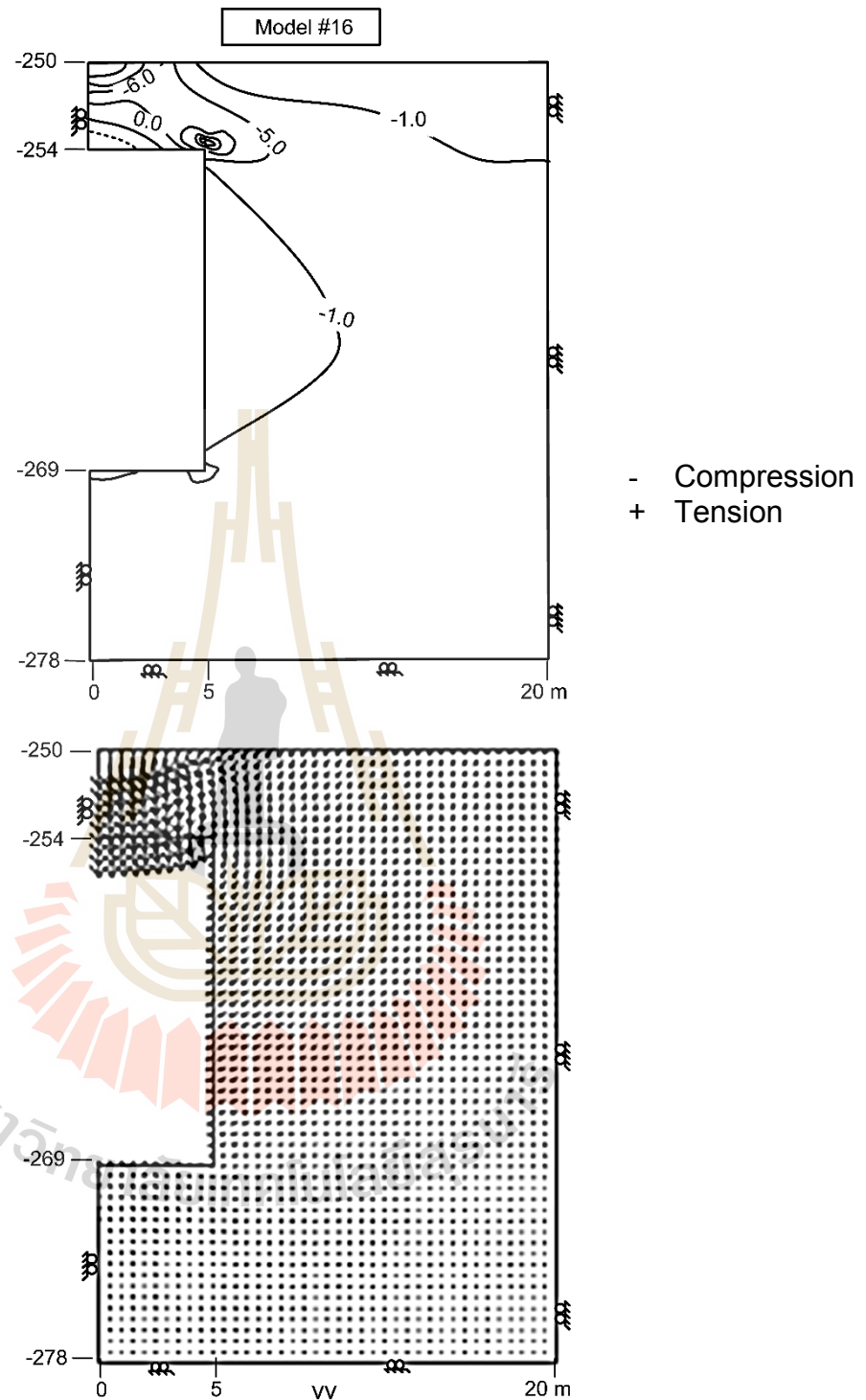


Figure A.16 Stress distribution (top) and displacement vectors (bottom) in mine roof for depths of 250 m and width of 10 m with minimum pressure at 50 % of in-situ stress

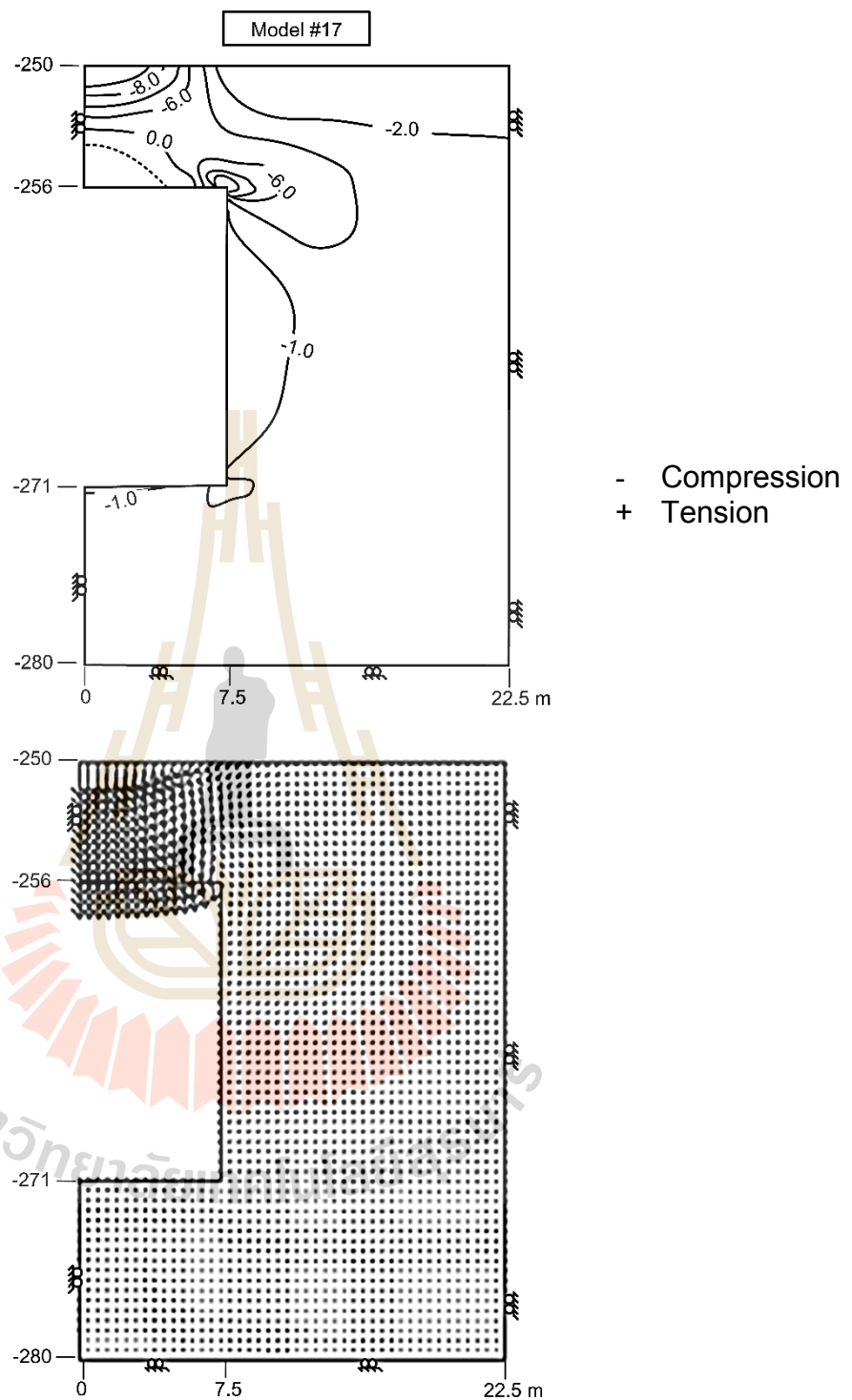


Figure A.17 Stress distribution (top) and displacement vectors (bottom) in mine roof for depths of 250 m and width of 15 m with minimum pressure at 20 % of in-situ stress

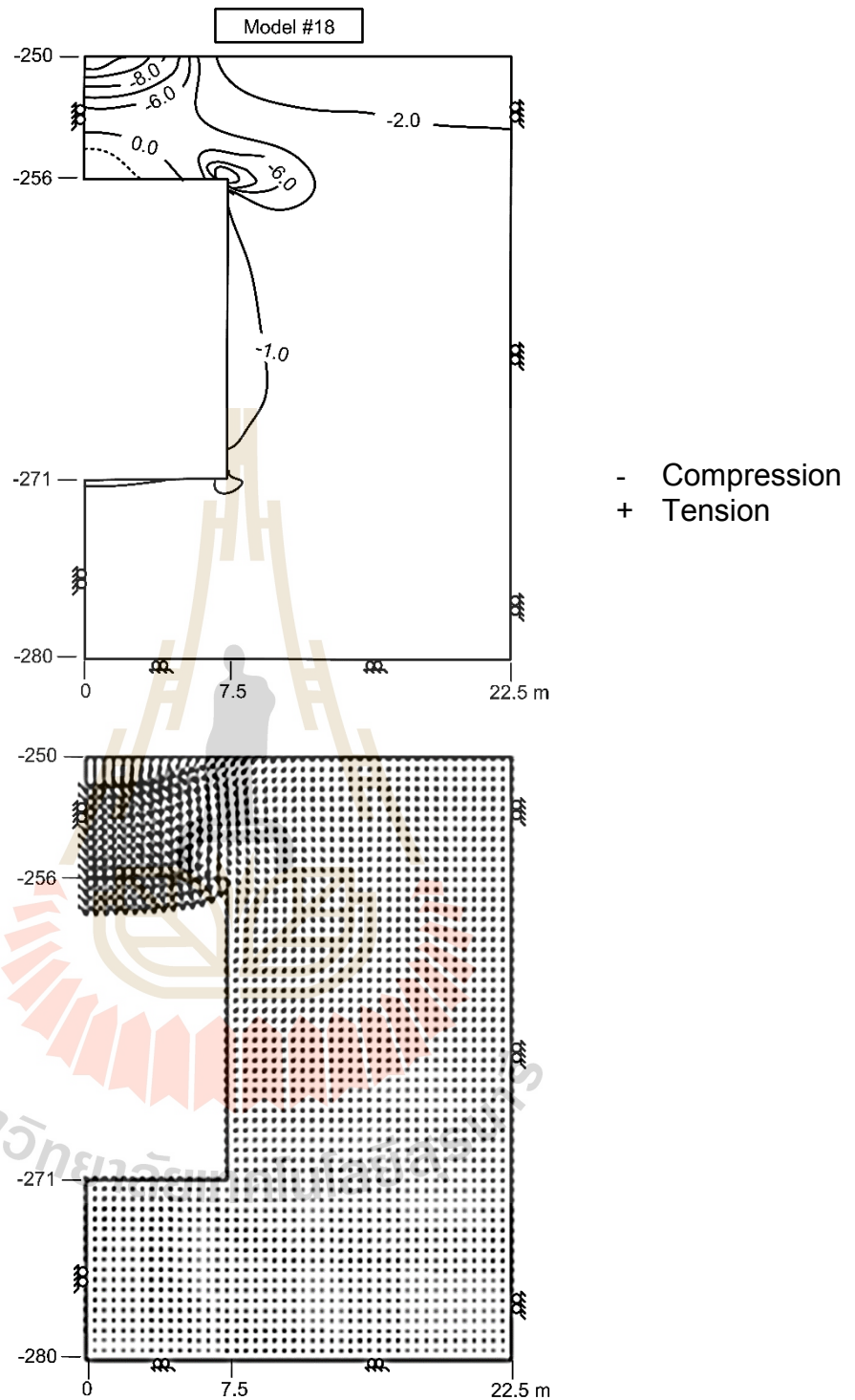


Figure A.18 Stress distribution (top) and displacement vectors (bottom) in mine roof for depths of 250 m and width of 15 m with minimum pressure at 30 % of in-situ stress

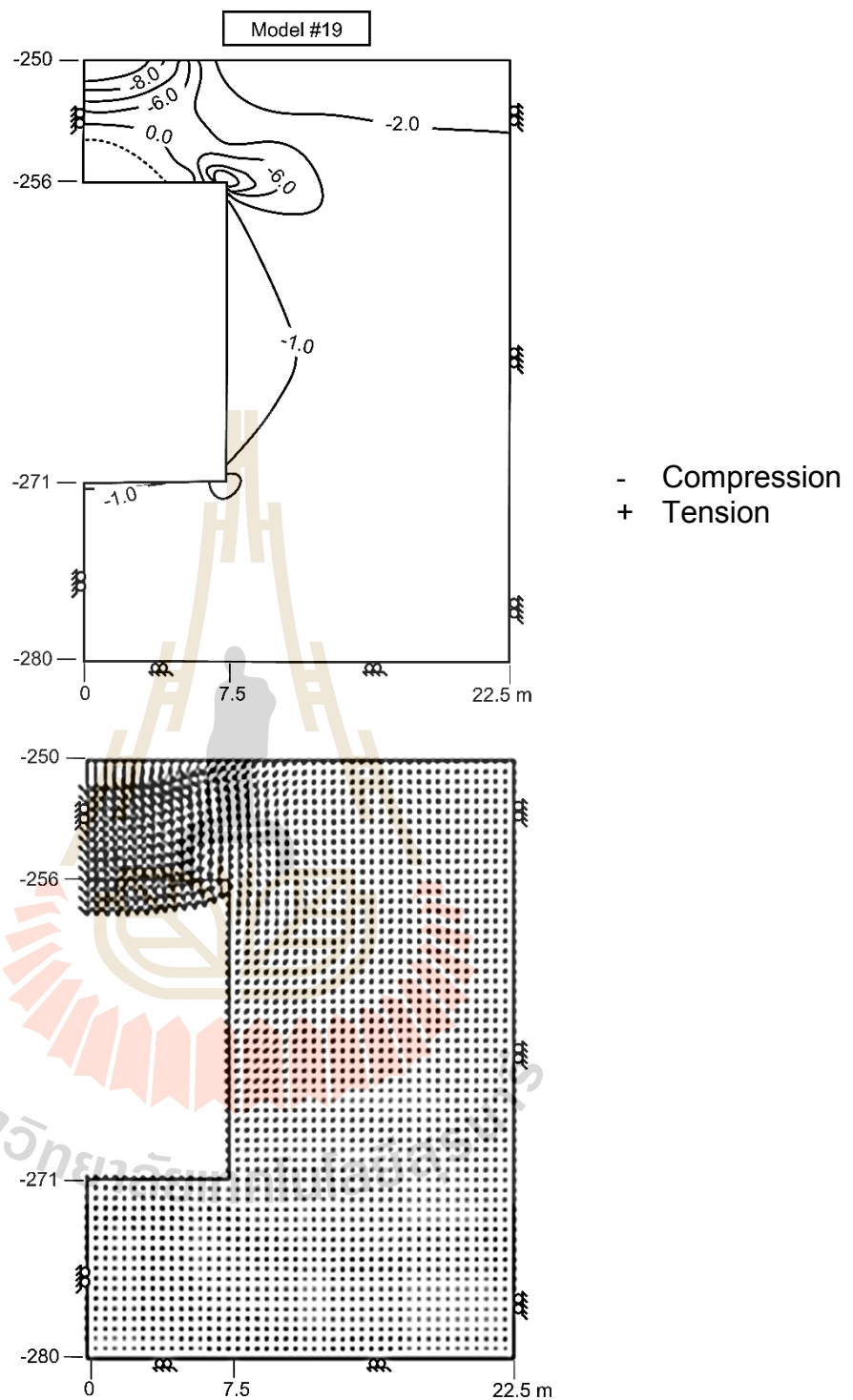


Figure A.19 Stress distribution (top) and displacement vectors (bottom) in mine roof for depths of 250 m and width of 15 m with minimum pressure at 40 % of in-situ stress

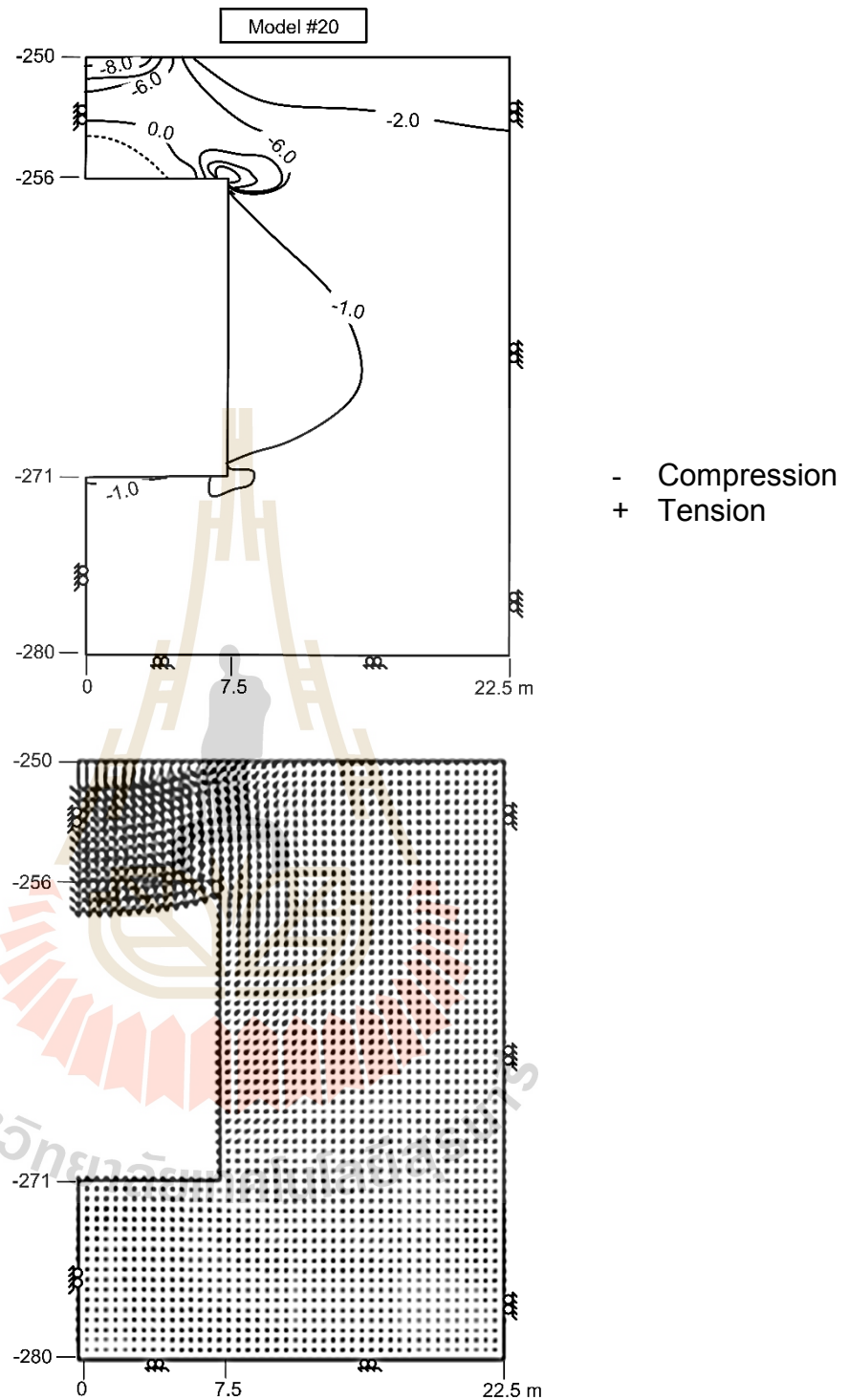


Figure A.20 Stress distribution (top) and displacement vectors (bottom) in mine roof for depths of 250 m and width of 15 m with minimum pressure at 50 % of in-situ stress

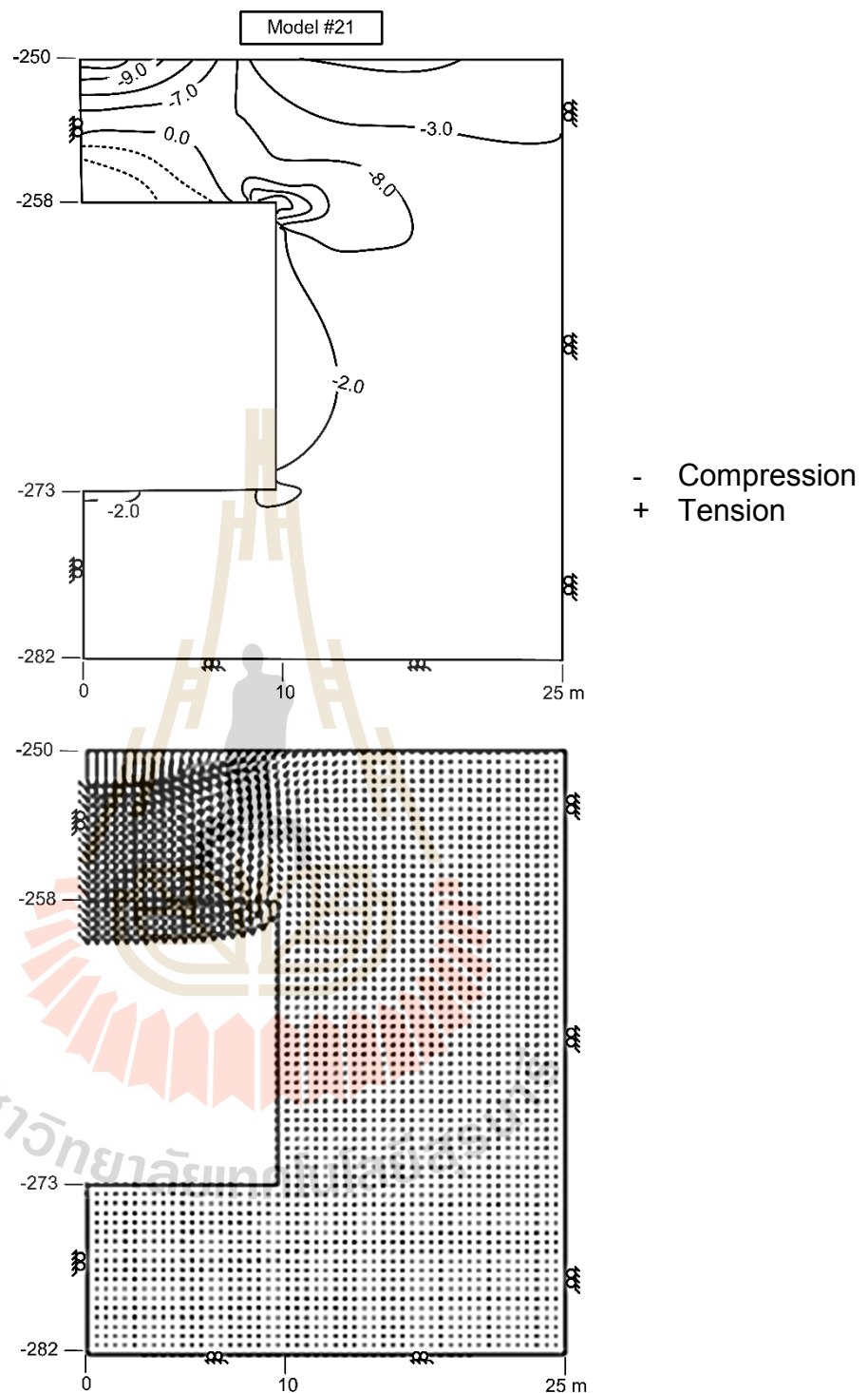


Figure A.21 Stress distribution (top) and displacement vectors (bottom) in mine roof for depths of 250 m and width of 20 m with minimum pressure at 20 % of in-situ stress

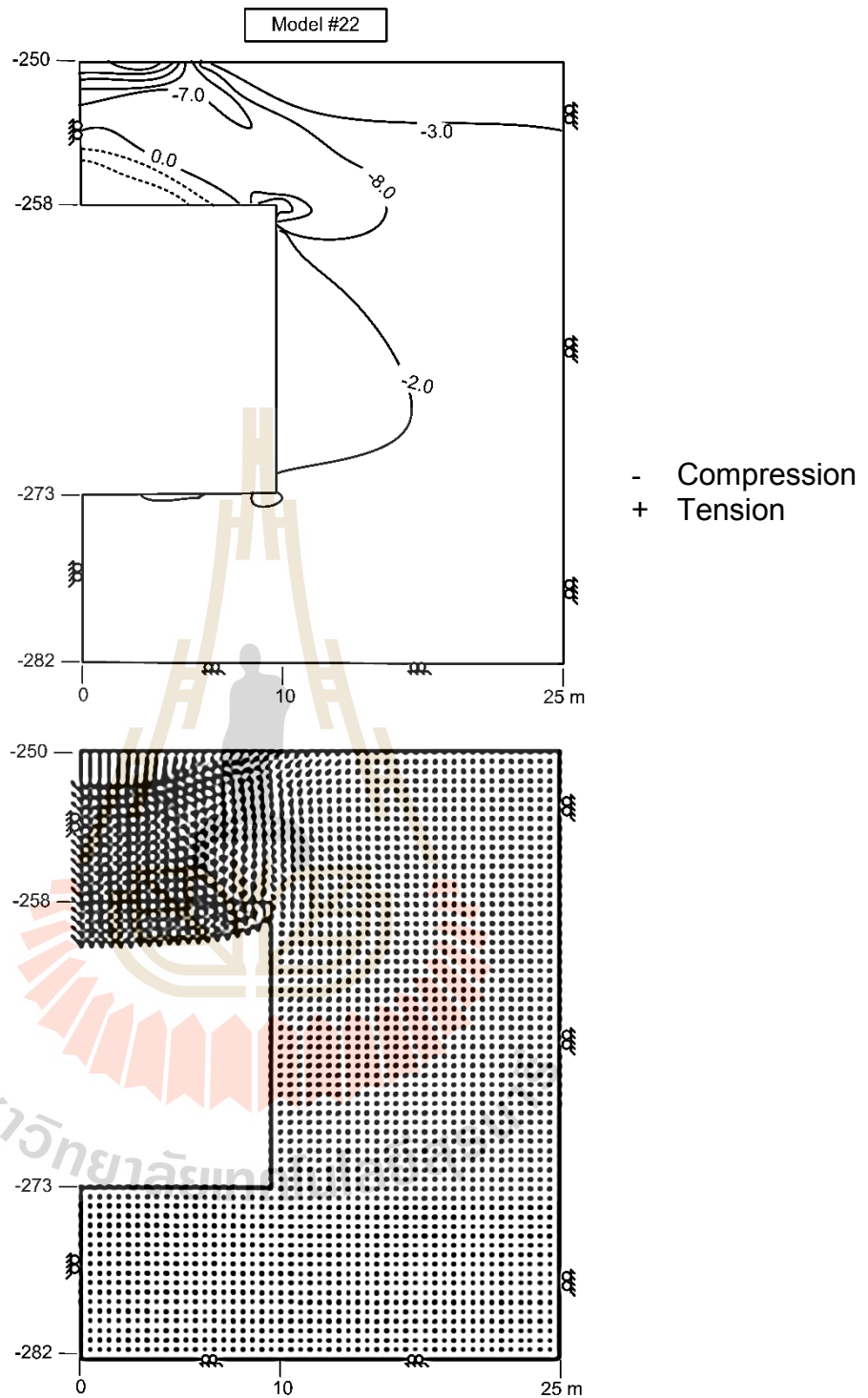


Figure A.22 Stress distribution (top) and displacement vectors (bottom) in mine roof for depths of 250 m and width of 20 m with minimum pressure at 30 % of in-situ stress

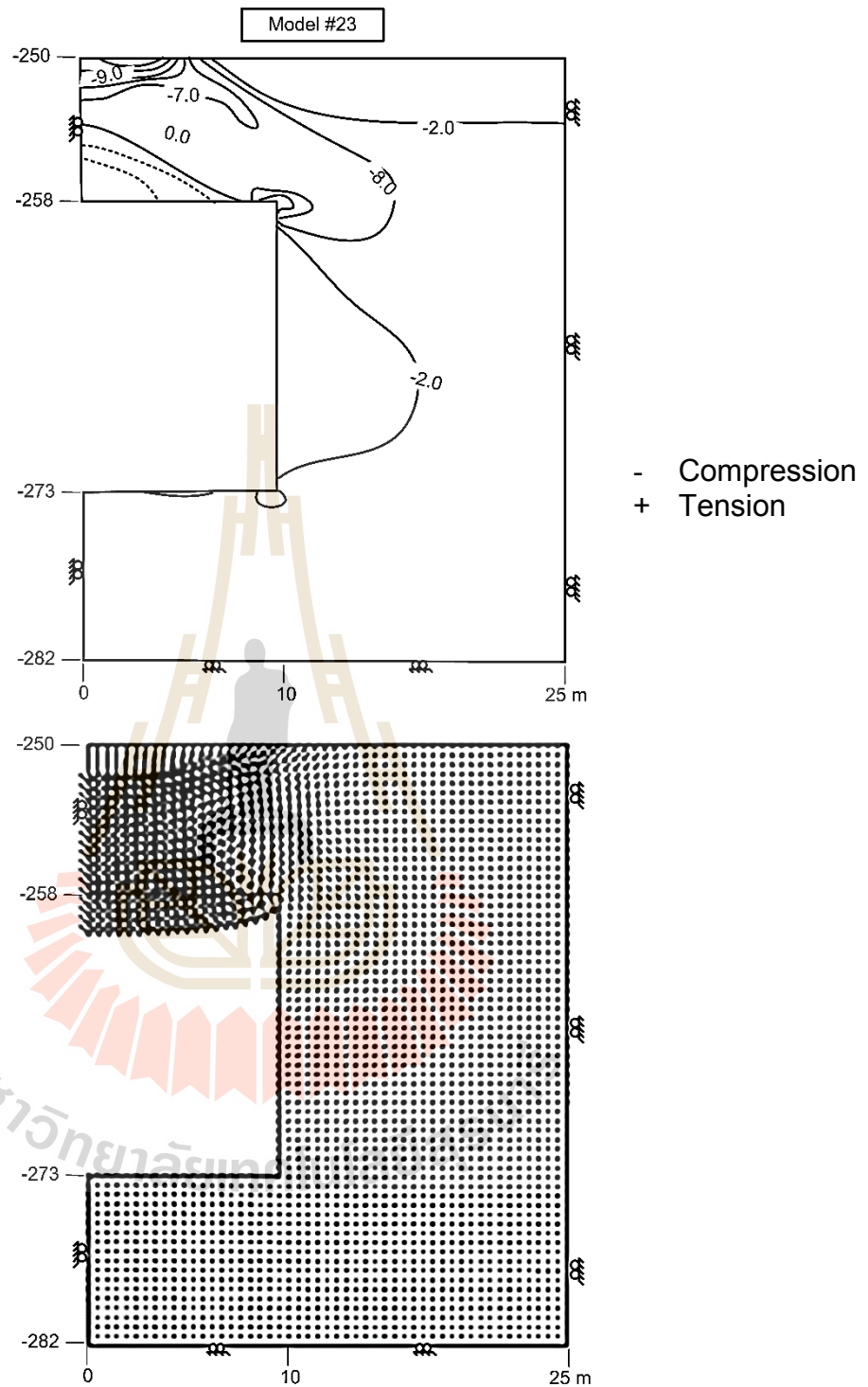


Figure A.23 Stress distribution (top) and displacement vectors (bottom) in mine roof for depths of 250 m and width of 20 m with minimum pressure at 40 % of in-situ stress

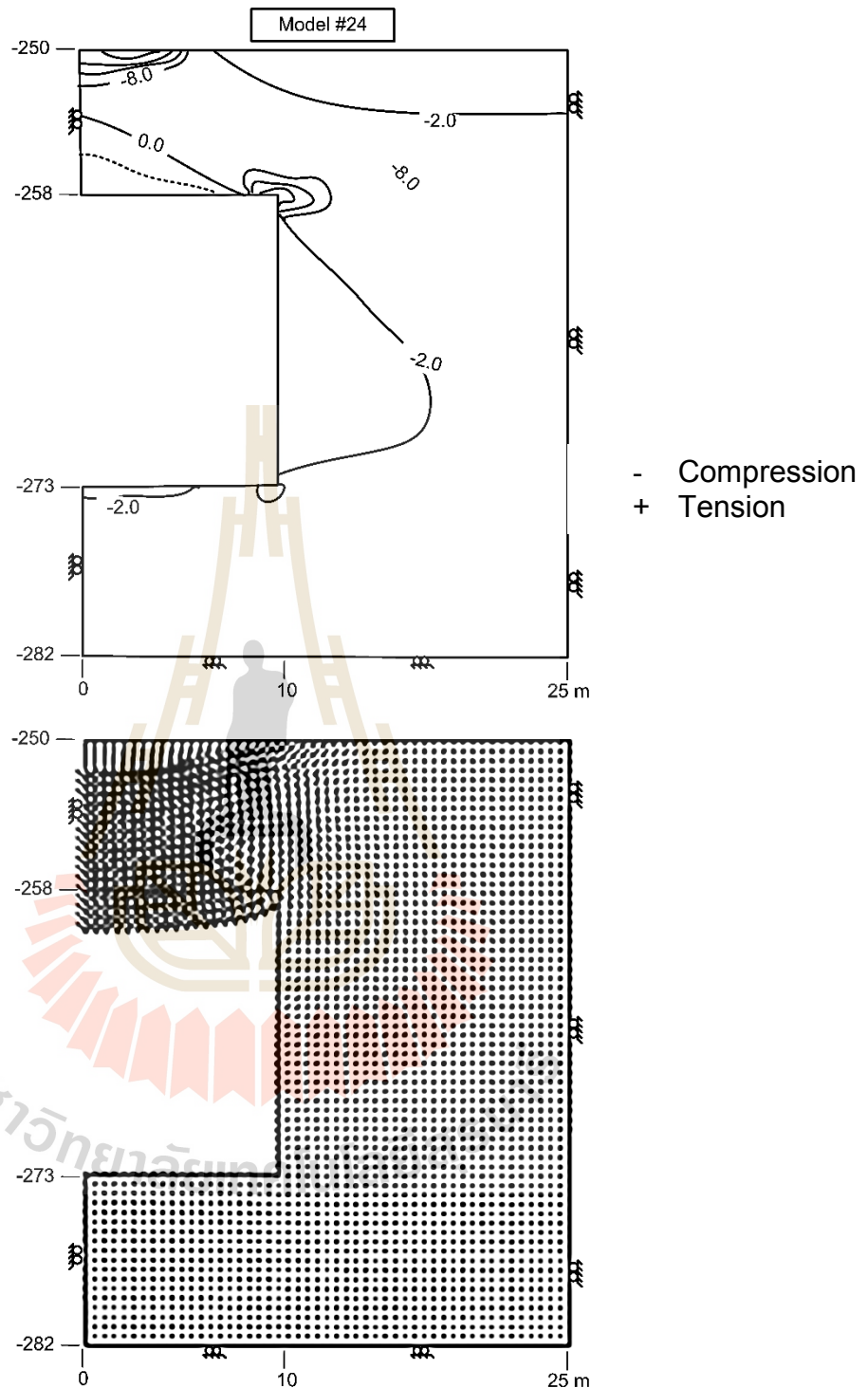


Figure A.24 Stress distribution (top) and displacement vectors (bottom) in mine roof for depths of 250 m and width of 20 m with minimum pressure at 50 % of in-situ stress

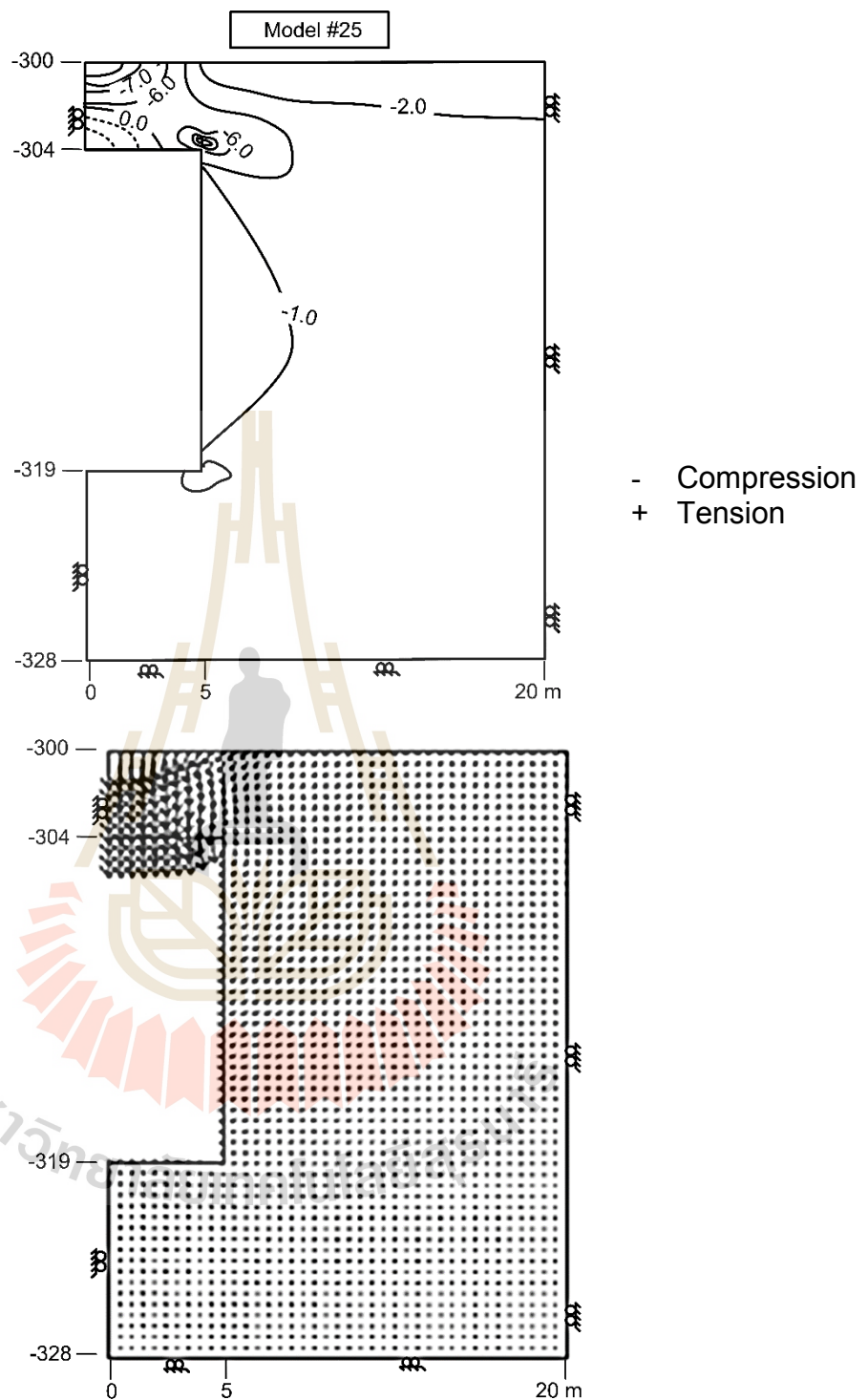


Figure A.25 Stress distribution (top) and displacement vectors (bottom) in mine roof for depths of 300 m and width of 10 m with minimum pressure at 20 % of in-situ stress

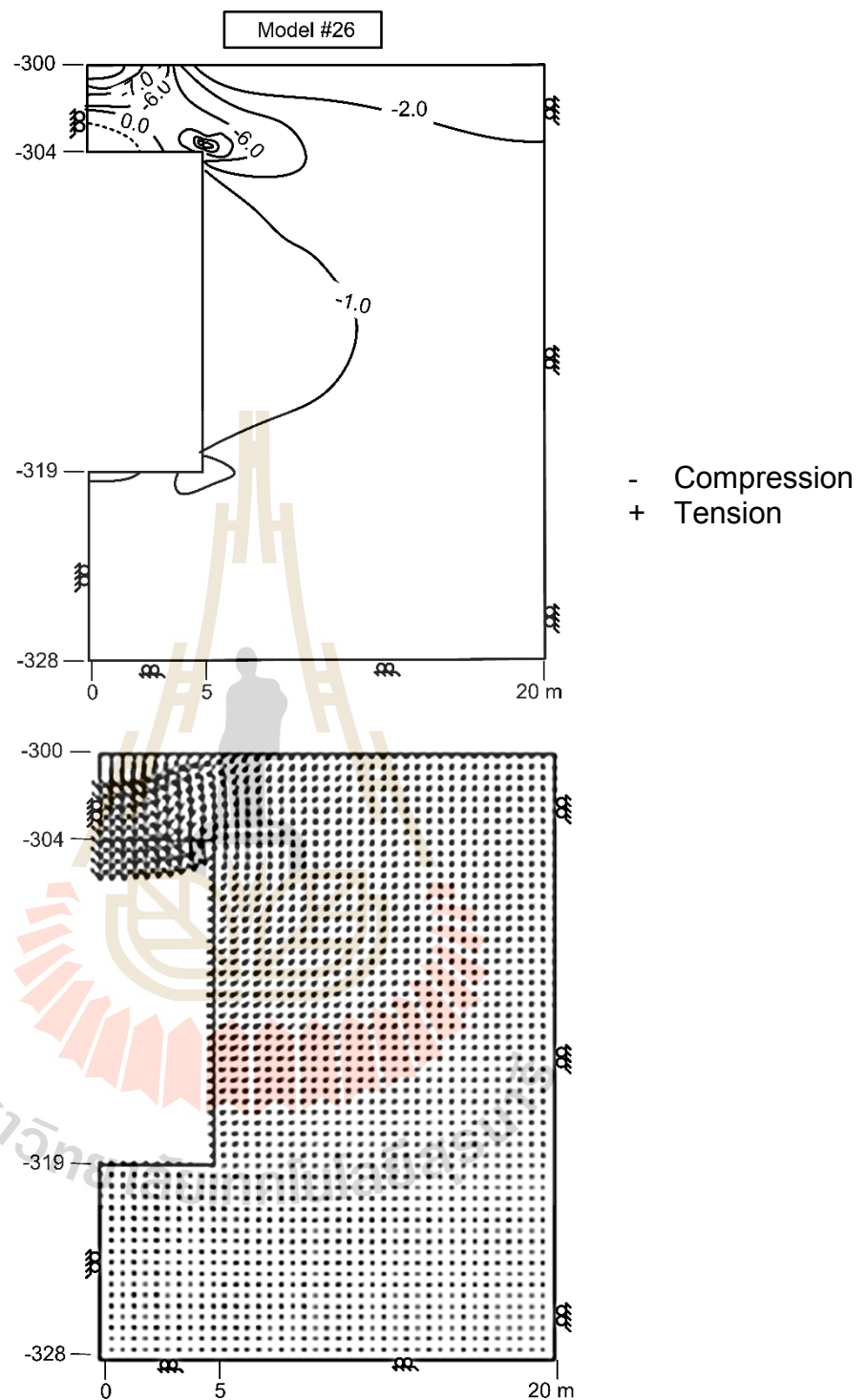


Figure A.26 Stress distribution (top) and displacement vectors (bottom) in mine roof for depths of 300 m and width of 10 m with minimum pressure at 30 % of in-situ stress

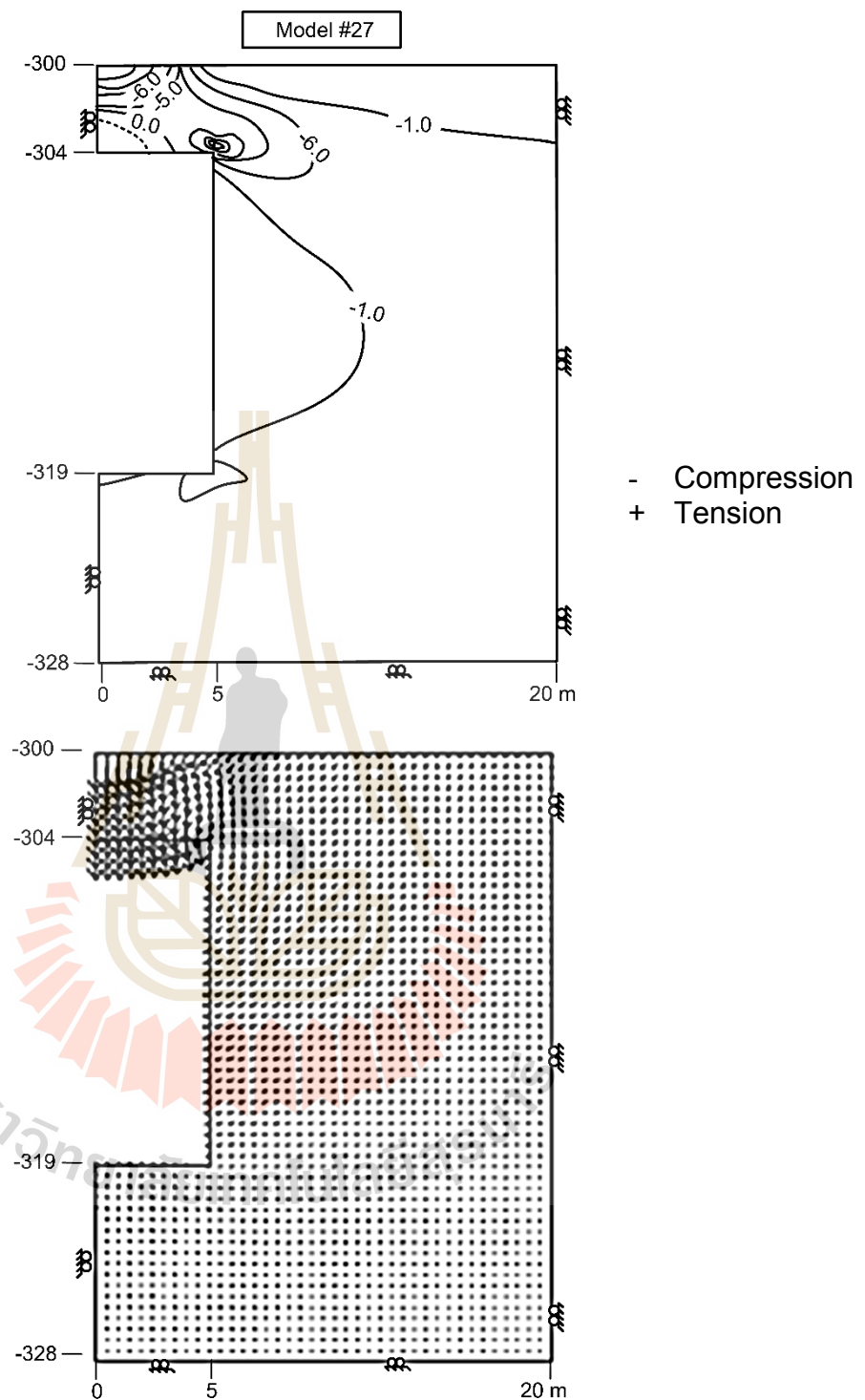


Figure A.27 Stress distribution (top) and displacement vectors (bottom) in mine roof for depths of 300 m and width of 10 m with minimum pressure at 40 % of in-situ stress

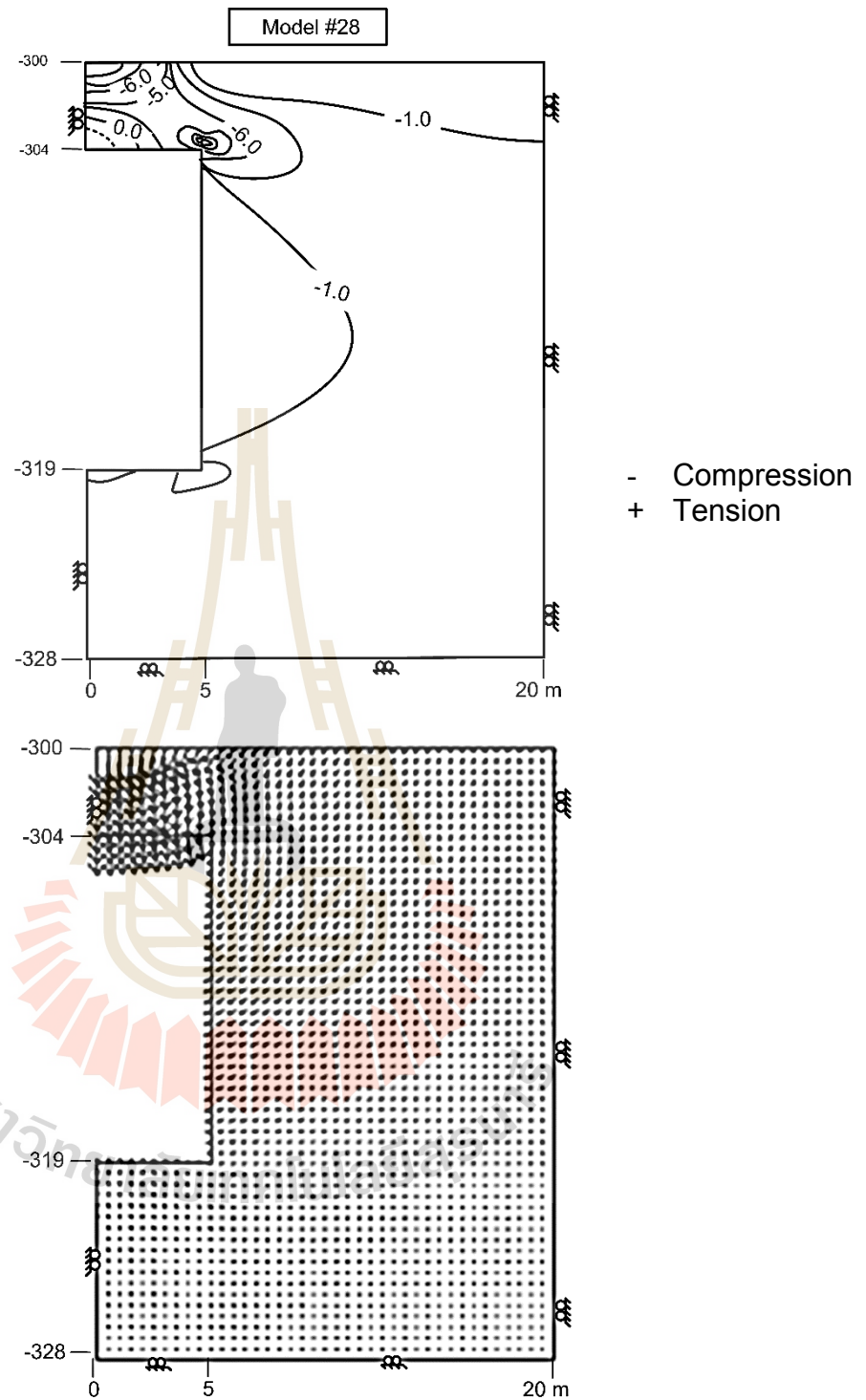


Figure A.28 Stress distribution (top) and displacement vectors (bottom) in mine roof for depths of 300 m and width of 10 m with minimum pressure at 50 % of in-situ stress

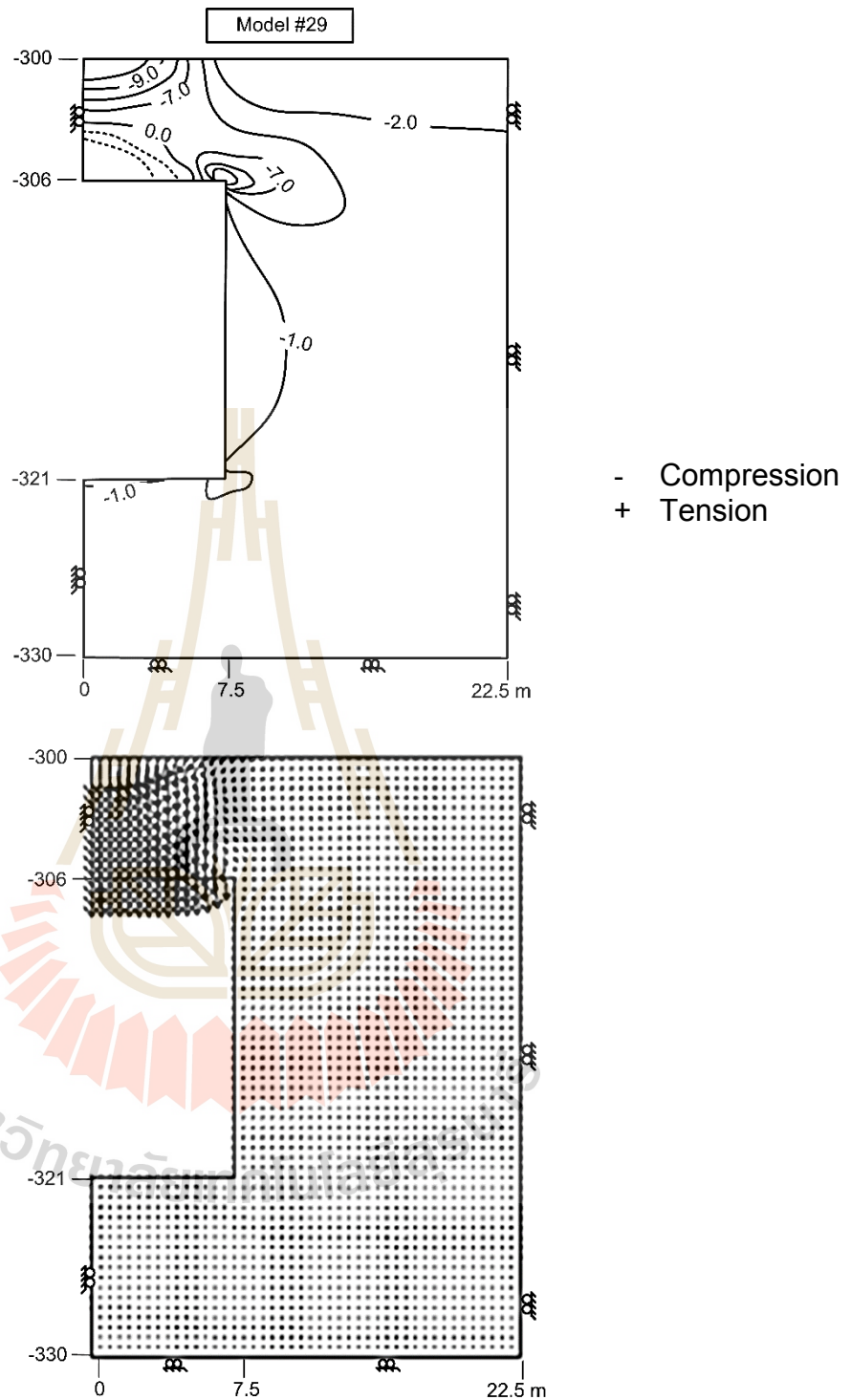


Figure A.29 Stress distribution (top) and displacement vectors (bottom) in mine roof for depths of 300 m and width of 15 m with minimum pressure at 20 % of in-situ stress

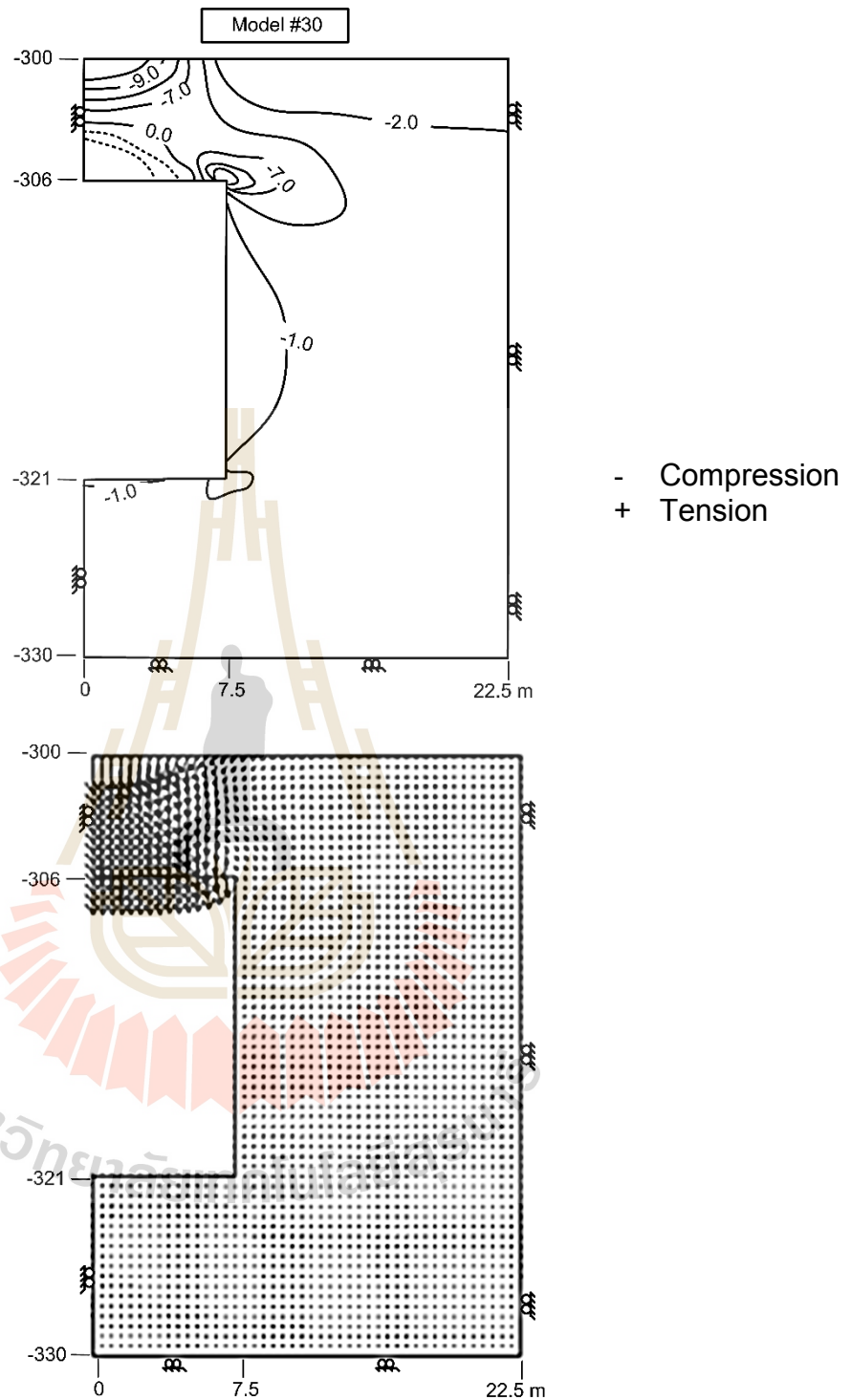


Figure A.30 Stress distribution (top) and displacement vectors (bottom) in mine roof for depths of 300 m and width of 15 m with minimum pressure at 30 % of in-situ stress

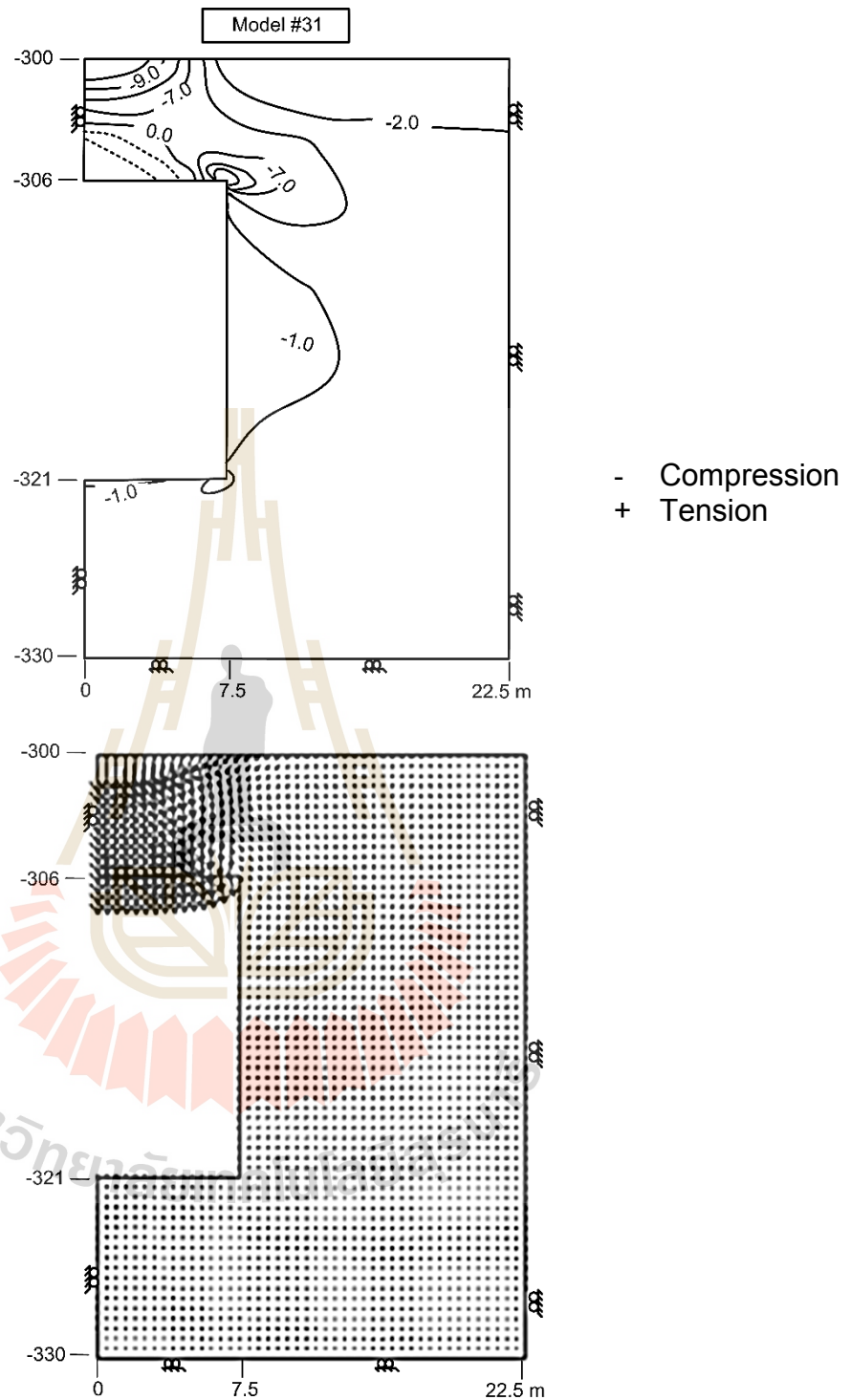


Figure A.31 Stress distribution (top) and displacement vectors (bottom) in mine roof for depths of 300 m and width of 15 m with minimum pressure at 40 % of in-situ stress

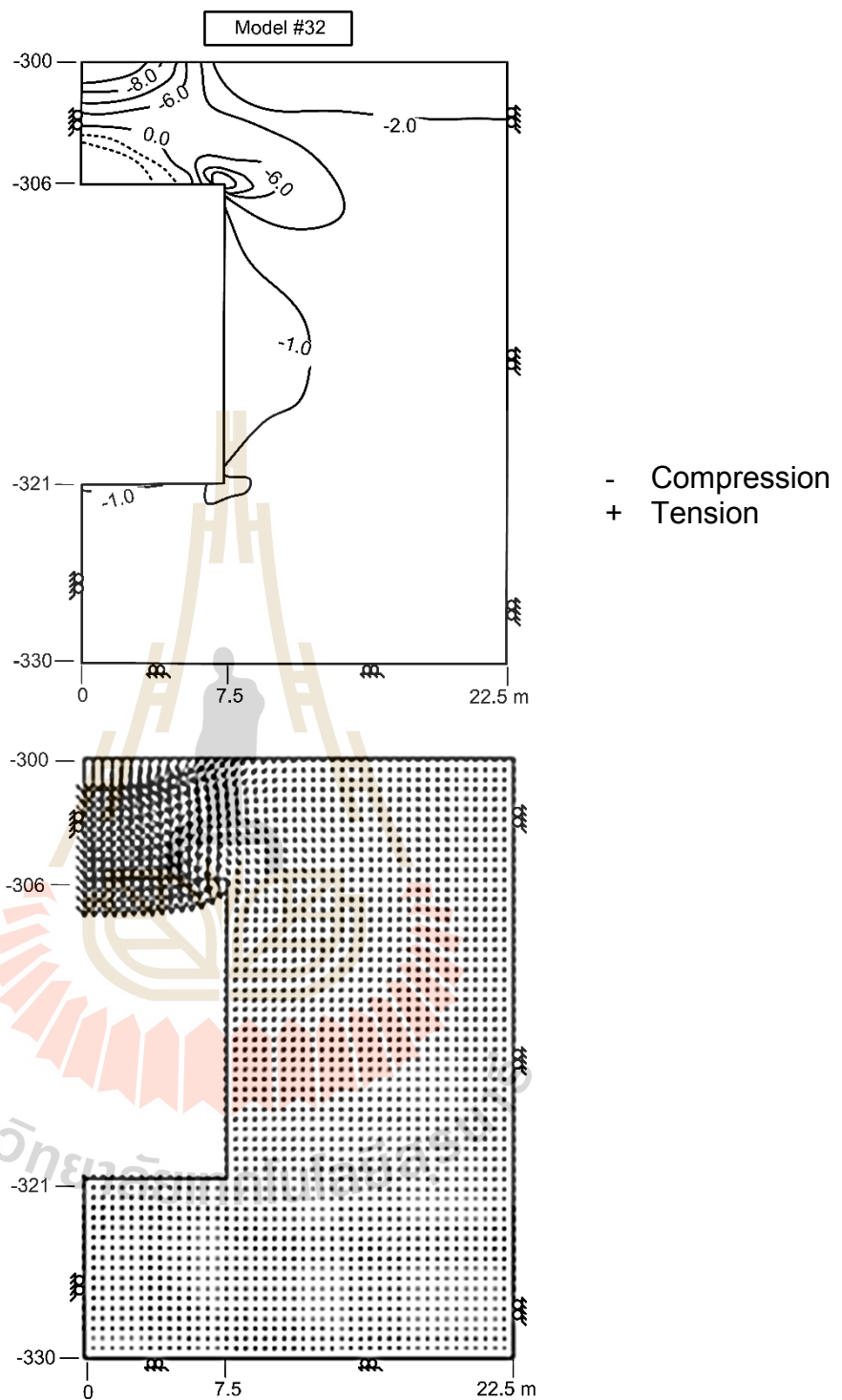


Figure A.32 Stress distribution (top) and displacement vectors (bottom) in mine roof for depths of 300 m and width of 15 m with minimum pressure at 50 % of in-situ stress

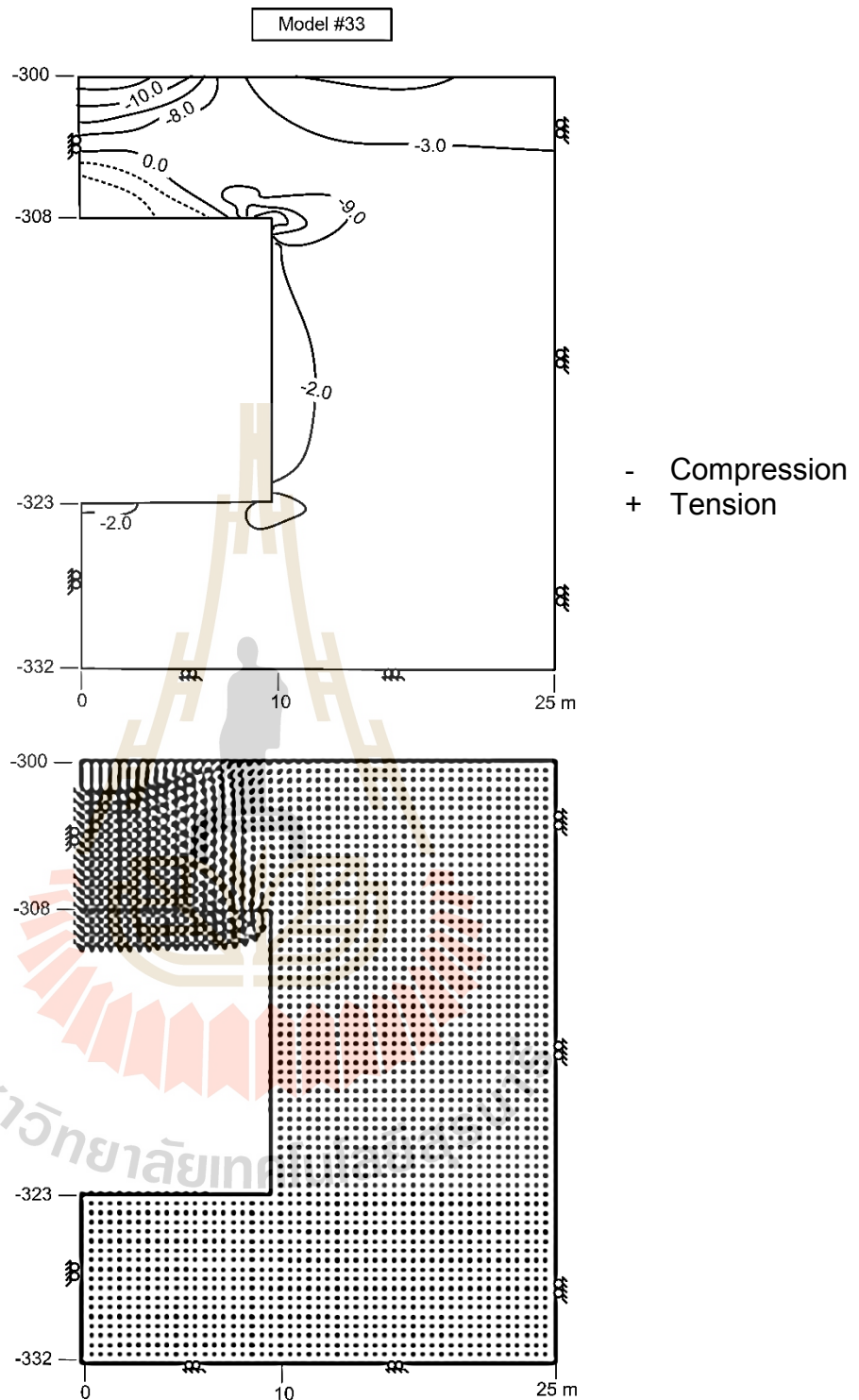


Figure A.33 Stress distribution (top) and displacement vectors (bottom) in mine roof for depths of 300 m and width of 20 m with minimum pressure at 20 % of in-situ stress

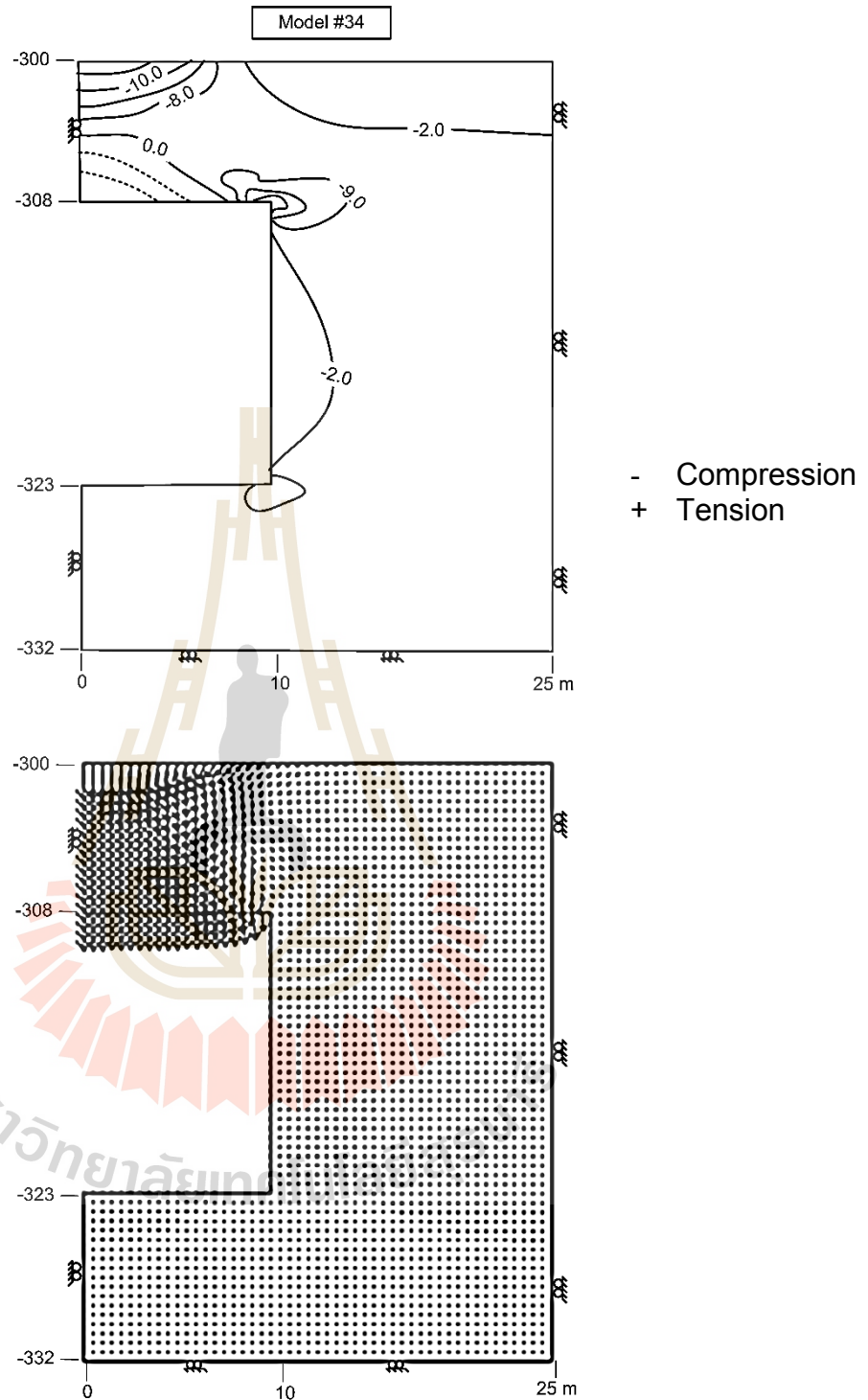


Figure A.34 Stress distribution (top) and displacement vectors (bottom) in mine roof for depths of 300 m and width of 20 m with minimum pressure at 30 % of in-situ stress

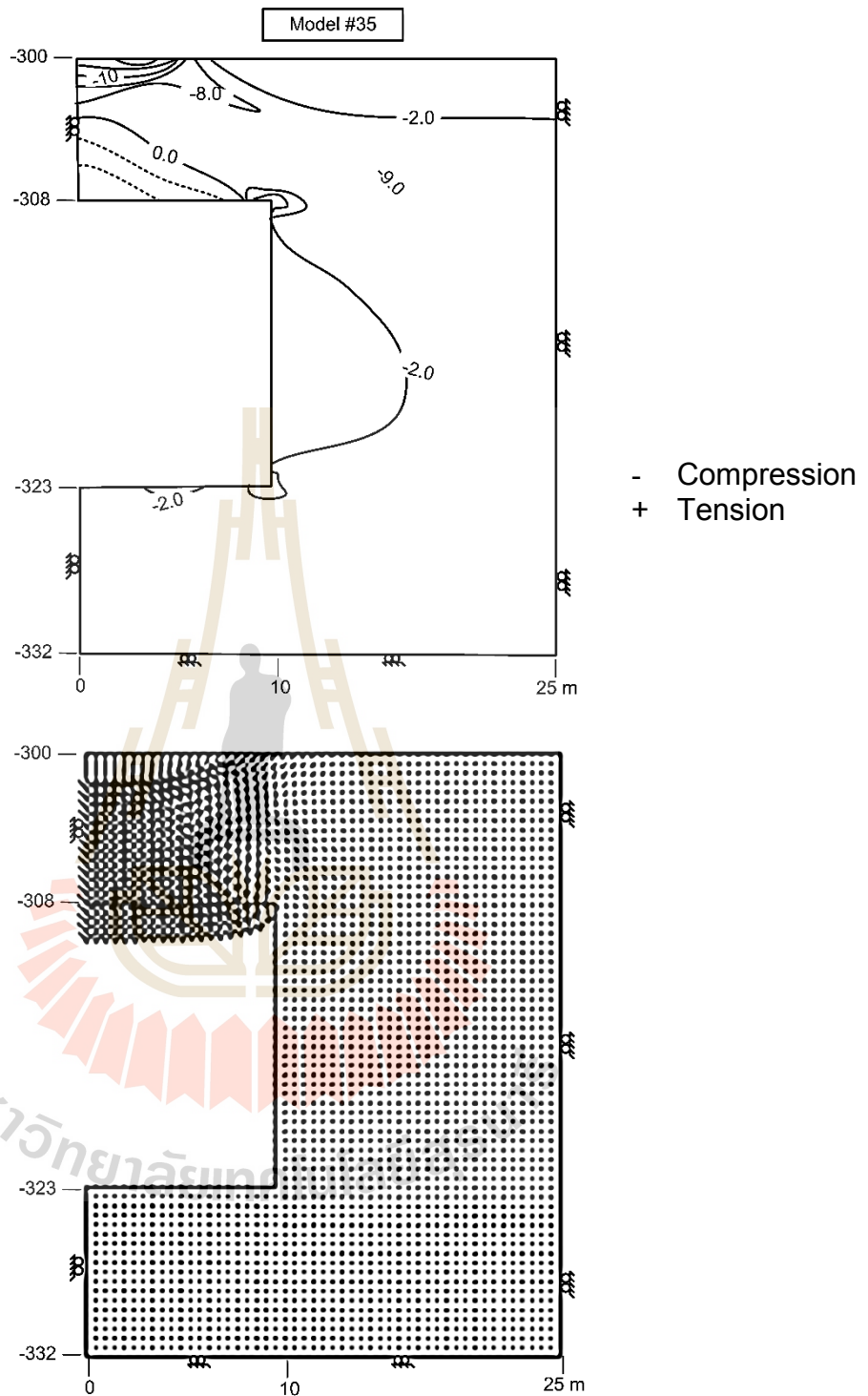


Figure A.35 Stress distribution (top) and displacement vectors (bottom) in mine roof for depths of 300 m and width of 20 m with minimum pressure at 40 % of in-situ stress

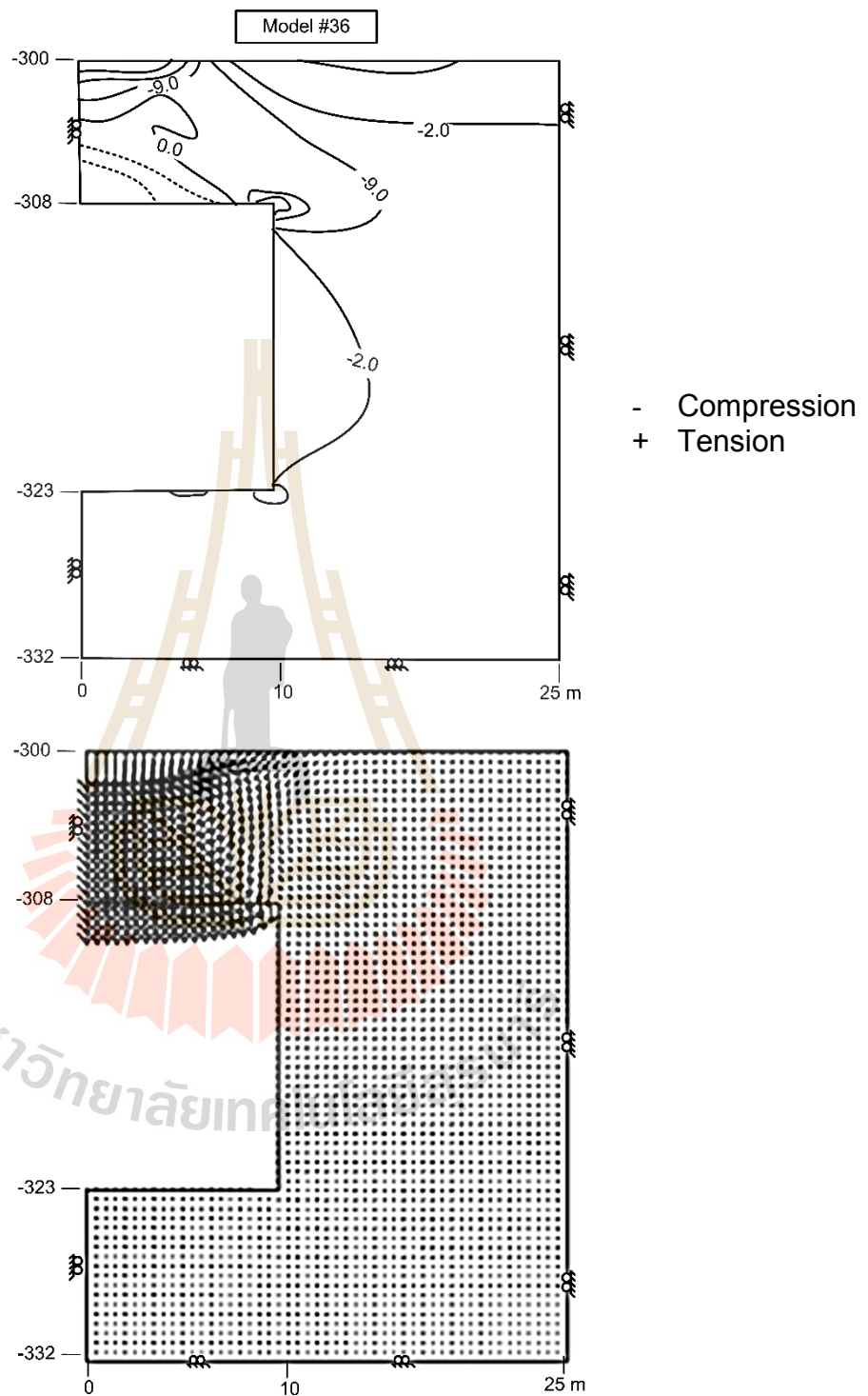


Figure A.36 Stress distribution (top) and displacement vectors (bottom) in mine roof for depths of 300 m and width of 20 m with minimum pressure at 50 % of in-situ stress

Table A.1 Applied load for creep test.

| Applied tensile stress (MPa) | Average Width (mm) | Average Height (mm) | Average Length (mm) | Load (N) |
|-------------------------------------|---------------------------|----------------------------|----------------------------|-----------------|
| 1.25 | 52.01 | 48.81 | 199.31 | 1.08 |
| 1.25 | 49.31 | 48.48 | 196.31 | 0.99 |
| 1.00 | 49.81 | 49.57 | 200.37 | 1.08 |
| 1.00 | 50.31 | 49.96 | 200.30 | 1.07 |
| 0.75 | 49.76 | 49.69 | 200.52 | 1.03 |
| 0.75 | 49.95 | 49.90 | 199.83 | 1.06 |
| 0.50 | 50.23 | 49.89 | 199.93 | 1.06 |
| 0.50 | 49.95 | 49.90 | 199.83 | 1.05 |

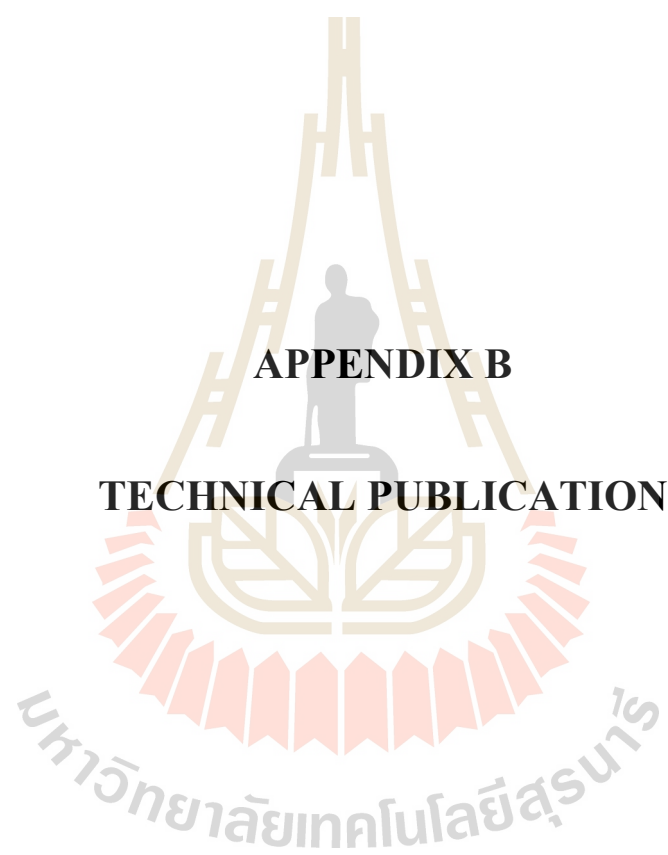
Table A.2 Applied load for cyclic loading test.

| Applied tensile stress (MPa) | Average Width (mm) | Average Height (mm) | Average Length (mm) | Load (kN) |
|-------------------------------------|---------------------------|----------------------------|----------------------------|------------------|
| 3.20 | 50.27 | 50.45 | 199.97 | 2.05 |
| 2.80 | 50.36 | 48.95 | 198.28 | 1.70 |
| 2.55 | 50.93 | 50.08 | 198.83 | 1.64 |
| 2.40 | 50.72 | 49.56 | 202.74 | 1.47 |
| 2.24 | 50.35 | 50.37 | 202.53 | 1.41 |
| 1.99 | 50.27 | 50.45 | 199.97 | 1.27 |
| 1.87 | 50.36 | 48.95 | 198.28 | 1.14 |
| 1.22 | 50.93 | 50.08 | 198.83 | 0.78 |
| 2.90 | 50.72 | 49.56 | 202.74 | 1.78 |
| 2.56 | 50.35 | 50.37 | 202.53 | 1.61 |
| 2.40 | 50.27 | 50.45 | 199.97 | 1.54 |
| 2.25 | 50.36 | 48.95 | 198.28 | 1.37 |
| 1.99 | 50.93 | 50.08 | 198.83 | 1.28 |
| 1.88 | 50.72 | 49.56 | 202.74 | 1.16 |
| 1.40 | 50.35 | 50.37 | 202.53 | 0.88 |

Table A.3 Applied load for loading rate test.

| Applied tensile stress (MPa) | Average Width (mm) | Average Height (mm) | Average Length (mm) | Load (kN) |
|------------------------------|--------------------|---------------------|---------------------|-----------|
| 3.19 | 52.01 | 48.81 | 199.31 | 1.98 |
| 2.72 | 49.31 | 48.48 | 196.31 | 1.61 |
| 2.21 | 49.81 | 49.57 | 200.37 | 1.35 |
| 1.53 | 50.31 | 49.96 | 200.3 | 0.96 |
| 1.70 | 49.76 | 49.69 | 200.52 | 1.04 |
| 1.23 | 49.95 | 49.9 | 199.83 | 0.77 |
| 0.78 | 50.23 | 49.89 | 199.93 | 0.49 |





APPENDIX B

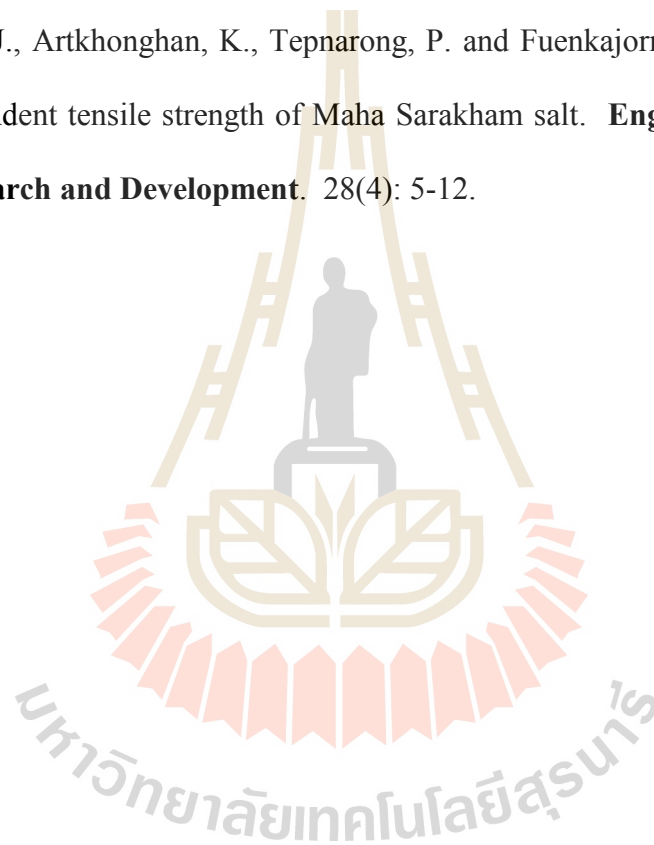
TECHNICAL PUBLICATION

มหาวิทยาลัยเทคโนโลยีสุรนารี

Technical Publication

Plangklang, J., Artkhonghan, K., Tepnarong, P. and Fuenkajorn, K. (2017). Time-dependent tensile strength and deformation of rock salt. In **11th South East ASEAN Technical University Consortium Symposium (SEATUC2017)**. March 13-14, Ho Chi Minh City, Vietnam.

Plangklang, J., Artkhonghan, K., Tepnarong, P. and Fuenkajorn, K. (2017). Time-dependent tensile strength of Maha Sarakham salt. **Engineering Journal of Research and Development**. 28(4): 5-12.



BIOGRAPHY

Miss Jenjira Plangklang was born on February 4, 1994 in Buriram, Thailand. She received her Bachelor's Degree in Engineering (Geotechnology) from Suranaree University of Technology in 2016. For her post-graduate, she continued to study with a Master's degree in the Geological Engineering Program, Institute of Engineering, Suranaree university of Technology. During graduation, 2016-2018, she was a part time worker in position of research assistant at the Geomechanics Research Unit, Institute of Engineering, Suranaree University of Technology.

